Re-visiting the Radio-Mechanical Feedback in Brightest Cluster Galaxies

by

Prathamesh Tamhane

A thesis
presented to the University of Waterloo
in fulfillment of the
thesis requirement for the degree of
Doctor of Philosophy
in
Physics

Waterloo, Ontario, Canada, 2023

Examining Committee Membership

The following served on the Examining Committee for this thesis. The decision of the Examining Committee is by majority vote.

External Examiner:	Sarah Gallagher Professor, Dept. of Physics and Astronomy, Western University
Supervisor(s):	Brian McNamara Professor, Dept. of Physics and Astronomy, University of Waterloo
Internal Member:	Michael Balogh Professor, Dept. of Physics and Astronomy, University of Waterloo
Internal Member:	Avery Broderick Professor, Dept. of Physics and Astronomy, University of Waterloo
Internal-External Member:	Pierre-Nicholas Roy Professor, Dept. of Chemistry, University of Waterloo

Author's Declaration

This thesis consists of material all of which I authored or co-authored: see Statement of Contributions included in the thesis. This is a true copy of the thesis, including any required final revisions, as accepted by my examiners.

I understand that my thesis may be made electronically available to the public.

Statement of Contributions

Chapters 2, 3, and 4 of this thesis contain original research written by myself, Prathamesh Tamhane under the supervision of Dr. Brian McNamara. Chapter 2 has been published in the peer-reviewed journal Monthly Notices of the Royal Astronomical Society (MNRAS). The paper reference is:

Tamhane P. D.: McNamara B. R.; Russell H. R.; Edge A. C.; Fabian A. C.; Nulsen P. E. J.; Babyk I. V., 2022, Monthly Notices of the Royal Astronomical Society, 516, 861, doi:10.1093/mnras/stac2168.

A revised version of chapter 3 has been accepted for publication in Monthly Notices of the Royal Astronomical Society. The paper reference is:

Tamhane, Prathamesh D.; McNamara, Brian R.; Russell, Helen R.; Combes, Francoise; Qiu, Yu; Edge, Alastair C.; Maiolino, Roberto; Fabian, Andrew C.; Nulsen, Paul E. J.; Johnstone, R.; Carniani, Stefano, (2022). The manuscript has been for publication in Monthly Notices of the Royal Astronomical Society. DOI:10.1093/mnras/stac3803

In each of these publications, I, P. D. Tamhane, am the first author, having analyzed the data and written the manuscripts. The second author, Dr. B. R. McNamara, is my supervisor and significantly edited sections 2.7 and 2.10 in chapter 2. Dr. H. R. Russell led the proposal to obtain the XSHOOTER data presented in chapter 3. The remaining authors are collaborators that provided comments on how to improve manuscripts before submission for publication.

Abstract

The self-regulated feedback from the Active Galactic Nucleus (AGN) plays a key role in the formation and evolution of galaxies by heating and expelling gas in galaxies. The goal of this thesis is to investigate the role of radio-mechanical AGN feedback in expelling gas in central cluster galaxies (BCGs), triggering star formation in the outflowing gas and promoting runaway cooling of the hot intracluster medium gas.

We used ALMA observations to characterize molecular gas flows in 14 BCGs and compared them with molecular flows observed in nearby AGN hosting and starburst galaxies. The molecular flows in BCGs are slower, 10–1000 times larger, 10–100 times heavier and carry more momentum compared to outflows driven by quasar mode AGN feedback and starbursts. The kinetic power of flows lies substantially below driving power. The lifting factor, a product of flow mass and radius divided by the driving power, is substantially larger in BCGs showing that radio feedback, when active, is more effective at lifting gas. BCGs form fewer stars per unit molecular gas mass, suggesting that star formation is suppressed, perhaps because the gas in these systems rarely forms molecular disks. The radio mode feedback can drive massive gas outflows and suppress star formation in negative feedback.

Paradoxically, radio jets can not only inhibit star formation but also trigger star formation. In chapter 3, we studied one such example of radio-jet triggered star formation in the BCG of the Abell 1795 cluster using VLT optical spectroscopy, *HST* and ALMA data. Abell 1795 has bright UV filaments surrounding radio jets indicating recent radio jet-triggered star formation. The total extinction corrected star formation rate in the BCG is 9–21 $M_\odot$ yr^{-1}. We showed that the star formation follows the Kennicutt-Schmidt law with a low efficiency. The gas depletion time of 1 Gyr due to star formation is longer than the dynamical time of the outflow, indicating that star formation may be eventually quenched. The velocity structure function of the warm ionized gas suggests that radio jets may be able to drive supersonic turbulence. Thus radio-mechanical feedback can both trigger and inhibit star formation in the same galaxy on different timescales.

Heating from radio-mode feedback does not completely offset cooling of hot gas at all times, as many BCGs have large amounts of cold gas. We also studied the formation of cold gas by cooling of uplifted low entropy gas from centres of galaxy clusters by cavities in 24 galaxy clusters and their BCGs. We showed that single generation of cavities cannot lift enough low entropy gas to form observed amount of cold gas in BCGs. The amount of uplifted gas expected to have cooled from cavities within their lifetimes is less than the observed cold gas mass in many BCGs suggesting that either efficient gas cooling is

required or that the uplift mechanism alone cannot produce all the cold gas in BCGs. The average altitude to which the gas needs to be lifted by cavities to cool before it falls back is also large ($\sim$80 kpc) compared to the observed extent of nebular emission even in the most extended systems. Therefore, we found that stimulated feedback by uplift alone is generally insufficient to explain the observed levels of molecular gas mass in BCGs.

Acknowledgements

I thank my supervisor Prof. Brian McNamara for giving me an opportunity, his guidance and continuous support. I would like to thank the committee members Michael Balogh, Avery Broderick and P. N. Roy for taking the time to listen to my presentations and for their useful guidance. I would like to thank my collaborators Helen Russell, Alastair Edge, Andrew Fabian, Paul Nulsen, Francoise Combes, Yu Qiu, Roberto Maiolino for their guidance and useful feedback on my papers. I thank Adrian Vantyghem for getting me started with ALMA data analysis at the beginning of my PhD and helping me with Python time and time again.

I couldn't have made this journey without all the amazing friends I have made from all over the world. Thank you Adrian, Connor and Andrew for our long (sometimes hours long) discussions on random topics. I would like to thank Kristi for organizing various social events, camping trips that brought everyone together and made everyone feel welcome and especially for introducing me to rock climbing. Thank you Iurii, Muzi and MJ for useful discussions. I would like to thank all the other graduate students for their discussions, camaraderie and amazing company during Astrobeer and other events.

I would like to thank my awesome roommates Sainath, Cristobal and Varsha for their company during the pandemic lockdown. Thank you Cristobal for introducing me to his friends. Thanks to Julie, Ekin and everyone else who welcomed me and almost made me feel like a part of Civil engineering department. Also thank you for organizing all the hikes, bike trips, the Mexico trip, potlucks and other social events and always including me. I would like to thank Dino, Tomas, Karolina and little Viola for their warm company during the pandemic, accompanying me to the climbing gym and outdoor climbing. Thank you Yuba for your company at coffee shops while working during the pandemic. Thank you Huether hotel and their staff for allowing me to sit for hours working when the University was closed. I would also like to thank my friends from undergrad Sainath, Mihir, Sreevani, Nishad, Shiva and everyone else for their support.

Most importantly, I would like to thank my parents for their continued, unwavering love and support at every step of the way.

Dedication

I dedicate this thesis to my parents.

Table of Contents

List of Figures

List of Tables

Chapter 1

Introduction

The formation and evolution of the Universe currently are best explained by the ΛCDM model, where Λ is the cosmological constant associated with the as yet unknown *dark energy*, and CDM stands for Cold Dark Matter. The ΛCDM model is highly successful in explaining the properties of the Universe. Strong constraints on the parameters of this model have been placed. The constraints particularly come from the observations of the Cosmic Microwave Background (CMB). The CMB is the leftover radiation from the very early Universe when it was opaque because the density of the Universe was very high. When the density dropped due to the expansion of the Universe, the photons could escape without interacting with matter, an epoch also called the time of *recombination*. The CMB is as close as we can get to the image of the Universe since its formation 13.7 billion ago. As the Universe expanded, the radiation cooled. It is now observed in microwave frequencies and has a temperature of 2.75 K. Various observational programs have mapped the CMB radiation, such as NASA's WMAP and ESO's Planck Observatories. The most recent constraints come from the Planck observatory and the CMB spectrum is very well explained by the ΛCDM model (Planck Collaboration et al., 2020).

In the ΛCDM framework, the universe evolved in a bottom-up hierarchical scenario. Initially, the Universe was hot and smooth with weak, homogeneous gaussian distributed density fluctuations. During the inflation, the perturbations were amplified making the Universe clumpy and in-homogeneous, as it is observed today. About 85% of matter in the Universe is made up of as yet unknown particles called dark matter and only 15% is made up of observable baryons (Planck Collaboration et al., 2020). The initial perturbations collapsed and merged under the influence of gravity to form dark matter halos. The dark matter halos serve as the sites of galaxy formation, where the gas condenses in their central deep potentials, fueling star formation. As dark matter halos merge and grow, they

accrete more gas and fuel more star formation. Eventually, galaxies come together under the influence of gravity to form galaxy clusters. Galaxy clusters are the most massive and largest gravitationally bound objects in the Universe. The biggest clusters of galaxies have total masses $\sim 10^{15}$ $M_\odot$, where $M_\odot$ is the mass of the Sun. The stellar mass in clusters makes up only a few percent of the total mass. About 90% of the baryonic mass in clusters is in the hot, diffuse gas that permeates the cluster known as the intracluster medium (ICM). Galaxies residing at the centres of clusters are called Brightest Cluster Galaxies (BCGs).

Despite the success of the ΛCDM model, there are problems that are not consistent with observations. Some of these problems are summarized below.

1.1 Galaxy Luminosity Function

As explained earlier, in the standard ΛCDM structure formation scenario, the gas condenses in the central deep potentials of dark matter halos, fueling star formation and forming galaxies. As dark matter halos merge and grow, they accrete more gas and fuel more star formation. As galaxies grow they become more massive and brighter. This hierarchical model of structure formation is usually modelled using large-scale cosmological numerical simulations. In these simulations, gravity can be well described by Newtonian theory. Dark matter is thought of as collisionless particles that only interact gravitationally, and is represented by a set of point particles, called N-bodies. Small density fluctuations are applied to the initial homogeneous distribution of particles. Their evolution is tracked from very early stages to the current epoch. To compare these models to observations, the number density of galaxies is counted assuming each dark matter halo hosts a galaxy of proportional mass.

This simple prescription predicts a higher number of galaxies at both low and high luminosities than what is observed (Baugh, 2006). This is characterized by the galaxy luminosity function. The observed luminosity function is given by the Schechter function (Schechter, 1976) as:

$$\frac{dn}{dL} = \left(\frac{\phi^*}{L^*}\right) \left(\frac{L}{L^*}\right)^{\alpha} e^{-(L/L^*)}, \tag{1.1}$$

where dn/dL is the number of galaxies per unit comoving volume per unit luminosity and L^* is the characteristic luminosity at which the power law part of the Schechter function cuts off. The typical observed value of L^* in the nearby Universe corresponds to a galaxy

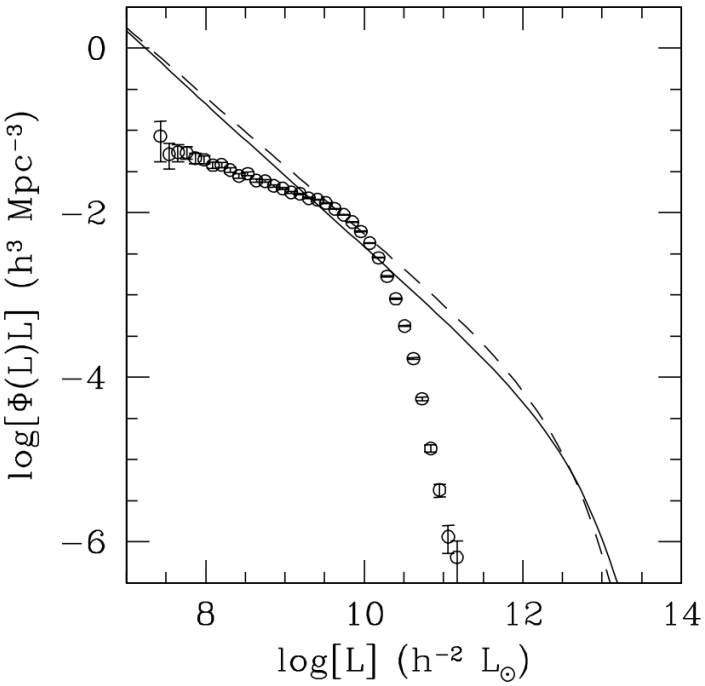

Figure 1.1: The observed b band galaxy luminosity function in the 2dFGRS survey is represented by circles compared with the Seth & Tormen (Press-Schechter) halo mass function as a solid (dashed) line assuming M/L = 100 hM/L$_\odot$. Note the discrepancy at the low and high-mass end for the dark matter-only case, suggesting that the M/L ratio is not constant. (Figure is taken from Yang et al. (2003) with permission).

mass of 10^{12} $M_\odot$. Figure 1.1 from Yang et al. (2003) shows the galaxy luminosity function for galaxies in the 2dFGRS survey (Norberg et al., 2002), compared with the halo mass function assuming a constant mass-to-light ratio. The figure clearly shows the observed deficit of low and high-mass galaxies in the Universe under simplistic assumptions. Thus, additional physics is required to explain the observed demographics of galaxies.

1.2 The M-σ relation

Every massive galaxy is believed to host a supermassive black hole (SMBH) at its centre (Kormendy & Richstone, 1995). The properties of SMBHs have been considered to be closely associated with the properties of their host galaxies. Thus, correlations between various host galaxy parameters and SMBH parameters were discovered. The correlations showed that the evolution of galaxies and their SMBH are fundamentally interlinked. Out of all the correlations, the M-σ relation is particularly strong. It is given by equation 1.2 and is also shown in Figure 1.2 (Gültekin et al., 2009).

$$\log(M_{BH}/M_\odot) = (8.12 \pm 0.08) + (4.21 \pm 0.41)\log\left(\frac{\sigma}{200\,\mathrm{km\,s^{-1}}}\right), \tag{1.2}$$

where M_{BH} is the mass of the black hole in solar masses and σ is the stellar velocity dispersion in the bulge. The velocity dispersion of stars is directly related to the galaxy's mass. Indeed previous studies have shown a correlation between the galaxy bulge mass and black hole mass (Kormendy & Richstone, 1995). Other correlations include the correlations between the black hole mass and bulge luminosity (Kormendy & Richstone, 1995; Magorrian et al., 1998) and galaxy light concentration (Graham et al., 2001). However, these correlations are not as tight as the M-σ relation. Nevertheless, they suggest the co-evolution of black holes and their host galaxies. Why these correlations are observed is a debated issue. Some studies argued that it is a result of hierarchical merging (Peng, 2007; Jahnke & Macciò, 2011; Graham & Scott, 2013) but the energy budget analysis requires a feedback mechanism that couples the growth of black holes to the growth of their host galaxies.

1.3 Cooling flow problem

Another major problem is that the galaxy evolution models without any kind of feedback mechanism predicted large amounts of cold gas and star formation in massive galaxies

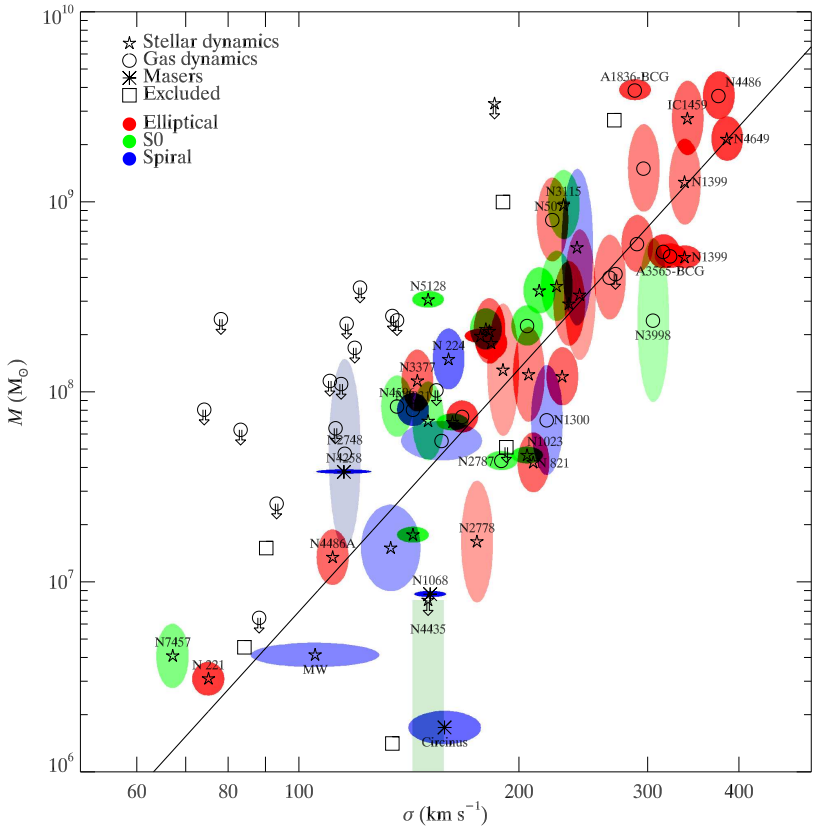

Figure 1.2: The figure shows the relationship between the black hole mass and the stellar velocity dispersion in the bulges of galaxies (M-σ relation) and its scatter. The black line is the best-fit line given by equation 1.2. The figure is reproduced with permission from (Gültekin et al., 2009).

and "cool-core" galaxy clusters. Cool-core galaxy clusters are characterized by short ($\leq$1 Gyr) gas cooling times and low entropy, dense ($\sim 10^{-2}$ cm^{-3}) gas in the core (Hudson et al., 2010). The gas in the ICM gets heated to high temperatures of a few 10^7 K in the deep gravitational potentials of clusters and primarily emits in X-rays. The gas is in global hydrostatic equilibrium, which means that the gravitational force acting on the gas is balanced by its thermal pressure. The primary emission mechanism in the ICM gas is the bremsstrahlung emission, in which the emissivity of the gas is proportional to the square of the density of the gas (Sarazin, 1988). Due to their dense cores, cool-core clusters have a strong peak in X-ray surface brightness in the core. In the absence of heating, the hot gas will radiate away its energy in a cooling time given by

$$t_{\rm cool} = E_{\rm th}/L_X = \frac{p}{(\gamma-1)n_e n_H \Lambda(T,Z)}, \tag{1.3}$$

where, $E_{\rm th}$ is the total thermal energy of the gas, L_X is its X-ray luminosity which is approximated as $n_e n_H \Lambda(T,Z)$, p is the gas pressure, n_e and n_H are the electron and proton densities, $\Lambda(T,Z)$ is the cooling function that depends on the temperature T and metallicity Z of the gas and $\gamma \sim 5/3$ is the ratio of specific heats for monoatomic ideal gas. The cooling time at centres of clusters falls below 1 Gyr, which is much shorter than the age of the Universe, indicating that an enormous amount of gas should cool to low temperatures.

As the gas radiates its energy, its entropy ($\propto T/\rho^{2/3}$) decreases, which must correspond to an increase in its density (ρ). Denser gas sinks deeper into the gravitational potential of the cluster settling at a lower radius than its initial radius, reducing the thermal pressure at its initial radius. Since the gravitational pressure at the initial radius is unchanged since it only depends on the amount of gas above that radius, it overpowers the thermal pressure and drives an inflow of gas. This is a classical schematic of a cooling flow (Fabian & Nulsen, 1977; Cowie & Binney, 1977; Fabian, 1994). Thus, increased density causes even more gas to cool rapidly, increasing the X-ray emissivity in the centre. The observed X-ray luminosities of galaxy clusters predict classical gas cooling rates of hundreds to thousands of solar masses per year.

Early X-ray observations detected weak line emission from the Fe L complex, consistent with the predictions of the classical cooling flow model (Canizares et al., 1982, 1988). Later, far more sensitive observations using the $XMM-Newton$ Reflection Grating Spectrometer failed to confirm this result (Kaastra et al., 2001; Peterson et al., 2001; Tamura et al., 2001a,b). Robust spectroscopy of the most extreme systems measured gas cooling rates of $\sim$100 M$_\odot$ yr^{-1}, which is a factor of ten lower than expected from classical cooling flows (Morris & Fabian, 2003). Other indirect evidence of cooling in the form of warm, ionized

gas (Heckman, 1981), star formation (Johnstone et al., 1987; McNamara & O'Connell, 1989) and cold molecular gas ($T \ll 100$K) (Edge, 2001; Salomé & Combes, 2003) has been detected in the BCGs of cool-core clusters. However, the star formation rates in BCGs are typically a few $M_\odot$ yr^{-1}, only reaching a few hundred $M_\odot$ yr^{-1} in the most extreme systems (McDonald et al., 2018). For expected gas cooling of hundred to thousand $M_\odot$ yr^{-1}, these estimates are ten to hundred times smaller. Up to 10^{10} $M_\odot$ of molecular gas has been detected in galaxy clusters (Edge, 2001; Salomé & Combes, 2003). However, unimpeded cooling for 1 Gyr should produce upwards of 10^{11} $M_\odot$ of molecular gas. The observed cold gas masses account for only 5 – 10 per cent of expected molecular gas in BCGs.

1.4 Feedback mechanisms

The formation and evolution of stars and gas (baryons) in galaxies is more complex than the formation of dark matter halos. Simple prescriptions for the formation and evolution of galaxies do not match observations as explained above. Galaxy evolution models incorporating radiative cooling and gravitational heating alone produce too many stars, too much cold gas and few hot baryons (Balogh et al., 2001; Davé et al., 2001; Bregman, 2007). Additionally, the models have structural problems where the dark matter is found to be excessive in dwarf and barred galaxies (Moore, 1994; Navarro et al., 1997) or the galaxies are not extended enough or their bulges are too massive because stars are forming too efficiently early in the formation process of galaxies (Brook et al., 2011). Thus, additional physics is required to explain the observations.

Some of the initial works invoked gas cooling, and feedback from supernovae as some of the mechanisms to reproduce the observed galaxy luminosity functions (White & Frenk, 1991; Cole et al., 1994). Later, feedback from AGN in the form of powerful winds and radio jets was also invoked to stop the growth of black holes and spheroids, heat the atmospheres of galaxies and quench star formation (Silk & Rees, 1998; Fabian, 1999; King, 2003). Now AGN and starburst feedback is an integral part of all galaxy evolution simulations. Simulations have shown that the combination of these feedback mechanisms can regulate the growth of massive galaxies by heating or expelling gas from halos (Bower et al., 2006, 2008; Croton et al., 2006). Significant improvement was achieved when the addition of the radio mode feedback (see section 1.4.4) from the AGN was able to reproduce the observed luminosity function of massive galaxies (Bower et al., 2006; Croton et al., 2006; Davé et al., 2012). Signatures of both starburst and AGN feedback are observed in many galaxies in the local and distant Universe. In the following sections, we review these feedback processes.

1.4.1 Starburst feedback

Starburst feedback is most prominent in intensely starforming systems. Massive stars with masses between ~ 8 and 25 $M_\odot$ end their lives after ~ 3 Myr as they undergo core collapse causing a violent explosion of the star's outer layers called a supernova (SN). As a result, stars eject $\sim$ 1–10 $M_\odot$ of metal[1] enriched material with kinetic energy $\sim 10^{51}$ erg. This ejected energy can significantly affect the ISM and regulate star formation. This is called the SN or starburst feedback. Supernova feedback can regulate star formation (see Mac Low & Klessen, 2004; McKee & Ostriker, 2007, and references therein), drive turbulence in the ISM (Kim et al., 2001; Joung & Mac Low, 2006; Agertz et al., 2009; Tamburro et al., 2009) and generate galactic outflows (Martin, 1999; Oppenheimer & Davé, 2006). Dekel & Silk (1986) first proposed that galactic outflows generated by stellar feedback can blow away the gas in star-forming regions limiting the number of baryons from which the stars form, subsequently suppressing star formation. How the energy released by SN couples to the ISM depends on the state of the pre-SN ISM. In low-density environments, the ejecta continues to be in a free expansion phase keeping the kinetic energy and momentum. In more typical environments, some part of the energy is quickly transformed into thermal energy through shock heating the ejecta and the surrounding ISM to high temperatures. Once the mass of the swept-up material becomes equal to the ejected material, the outer shock radius expands, the temperature drops and the SN remnant enters a pressure-driven phase, where the pressure on the inside is still larger than the pressure outside the expanding material. Once the pressure inside becomes equal to the pressure outside, the SN enters a momentum-conserving snowplough and continues to sweep up the ISM. Some studies have shown that clustered supernovae going off in star-forming regions within typical starburst timescales of $\sim 10^8$ yr can provide a momentum boost up to an order of magnitude greater than isolated SN, which is sufficient to drive galaxy scale outflows of gas and dust (see Fig. 1.3 for example) (Sharma et al., 2014; Gentry et al., 2017; El-Badry et al., 2019).

Additionally, stellar winds from young, massive stars profoundly transform the surrounding ISM and clear the denser gas from young stellar clusters before the SN occur (Longmore et al., 2014). The bubble created by these winds can enhance the SN feedback efficiency. It can also affect the dust being formed in the ejecta or pre-existing dust in these environments (El-Badry et al., 2019; Martínez-González et al., 2019). Cosmic rays (CRs) originating in the SN remnants can ionize and heat the ISM including the cold material that is optically thick. The CR energy is not radiated away during the expansion of the SN remnant. Although their energy is small, they can inject momentum at a significant rate. Therefore, they can continue the expansion of the SN remnant and can also drive

[1]In astronomy, all elements heavier than Hydrogen and Helium are called metals.

winds (Salem et al., 2016; Diesing & Caprioli, 2018).

Multiphase galactic outflows driven by starburst have been observed in many starforming galaxies (see Rupke, 2018, for review and references therein). Over the last two decades, a large number of studies have tried to model the starburst feedback and incorporate it into simulations of galaxy evolution (Dubois & Teyssier, 2008; Scannapieco et al., 2008; Agertz et al., 2009; Joung et al., 2009; Ceverino & Klypin, 2009; Governato et al., 2010; Kimm et al., 2015). However, modelling the SN feedback has proven to be challenging and its results are generally mixed. The differences and contradictions between these studies find their origins in the details of how SN feedback is modelled, different numerical recipes, different resolutions adopted in these models as well as a variety of galaxy masses and merger histories (see Scannapieco et al., 2012, and references therein). Therefore it is still unclear to what extent SN feedback affects low and high-mass galaxies. For example, SN feedback only has a small impact on the formation of massive galaxies, mostly because the deep potential wells of massive galaxies prevent the gas from escaping the galaxy. Moreover, SN feedback fails to stop the flow of cold gas toward the centre of galaxies (Powell et al., 2011). The gas pushed away by SN only modestly interacts with the inflowing gas thus allowing massive galaxies to form too many stars. This is corroborated by hydrodynamical simulations that incorporate a subgrid recipe for SN feedback without including the black hole feedback. Comparison of these simulations with an expected relation between total halo mass and the stellar mass of galaxies obtained by using the 'abundance matching' technique, i.e., by ranking galaxy halo masses from simulations with luminosities from observations and pairing them in the same order, shows that for galaxies with high halo mass, SN feedback is unable to stop the formation of stars and star formation is too efficient (e.g., see Kannan et al., 2014; Moster et al., 2010).

Star formation

Estimating accurate star formation rates in galaxies is critical for understanding the processes governing the formation and destruction of stars and their impact on galaxies. Stars form in cold and dense regions in galaxies containing molecular gas and dust, where the temperature is favourable for the dense clouds to be gravitationally bound. Individual stars are almost always unresolved in galaxies except in very few neighbouring galaxies. Therefore, the information about star formation comes from integrated light from young stars and gas around them in the ultraviolet (UV) and far-infrared (FIR) wavelengths and from nebular recombination lines. These measurements are direct tracers of young stars. The most common way to measure the star formation rate is to compare either UV/FIR continuum fluxes, nebular emission line fluxes or UV/visible wavelength spectra of galax-

Figure 1.3: A composite image of the M82 galaxy showing very hot ($\sim 10^7$ K) outflowing gas emitting X-rays (Blue); starlight in Optical (Green); $\sim 10^4$ K Hα emitting gas (Orange) and dust emission in Infrared (Red). Galactic winds driven by intense starburst with star formation rate of ~ 10 $M_\odot$ yr^{-1} at the centre blasting the gas and dust out of the galaxy are visible. Credit: X-ray: NASA/CXC/JHU/D.Strickland; Optical: NASA/ESA/STScI/AURA/The Hubble Heritage Team; IR: NASA/JPL-Caltech/Univ. of AZ/C. Engelbrecht.

ies or star-forming regions with empirical libraries of stellar populations of different ages, metallicities, star formation histories and initial mass functions (IMFs) (see Conroy, 2013, for review). Kennicutt (1998) has discussed methods used to estimate star formation rates which are summarized below.

Ultraviolet continuum: The ultraviolet wavelength spectrum of star-forming regions is dominated by light from young and massive stars. Therefore, the star formation rate scales linearly with UV luminosity. The optimal wavelength range is 1250–2500 Å which avoids contamination from older stars (Kennicutt, 1998). The conversion between measured UV continuum fluxes and star formation rates can be derived from stellar population models. Several studies have published these relations. One of the most commonly used relations is given by (Kennicutt, 1998)

$$\mathrm{SFR}(M_\odot\,\mathrm{year}^{-1}) = 1.4 \times 10^{-28} L_\nu(\mathrm{ergs\ s^{-1}\ Hz^{-1}}), \tag{1.4}$$

where L_ν estimated over the wavelength range 1500–2800 Å. This conversion relation assumes that star formation has remained constant over $\sim 10^8$ years (continuous star formation) and a Salpeter IMF (Salpeter, 1955) with mass limits 0.01 and 100 $M_\odot$.

Recombination lines: Stars with masses $\gtrsim 10$ $M_\odot$ and lifetimes of $\lesssim 20$ Myr contribute significantly in ionizing the gas around them. The ionized gas effectively re-emits the integrated stellar luminosities of galaxies through recombination lines providing another direct method to estimate star formation rates. The ionizing flux of stars is calculated using stellar population models. The most commonly used recombination line is the Hα line and the commonly used relation to estimate the star formation rate is given by (Kennicutt, 1998)

$$\mathrm{SFR}(M_\odot\,\mathrm{year}^{-1}) = 7.9 \times 10^{-42} L(\mathrm{H}\alpha)(\mathrm{ergs\ s^{-1}}), \tag{1.5}$$

which is derived based on the assumptions used to derive equation 1.4. Other recombination lines such as Hβ, Pα, and Pβ have also been used. Forbidden emission lines can also be used to estimate the SFR if H Balmer lines are not available. The [OII]λ3727 forbidden line doublet is often sufficiently strong and it has been calibrated empirically through Hα as an SFR tracer.

FIR luminosity: Interstellar dust absorbs a significant fraction of the light emitted by stars, primarily at UV wavelengths and re-emits it in the FIR wavelength (10–300 μm). Therefore, FIR emission can be a sensitive tracer of the young stellar population and the SFR. The effectiveness of FIR emission as the SFR tracer depends on the opacity of the interstellar medium and the age of the stellar population. In galaxies with young stars, most of the FIR dust emission is associated with young stars. In red galaxies containing mostly older stellar populations, dust emission is associated with older stars. Even though

there are ambiguities in the FIR emission, many studies have published calibrations for the FIR luminosity and star formation rate. For example, for a continuous starburst of age 10–100 Myr and assuming a Salpeter IMF, Kennicutt (1998) calibrated the following relation for starburst systems

$$\mathrm{SFR}(M_\odot\,\mathrm{year}^{-1}) = 4.5 \times 10^{-44} L_{FIR}(\mathrm{ergs\ s}^{-1}), \tag{1.6}$$

where L_{FIR} is the total integrated infrared luminosity between 8–1000 μm.

1.4.2 AGN feedback

A clue to solving this problem comes from the supermassive black holes (SMBH) that are found at the centres of almost all massive galaxies (Kormendy et al., 2011). The correlations observed between the SMBH masses and stellar velocity dispersions suggest that they co-evolve. In the Active Galactic Nucleus (AGN) feedback model, a large amount of gas initially cools down to the centre of the galaxy and accretes onto the central SMBH triggering AGN activity. The AGN powered by accreting black holes release a fraction ($f_{\rm acc} \sim 0.1$) of the potential energy lost by the accreted material as it falls into the potential well of a black hole, back into the surrounding gas in the form of radiation or kinetic outflows. We can compare the energy output of a black hole given by $\mathrm{E_{BH}} \sim f_{\rm acc}\mathrm{M_{BH}}c^2$, where $\mathrm{M_{BH}}$ is the black hole mass and c is the speed of light, to the binding energy of a galaxy bulge approximately given as $\mathrm{E_{bulge}} \sim \mathrm{M_{bulge}}\sigma^2$, where σ is the stellar velocity dispersion of the bulge. Using the relation between black hole and bulge mass, $\mathrm{M_{BH}} = 1.4 \times 10^{-3}\mathrm{M_{bulge}}$ (Häring & Rix, 2004), we can estimate the ratio of the two energies as $\mathrm{E_{BH}/E_{bulge}} \sim 1.4 \times 10^{-4} c/\sigma^2$. The stellar velocity dispersions are usually less than 400 km s^{-1}, resulting in $\mathrm{E_{BH}/E_{bulge}} \sim 100$. A galaxy with a mass of 10^{11} $\mathrm{M}_\odot$ typically has a central black hole of mass $\sim 10^8$ $\mathrm{M}_\odot$. The rest-mass energy of a black hole exceeds the galaxy's collective SN energy output. Thus even a small fraction of black hole energy released into the galaxy can have a profound effect on its host galaxy. The energy output of a black hole, therefore, is an order of magnitude greater than the SN energy output, regulating not only the black hole growth but the baryonic content of galaxies (Silk & Rees, 1998; Silk & Mamon, 2012, for review). AGN feedback operating in cycles has been suggested, where the energy released by AGN pushes the gas away and heats the surrounding atmosphere, thereby quenching the cooling flow and halting AGN activity and subsequently black hole growth. Without an AGN to disturb the cooling flow, the gas cools and the AGN activity resumes (Li et al., 2015; McNamara et al., 2016; Prasad et al., 2020; Nobels et al., 2022).

AGN feedback primarily operates in two modes, "quasar mode" also known as radiative feedback and "radio mode" also known as kinetic or mechanical feedback. While the quasar

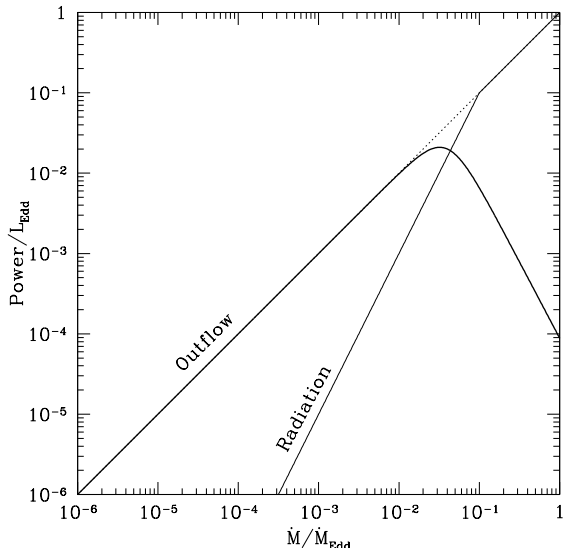

Figure 1.4: The figure shows the radiative efficiency of an AGN as a function of its accretion rate. As the accretion rate increases, the AGN becomes more and more radiatively efficient, whereas, in the low accretion limit, it is dominated by high mechanical efficiency (radio jets). The figure is taken from Churazov et al. (2005).

mode suppresses star formation and launches fast outflows on short time scales, the radio mode heats the atmospheres of galaxies on longer timescales suppressing cooling flows (see McNamara & Nulsen, 2007; Fabian, 2012, for reviews). Whether the AGN is in the quasar mode or radio mode is determined by the accretion rate onto the central SMBH.

The energy radiated away by material accreting onto SMBHs can be given as $L = \epsilon_r \dot{M}_{\rm acc} c^2$, where ϵ_r is the radiative efficiency of the AGN which is a strong function of the accretion rate $\dot{M}_{\rm acc}$. It is often useful to compare accretion rates to that of the Eddington accretion rate ($\dot{M}_{\rm acc}^{\rm Edd}$) to define mass accretion limits. The Eddington accretion rate is defined as the accretion rate when the outward radiation pressure of the AGN is comparable to the gravitational force acting on the infalling material. Thus, $\epsilon_r \dot{M}_{\rm acc}^{\rm Edd} c^2 \simeq L_{\rm Edd} \simeq 4\pi G M c/\kappa$, where κ is the opacity of the surrounding gas. At low accretion rates ($\dot{m}_{\rm acc} \equiv \dot{M}_{\rm acc}/\dot{M}_{\rm acc}^{\rm Edd} \equiv L/L_{\rm Edd} \equiv 10^{-3}$), the accreting material forms an optically thin, geometrically thick and radiatively inefficient hot disk with $\epsilon_r < 10^{-3}$ because of long cooling timescales (Yuan & Narayan, 2014). At moderate accretion rates ($\dot{m}_{\rm acc} \simeq 0.01$–$0.25$), the accreting material forms a cold (relative to the virial temperature) geometrically thin, optically thick and radiatively efficient disk with $\epsilon_r(\alpha_{\rm BH}) \simeq 0.05$–$0.2$, with efficiency increasing with increasing black hole spin ($\alpha_{\rm BH}$) (Novikov & Thorne, 1973;

Koratkar & Blaes, 1999). At even higher accretion rates, the accreted material forms an optically and geometrically thick disk that is radiatively inefficient with $\epsilon_r < 10^{-3}$, due to long radiative diffusion times (Sądowski et al., 2013, 2014; Sądowski & Narayan, 2015). This is illustrated in Fig. 1.4. The AGN operates in the quasar mode when it is in the radiatively efficient regime, otherwise, it operates in the radio mode.

1.4.3 Quasar mode feedback

The quasar mode feedback is commonly associated with highly luminous quasars at high redshifts. In the early Universe, mergers of galaxies left large reservoirs of gas and dust in galaxies. They fed the black holes forming powerful AGN that outshone their host galaxies. The first quasar was discovered as a point radio source (Schmidt, 1963). It was identified as a star because of its star-like appearance. However, follow-up spectroscopy of the object revealed very strong broad gas emission lines implying velocities of thousands of km s^{-1} with a very blue optical spectrum that was unlike any star. Therefore these objects were called "quasi-stellar objects" (QSOs) or "quasars". The most luminous quasars can have luminosities of up to 10^{47} erg s^{-1}.

The outflows driven by quasar mode feedback can be energy or momentum-conserving depending on whether radiative losses are negligible or not, respectively. When outflowing gas does not radiate away its energy within short dynamical times of the outflow, it is an energy-conserving outflow, otherwise, the outflow is momentum-conserving. In the energy-conserving outflow, energy injected in the surrounding gas gets converted into the bulk motion at a rate $\dot{E} \sim \dot{M} v_{\rm out}^2$, where $v_{\rm out}$ is the outflow velocity and $\dot{M}$ is mass outflow rate. Energy conserving flows driven by AGN scale with black hole mass and lead to $\rm M_{BH} \propto \sigma^5$, where σ is the stellar velocity dispersion (Silk & Rees, 1998; Murray et al., 2005). Whereas for momentum conserving flows, $\dot{E} \propto \dot{M} v_{\rm out}$ and it leads to $\rm M_{BH} \propto \sigma^4$ (King, 2003; Murray et al., 2005). Both relations lie close to the observed $M_{\rm BH}$–σ relation (Fabian, 2012).

The primary source of energy in quasar mode can come from thermal energy or radiation pressure. In the thermal pressure scenario, the shell of outflowing ambient gas is pushed by the ram pressure of the hot, over-pressured gas in the inner regions of the galaxy heated by the AGN. Essentially, the outflows of cold or atomic gas in this case are driven by hot winds produced by the AGN. X-ray observations of some galaxies have found such high-velocity ($\gtrsim$10,000 km s^{-1}) winds of hot, X-ray emitting gas driving cold outflows (Faucher-Giguère & Quataert, 2012; Tombesi et al., 2015). In this scenario, from energy conservation, it follows that $\dot{p}_{\rm out} = 0.5 \dot{M}_{\rm out} v_{\rm out}^2 = 0.5 f \dot{M}_{\rm wind} v_{\rm wind} = \dot{p}_{\rm wind}$, where the subscript "outflow" refers to the outer atomic or molecular outflow, "wind" refers to the hot inner wind driving

the outflow, f is the coupling factor which determines the fraction of the kinetic energy of the inner wind that is transferred to the outer outflow and $\dot{p}$ is the kinetic power of the outflow. Rearranging the terms, we get, $\dot{p}_{\rm out} = f(v_{\rm wind}/v_{\rm out})\dot{p}_{\rm wind}$. If the wind is driven by radiation pressure, $\dot{p}_{\rm wind} = L_{\rm AGN}/c$ and we get, $\dot{p}_{\rm out} = f(v_{\rm wind}/v_{\rm out})L_{\rm AGN}/c$. For wind-driven outflows, $\dot{p}_{\rm out} \sim 20L_{\rm Edd}/c$ and $\dot{E} \sim 0.05L_{\rm Edd}$ (Zubovas & King, 2012; King & Pounds, 2015).

Radiation from the AGN can also drive outflows of gas if it is efficiently coupled to the ambient gas and if the ratio of the radiation force to the gravitational force is greater than unity. The coupling of radiation to the gas is determined by the opacity of the gas per unit mass, κ, which depends on the gas density, dust-to-mass ratio and ionization parameter of the gas. If κ of the ISM is large enough, AGN radiation can couple effectively with the ambient gas and drive outflows (Ishibashi et al., 2018). In radiation-driven outflows, the momentum ratios $\dot{p}_{\rm out}/L_{\rm AGN}/c$ can reach values of up to 10 depending on the optical depth and dust content of the gas in the ISM.

A very well-studied example of quasar mode feedback is the galaxy Markarian 231. It hosts a powerful quasar at the centre driving outflows of atomic, ionized and molecular gas (Feruglio et al., 2010, 2015). The inner 1 kpc of this galaxy is devoid of a young stellar population suggesting AGN has stopped star formation in the centre (Davies et al., 2007; Lipari et al., 2009). AGN wind feedback has been detected in numerous other galaxies hosting strong, active AGN. For example, AGN winds and actively star-forming regions are spatially anti-correlated (Cano-Díaz et al., 2012; Cresci et al., 2015; Carniani et al., 2016). In summary, quasar mode feedback is powerful enough to clear gas in massive galaxies (Fiore et al., 2017).

1.4.4 Radio mode feedback

The second mode of AGN feedback is the radio mode or mechanical feedback. In radio mode feedback, gas accreting on the central SMBHs releases a fraction of their stored gravitational potential energy in the form of bipolar jets of energetic particles moving at relativistic speeds emanating from the vicinity of the black hole. While quasar-mode feedback is effective close to the AGN in inner parts of galaxies, radio-mode feedback injects energy at much larger scales. The energy injected by the radio jets into the surrounding atmosphere may be given as

$$\dot{E}_k = \epsilon_{f,k}\dot{M}_{\rm acc}c^2 \simeq 5.7 \times 10^{46}\,\epsilon_{f,k}(\dot{M}_{\rm acc}/M_\odot\,{\rm yr}^{-1})\ {\rm erg\ s}^{-1}, \tag{1.7}$$

where $\epsilon_{f,k}$ is the efficiency of the radio jet to couple to the surrounding gas and drive outflow (Veilleux et al., 2020). Although simulations of accretion disks suggest $\epsilon_{f,k}$ of 10^{-3}

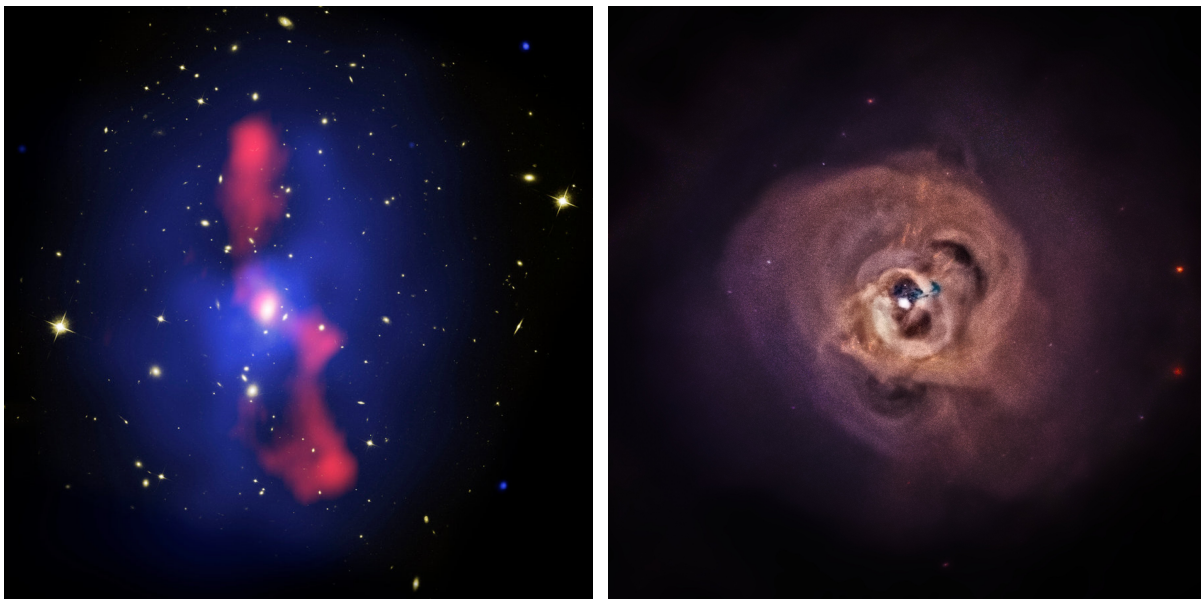

Figure 1.5: *Left*: Composite image of MS0735 cluster showing X-rays (blue), radio (red) and optical (yellow). Cavities in the X-ray emission carved by radio bubbles are clearly visible. Credit: By NRAO, and L. Birzan and team (Ohio University) - http://hubblesite.org/gallery/album/exotic/black_hole/pr2006051b/npp/all/, Public Domain, https://commons.wikimedia.org/w/index.php?curid=9910992. *Right*: *Chandra* X-ray image of the Perseus cluster showing disturbed X-ray cluster with cavities, shocks and sound waves. Credit: NASA/CXC/SAO/E.Bulbul, et al.

(Yuan & Narayan, 2014), the efficiency can be higher up to $\sim$ 3–8 % for spinning black holes with magnetized accretion disks (Sądowski et al., 2016). Radio jets deposit a large amount of energy in the atmospheres of galaxies and clusters heating their atmospheres. It is the primary candidate for suppressing the cooling of hot gas and star formation in galaxy clusters and all massive elliptical galaxies at late times (Bower et al., 2006; Croton et al., 2006; Mulcahey et al., 2022). Sufficient heating of the ambient atmosphere will suppress the cooling flows, starving the AGN of the fuel supply. In the absence of heating, cooling flow resumes and the cycle continues.

Although radio jets have been detected in many galaxies, cool-core galaxy clusters offer the clearest view of the radio-mode feedback owing to their dense and bright atmospheres. Radio mode feedback is evident in cool-core clusters and groups in which the radio jets blow bubbles into their hot atmospheres. The bubbles appear as cavities or surface brightness

depressions in the X-ray images of clusters and groups. The first detection of X-ray cavities was reported by Boehringer et al. (1993) and Carilli et al. (1994) for Perseus and Cygnus A clusters, respectively, using *ROSAT* satellite data. Since then, a wealth of high spectral and spatial resolution data from *XMM-Newton* and *Chandra* X-ray observatories detected X-ray cavities in almost all cool-core clusters they observed and have shown that radio mode feedback heats atmospheres of massive galaxies, clusters and groups, suppressing cooling flows. For example, the left panel of Fig. 1.5 shows an example of synchrotron radio jet emission (red) filling almost circular cavities seen in the X-ray emission (blue) of the MS0735 galaxy cluster. The spatial anti-correlation between radio lobes and X-ray cavities is evident. The right panel shows a *Chandra* X-ray image of the Perseus cluster showing shock fronts, cavities and sound waves produced by the mechanical feedback.

Measuring radio-mechanical power

The most effective way to gauge radio mechanical energy is by measuring the work done by radio jets in inflating cavities (McNamara et al., 2000). The cavities are likely filled with relativistic plasma with very high temperature and low density providing pressure support. In that case, the total enthalpy, i.e. the mechanical work done by cavities plus the internal energy providing pressure support is given by

$$E_{\rm cav} = \frac{\gamma}{\gamma - 1} pV = 4pV, \quad \text{for } \gamma = 4/3, \tag{1.8}$$

where γ is the ratio of specific heats of cavity plasma, p is the average pressure inside a cavity equal to the pressure of the surrounding ambient gas assuming that the cavity and the surrounding gas are in pressure balance and V is cavity volume. The cavity power can then be estimated as

$$P_{\rm cav} = \frac{E_{\rm cav}}{t_{\rm cav}}, \tag{1.9}$$

where $t_{\rm cav}$ is the age of the cavity. Cavity ages are determined assuming cavities rise buoyantly in the atmospheres of galaxies and clusters at their terminal velocity. The cavity age is then calculated as $t_{\rm cav} = R/v_{\rm term}$ where R is the distance of the cavity from the nucleus of the galaxy and $v_{\rm term}$ is its terminal velocity. Cavity powers are better estimators of kinetic powers in radio jets as radio synchrotron powers of radio jets represent a minor fraction of their kinetic power. The radio synchrotron power relies on the unknown ratio k of energies between non-radiating particles in the jets versus synchrotron emitting electrons assumed to lie in the range 0–100 (Willott et al., 1999). Low k would imply lower total mechanical power which may not be sufficient to offset cooling. A high value of k is

not confirmed by observations. However, large atmospheric pressures with values $\sim 10^{-10}$ dyn cm^{-2} and large cavity sizes with diameters ranging from $\sim$ 20 kpc to 200 kpc in the most extreme sources imply very large mechanical powers exceeding synchrotron powers of radio jets by up to two to three orders of magnitude (Bîrzan et al., 2008). The radio powers and cavity powers are correlated and follow a linear relationship in the log space given by (Bîrzan et al., 2004; Cavagnolo et al., 2010),

$$\log P_{\rm cav} = 0.75(\pm 0.14)\log P_{1.4} + 1.91(\pm 0.18), \tag{1.10}$$

where $P_{\rm cav}$ is the cavity power in units 10^{42} erg s^{-1} and $P_{1.4}$ is the radio power at 1.4 GHz in units 10^{40} erg s^{-1}. The most powerful clusters have cavity powers up to a few 10^{45} erg s^{-1} rivalling the power output of the powerful quasars. The measured cavity powers (10^{42} to 10^{46} erg s^{-1}) scale linearly with radiative losses from a galaxy cluster's core ($L_{\rm X-ray} \sim 10^{42-45}$ erg s^{-1}) implying that radio mechanical powers are sufficient to offset gas cooling in most systems (Rafferty et al., 2006). Cavity powers may be underestimated as they do not consider the power dissipated through shocks, sound waves, cosmic ray leakage, thermal conduction, turbulence and other forms of energy. It further strengthens the hypothesis that radio-mechanical AGN powers can offset cooling in galaxies and clusters.

1.4.5 Heating Hot Atmospheres with Radio mode feedback

The mechanical energy of the AGN needs to couple to the surrounding medium efficiently in order to offset cooling. Several mechanisms have been proposed for energy transport, however, their relative importance is unclear. Here we discuss some processes that can transfer AGN energy into the atmospheres of galaxies and clusters.

Weak shocks and sound waves

As cavities are blown and rise, they produce weak shocks in the ICM. However, weak shocks created by single AGN outbursts cannot cool the ICM at large scales. The timescale for shocks is smaller than the cooling time of the gas and the post-shock gas has a slightly lower pressure than before as it is raised to a higher radius where gravity is weak, leading to a small increase in the entropy of the gas. Although the impact of one weak shock is small, their cumulative impact can be significant (see for example Forman et al. (2007), Randall et al. (2011)). Still, weak shocks are unable to heat the ICM at large distances. They are, however, important at small distances close to the AGN, as shock strength decreases with radius but entropy increase is cubic in the shock strength (McNamara & Nulsen, 2012).

Similar to weak shock sounds waves can be seen in the Perseus cluster (see right panel of Fig. 1.5) driven by repeated AGN outbursts in the AGN of its BCG (Fabian et al., 2005). Sound waves dissipate energy through viscous dissipation and thermal conduction. The strength of sound waves depends on the square of the wave amplitude, meaning that it is effective at larger scales. Sound wave heating may provide sufficient heating to offset the cooling of ICM gas in clusters (Ruszkowski et al., 2004).

Turbulence, mixing and thermal conduction

As cavities rise buoyantly, they lift surrounding gas to higher altitudes. This gas then detaches and falls back towards the centre. This process can generate gravity waves, sound waves and turbulence that propagate outward, carrying the energy away from the cavities and eventually thermalizing it (Donahue & Voit, 2022). This energy transport depends on the properties of the ambient ICM such as its viscosity, thermal conduction coefficient, and magneto-hydrodynamic (MHD) wave interactions, which are uncertain and have large uncertainties making the energy transport process more complex.

Recently, turbulence has been proposed as a plausible mechanism for heating the ICM and offset radiative cooling (Zhuravleva et al., 2014). However, turbulent energy inferred from surface brightness fluctuations has large uncertainties making it inconclusive. *Hitomi* satellite directly measured the velocity field of the hot gas in the Perseus cluster with turbulent velocities of $\sim$160 km s^{-1}, equivalent to about 10% of the thermal pressure of the gas (Hitomi Collaboration et al., 2016). Thus the observed level of turbulent energy is insufficient to heat the cluster gas at large distances.

Cavity dissipation

As X-ray cavities rise, they are more susceptible to instabilities and should dissipate. When cavities are destroyed as a result of instabilities, heat is transferred to the ICM when ICM and lobe gases mix. While theory and simulations suggest cavities should be destroyed rapidly, observations suggest that they survive for long periods and rise to 100s of kiloparsecs (Bîrzan et al., 2004; Fabian et al., 2011). Moreover, cavity disruption can be delayed by magnetic confinement, viscosity, or favourable dynamics. Nevertheless, it can potentially transport energy into the atmosphere at much larger distances where most of the other mechanisms are less effective. Additionally, cosmic rays coming from within the bubble can propagate out via diffusion or streaming (Boehringer & Morfill, 1988; Sijacki et al., 2008). Streaming cosmic rays can excite plasma waves that can dissipate by heating the surrounding ICM.

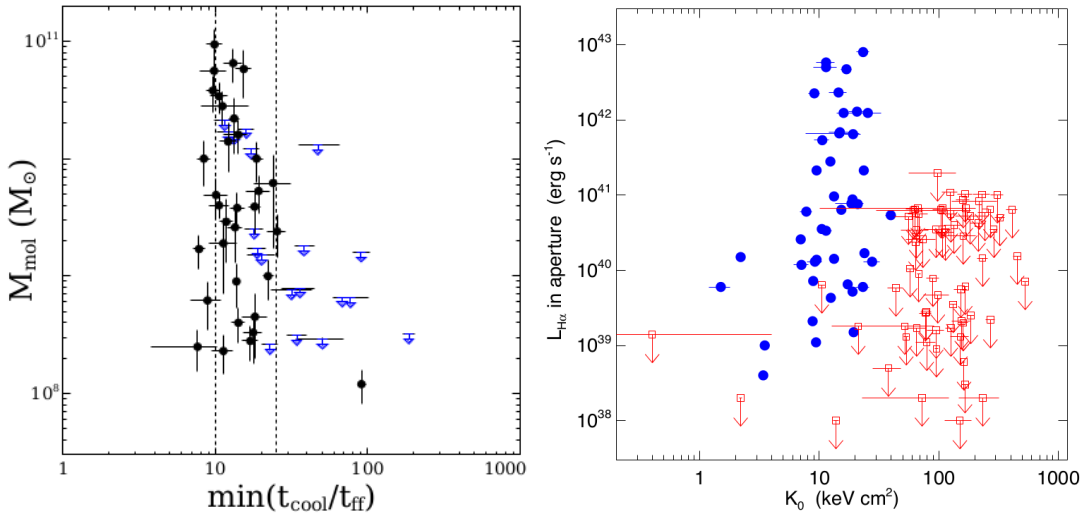

Figure 1.6: *Left*: The relationship between the molecular gas mass detected in clusters and the minimum $t_{\rm cool}/t_{\rm ff}$. All clusters with molecular gas detection (black points) have $\min(t_{\rm cool}/t_{\rm ff})$ lying between 10 and 25. The figure is taken from Pulido et al. (2018). *Right*: The relationship between Hα gas luminosity and the gas entropy in clusters from the ACCEPT database. All clusters with Hα gas detection (blue points) have central entropies less than 30 keV cm^2. The figure is taken from Voit & Donahue (2015).

The heating of the ICM by radio mode feedback is complex. Perhaps a combination of all of these processes is at play. However, their relative roles may change under different ICM conditions. More studies are required to study these processes in detail.

1.4.6 Residual cooling and the origin of cold gas

Even though radio mode feedback can effectively heat atmospheres of massive galaxies and clusters quenching cooling flows, observations have found large amounts of cold gas in cool-core clusters. Molecular gas masses as high as 10^{11} M$_\odot$ have been observed in BCGs. They correlate strongly with the total Hα luminosity and therefore with total star formation rates (SFRs) in BCGs. The most star-forming BCGs have star formation rates approaching 1000 M$_\odot$ yr^{-1}. Recent high-resolution observations show that the multiphase gas extends out to 20–30 kpc and that the cold and warm gas phases have similar velocities suggesting a common origin (Olivares et al., 2019). Therefore the hot X-ray emitting gas is cooling to low temperatures in the inner regions of galaxy clusters and massive galaxies.

Several authors have proposed models for gas cooling which are summarized below.

Thermal instabilities

The hot intracluster gas in cool core galaxy clusters is globally in thermal balance. However, it is locally thermally unstable. For example, imagine the motions of gas parcels in stratified atmospheres as the origin of thermal instabilities. An incompressible gas parcel in a hydrostatic atmosphere with a constant pressure gradient displaced vertically will oscillate about its equilibrium position at a frequency given by the Brunt-Väisälä frequency due to gravity and buoyancy forces that act in opposite directions. However, the gas in the ICM is compressible, which means that it cools in a timescale $t_{\rm cool}$ and free falls in a timescale $t_{\rm ff}$. As it cools and loses energy, it becomes denser and will sink deeper into the gravitational potential until it finds a new balance between gravity and buoyancy. If $t_{\rm cool}$ of the parcel of gas is much less than its $t_{\rm ff}$, it will cool faster than gravity is able to move it to its equilibrium level. By the time it reaches equilibrium, it would have cooled significantly resulting in a new equilibrium position much deeper into the cluster's gravitational potential corresponding to its increased density. If $t_{\rm cool}$ is longer than $t_{\rm ff}$, it will oscillate about its equilibrium at the Brunt-Väisälä frequency resulting in no runaway cooling. Analytical arguments and simulations show that in cluster atmospheres, thermal instability ensues when $t_{\rm cool}/t_{\rm ff} \lesssim 1$ criteria is reached (Nulsen, 1986; McCourt et al., 2012). When this happens, density perturbations form dense blobs of gas that cool to low temperatures which then decouple from the hot atmosphere.

However, observations of galaxy clusters show that minimum $t_{\rm cool}/t_{\rm ff}$ ratio never reaches 1. Pulido et al. (2018) showed that cool-core clusters have detectable levels of cold gas when the ratio of their cooling time to free-fall time, $t_{\rm cool}/t_{\rm ff}$, lies between 10 and 25 (see left panel of Fig. 1.6). It is equivalent to a cooling time of less than 1 Gyr and entropy of less than 30 keV cm^2 at 10 kpc (see right panel of Fig. 1.6). The sharp transition in both cases indicates that the multiphase gas is more closely associated with the dynamical time of the central galaxy rather than cosmological cooling time. The most likely hypothesis is that when these thresholds are met, thermal instabilities ensue leading to the condensation of gas.

Precipitation model

Several models called "precipitation models" proposed that thermal instabilities in cluster atmospheres ensue when $\min(t_{\rm cool}/t_{\rm ff}) \leq 10$ (Voit & Donahue, 2015). According to these

models, when this condition is satisfied, cold gas condenses and falls back towards the central SMBH increasing the accretion rate of the AGN. The AGN fueled by accretion releases powerful jets and heats the surrounding atmosphere driving the $\min(t_{\rm cool}/t_{\rm ff})$ ratio above 10, suppressing the condensation of cold gas without completely eliminating molecular gas. Eventually, reduced cooling reduces accretion and the atmosphere starts to cool down again driving the $\min(t_{\rm cool}/t_{\rm ff})$ below 10 and the cycle repeats. However, the atmosphere does not react to the heating due to AGN instantly. The $\min(t_{\rm cool}/t_{\rm ff})$ changes gradually over time similar to a hysteresis cycle, where a property of a system lags behind changes in the effect causing it. As a result, the cold gas is preferentially observed when $\min(t_{\rm cool}/t_{\rm ff})$ falls between 4–20 (Voit et al., 2020) and 1–20 (Li et al., 2015).

Uplift models

While some systems are consistent with the $\min(t_{\rm cool}/t_{\rm ff}) \lesssim 10$ criteria, there are some exceptions. For example, Martz et al. (2020) showed that in some BCGs the above criteria are observed, yet those BCGs are either devoid of cold gas or have a substantially low amount of cold gas. Recent ALMA observations have revealed that fast-moving molecular gas clouds spatially coincide with outflows of hot gas suggesting that the hot gas is uplifting the molecular gas (Russell et al., 2019). The density contrast between the cold and hot gas is $\gtrsim 10^5$, and yet hot gas appears to be pushing the cold gas. Motivated by these observations, McNamara et al. (2016) suggested a mechanism called "stimulated feedback", where buoyant bubbles blown by radio jets lift low-entropy gas in central regions of BCGs to high altitudes. Condensation of uplifted gas can happen when its cooling time is less than its infall time, i.e. $t_{\rm cool}/t_{\rm I} \lesssim 1$, where infall time $t_{\rm I}$ is the time it takes the gas to fall back to its original altitude. In addition to the filamentary structure of molecular gas observed in BCGs, their observed linewidths are narrow suggesting that the gas hasn't had enough time to respond to its gravitational environment and it has formed recently and in-situ from uplifted cold X-ray emitting gas (Russell et al., 2019). Uplift is now a part of many radio mode feedback simulations and gas cooling models. For example, Voit et al. (2017) have proposed a model where the atmosphere is divided into inner and outer regions where thermal instabilities can ensue promoting gas cooling. The inner region encompasses the area from the centre of the BCG to a distance where $\min(t_{\rm cool}/t_{\rm ff})$ occurs. Outside this region, hot gas needs to be uplifted to higher altitudes for thermal instabilities to occur consistent with the stimulated feedback model.

Turbulent cooling

It has been shown that radio jets and the uplift of cavities cause some level of atmospheric turbulence. X-ray surface brightness fluctuations (Zhuravleva et al., 2014) and velocity structure functions (Li et al., 2020; Qiu et al., 2021; Hu et al., 2022a) of multiphase gases have put constraints on the turbulent velocities. However, these estimates have large uncertainties. Nevertheless, vertical motion induced by turbulence can promote gas condensation similar to the bulk uplift of gas. Turbulent motions strong enough to lift gas to a higher altitude where its cooling time is smaller than its turnover time due to turbulent eddies ($t_{\rm edd}$) can stimulate cooling (Gaspari et al., 2018). Strong turbulence will shred and mix the gases (Banerjee & Sharma, 2014), whereas weak turbulence fails to overcome the buoyancy effects that suppress cooling (Donahue & Voit, 2022).

Additionally, cosmological infall of low-entropy gas (Donahue & Voit, 2022), rotational motions of galactic atmospheres (Sobacchi & Sormani, 2019), gravity waves (Voit et al., 2017) and convection (Binney & Tabor, 1995; Pizzolato & Soker, 2005; Meece et al., 2017) can also stimulate gas condensation (see Donahue & Voit, 2022, for the discussion and review).

1.4.7 Positive AGN feedback

As discussed above, AGN feedback is invoked in order to suppress star formation in massive galaxies to reproduce the galaxy luminosity function and solve the cooling flow problem. Indeed cosmological simulations including strong AGN and star formation feedback have been able to match the observations. However, the details of coupling between feedback energies and the surrounding gas need to be investigated further. From an observational point of view, the impact of AGN feedback on star formation in host galaxies is still not well understood.

Recent observations of radio jets interacting with the local ISM of galaxies show that radio jets may not only suppress the star formation but trigger star formation locally in the region of direct interaction (Zinn et al., 2013; Cresci et al., 2015; Salomé et al., 2015). Both phases can exist in a galaxy simultaneously or at different times. Simulations and analytical studies also suggest that radio-jets can trigger star formation in host galaxies with star formation rates of up to 100 $M_\odot$ yr^{-1} (Gaibler et al., 2012; Wagner et al., 2012; Ishibashi & Fabian, 2014). Local studies show that radio jets can induce star formation even if the ambient medium is only moderately dense. This leads to a possibility that this mode of star formation was more common in the past when the AGN activity was more prevalent and the gas densities were higher.

1.5 This Thesis

It has been established that AGN and starburst feedback are an integral part of galaxy formation and evolution. These disparate modes of feedback not only heat the atmospheres of galaxies preventing the over-cooling of gas, but they drive outflows of gas starving the galaxies of fuel to form stars and stopping the growth of their black holes. The goal of the thesis is to study whether the radio-mechanical feedback is capable of driving cold galactic outflows and suppressing star formation, study the nature of star formation triggered by radio mode feedback and its implications for galaxy formation and evolution and study whether the stimulated AGN feedback mechanism can explain the origin of cold gas filaments observed in BCGs.

Outflows driven by quasar mode feedback have been observed and discussed in the literature. Radio mode feedback is mainly thought to maintain hot atmospheres of massive galaxies at late times. They both influence and contribute to the evolution of galaxies, however, the relative importance of these different feedback mechanisms is debated. Cicone et al. (2014) and Fluetsch et al. (2019) studied gas outflows driven by different feedback mechanisms in nearby early-type galaxies and showed that AGN feedback dominates in galaxies hosting AGN, whereas, in starburst galaxies with no AGN, outflows are driven by starburst feedback. However, they did not find a correlation between radio jets and gas outflows and concluded that radio mode feedback does not play a major role in driving gas outflows. In chapter 2 of this thesis, I analyzed spatially resolved molecular gas observations in a sample of 14 BCGs taken with ALMA to characterize the molecular gas flows driven by radio mode feedback. We compared them with flows observed in nearby galaxies to understand the relative roles played by different feedback mechanisms and their effectiveness in driving gas outflows.

As discussed in section 1.4.7, radio mode feedback can trigger star formation in galaxies locally, possibly contributing to the inside-out growth of galaxies. Direct, high spatial resolution, multiwavelength observations of radio-jet triggered star formation in a galactic gas flow are very limited. In chapter 3, I studied an excellent example of radio-jet triggered star formation in the BCG of the galaxy cluster Abell 1795 using high spatial resolution multiwavelength data from UV to radio wavelengths. I estimated the star formation rate, and the star formation efficiency and studied the role of radio jets in driving supersonic shocks and turbulence in the surrounding gas.

In chapter 4 of this thesis, I study gas cooling via stimulated feedback by uplift in a sample of cool-core galaxy clusters. Multiphase gas is found within central 20–30 kpc in galaxy clusters. I test whether the stimulated feedback mechanism is a viable model to

explain observed levels of cold gas in galaxy clusters by estimating the ability of cavities to lift gas and the distances to which the hot gas needs to be lifted as well as the amount of gas that can cool within the ages of cavities through different gas cooling mechanisms. Finally, in chapter 5, I summarise this thesis and its main conclusions.

Chapter 2

Molecular Flows in Contemporary Active Galaxies and the Efficacy of Radio-Mechanical Feedback

The radio-mechanical feedback is thought to heat the heat atmospheres of massive galaxies preventing overcooling of the gas at late times. Although some simulations suggest that radio-mode feedback can drive gas outflows, most AGN feedback studies exclude radio-mode feedback as a plausible outflow-driving mechanism. BCGs offer excellent laboratories for studying the impact of radio-mechanical feedback, because of their dense atmospheres, cavities blown by radio jets are easily visible and recent high spatial resolution molecular gas observations have shown molecular gas in filaments behind or directed towards bubbles. Therefore, I studied molecular gas flows in cool-core BCGs to study the properties of their molecular gas flows and the role of radio-mechanical feedback in driving these flows.

The work in the following chapter contains original research and has been published in Tamhane et al. (2022). I analyzed the archival ALMA data and wrote the manuscript. The second author B. R. McNamara is my supervisor and significantly edited sections 7 and 10 in the manuscript corresponding to sections 2.7 and 2.10 in the following chapter. Other authors are collaborators who improved the manuscript by providing comments.

2.1 Abstract

Molecular gas flows are analyzed in 14 cluster galaxies (BCGs) centred in cooling hot atmospheres. The BCGs contain $10^9 - 10^{11}$ $M_\odot$ of molecular gas, much of which is being moved by radio jets and lobes. The molecular flows and radio jet powers are compared to molecular outflows in 45 active galaxies within $z < 0.2$. We seek to understand the relative efficacy of radio, quasar, and starburst feedback over a range of active galaxy types. Molecular flows powered by radio feedback in BCGs are ∼10–1000 times larger in extent compared to contemporary galaxies hosting quasar nuclei and starbursts. Radio feedback yields lower flow velocities but higher momenta compared to quasar nuclei, as the molecular gas flows in BCGs are usually ∼10–100 times more massive. The product of the molecular gas mass and lifting altitude divided by the AGN or starburst power — a parameter referred to as the lifting factor—exceeds starbursts and quasar nuclei by two to three orders of magnitude, respectively. When active, radio feedback is generally more effective at lifting gas in galaxies compared to quasars and starburst winds. The kinetic energy flux of molecular clouds generally lies below and often substantially below a few per cent of the driving power. We find tentatively that star formation is suppressed in BCGs relative to other active galaxies, perhaps because these systems rarely form molecular disks that are more impervious to feedback and are better able to promote star formation.

2.2 Introduction

The energy released by active galactic nuclei (AGN) and star formation is able to lift and perhaps expel interstellar gas (ISM) in galaxies at all epochs. Gaseous outflows of ionized, atomic, and molecular gas delay and suppress star formation in galaxies, affecting their evolutionary paths (Alatalo et al., 2011; Maiolino et al., 2012; Aalto et al., 2012; Cicone et al., 2012; Combes et al., 2013; Veilleux et al., 2013; Tombesi et al., 2015; Feruglio et al., 2015; Rupke et al., 2017). For example, energetic feedback from starburst winds and AGN may imprint the correlation between stellar velocity dispersion of the host galaxy bulges and the supermassive black holes (SMBHs) masses (Fabian, 2012; King & Pounds, 2015; Croton & Farrar, 2008; Bower et al., 2008) and may prevent galaxies from growing to much larger sizes (Scannapieco & Oh, 2004; Beckmann et al., 2017). Burgeoning galaxies at redshift 2 are maintained on the main sequence of galaxy formation by in- and outflowing gas propelled by star formation and AGN (Tacconi et al., 2020).

Observations have established that outflows from galaxies that host powerful AGN are primarily powered by the AGN (Cicone et al., 2014). In the most massive galaxies,

two primary forms or modes of AGN feedback are thought to operate during a galaxy's lifetime: the radio and quasar modes (Bower et al., 2006; Croton et al., 2006). During the quasar mode, nuclear winds drive large-scale outflows of gas (Tombesi et al., 2015). These winds are thought to eject interstellar gas from the nascent galaxy which suppresses star formation and accretion onto the central SMBH (Fabian, 2012; Veilleux et al., 2020). The mode, quasar or radio, is thought to be governed by the specific accretion rate onto the black hole (Churazov et al., 2005). For accretion rates lower than a few percent of the Eddington rate, radio-mechanical feedback ensues (Russell et al., 2013). Accretion rates approaching the Eddington rate produce a quasar.

The $M - \sigma$ relation is thought to have been imprinted by quasars accreting near the Eddington rate following major mergers (Kauffmann & Haehnelt, 2000a). Whether an Eddington flow conserves energy or momentum is consequential to the form and development of the $M - \sigma$ relation. A hot, adiabatic wind whose radiative cooling timescale exceeds the outflow timescale conserves energy. Energy conserving winds lead to $M - \sigma$ relations scaling as σ^5 (Silk & Rees, 1998; Haehnelt et al., 1998). The accretion energy released during the growth of a nuclear black hole vastly exceeds the potential energy of the host and thus must couple inefficiently to the surrounding gas (Fabian, 2012; King & Pounds, 2015). A wind accelerated and heated by shock fronts whose cooling time scale lies below its expansion timescale conserves momentum (Zubovas & King, 2014). In momentum-conserving outflows, the shocked wind radiates away its kinetic energy and compresses into a dense gas. Ram pressure is communicated to the ISM driving outflows to a kiloparsec and perhaps beyond (Zubovas & King, 2012; King & Pounds, 2015). Momentum conserving winds lead to σ^4 scaling (Fabian, 1999; King, 2003; Murray et al., 2005) which lies close to the observed $M - \sigma$ relation (Fabian, 2012).

If the optical depth of dust in the ISM is greater than that due to Thomson scattering, the coupling between AGN radiation and dust can be significant. In that case, radiation pressure can power an outflow (Ishibashi et al., 2018). Depending on the optical depth of the medium around the AGN and the dust content, momentum ratios $\dot{p}/(L_{\rm AGN}/c)$ can reach values of up to 10 or higher in sources with high AGN luminosity and high dust content, with large covering fraction leading to higher coupling efficiency. The power ratio $(\dot{E}/L_{\rm AGN})$ can be greater than 0.01.

During radio mode feedback, jets launched from SMBHs inflate bubbles in the surrounding hot atmosphere, many of which are observed as surface brightness depressions or cavities in X-ray images. Atmospheric heating by a combination of shock fronts (Randall et al., 2011), turbulence (Zhuravleva et al., 2014), and enthalpy released as the cavities rise suppresses and often neutralizes cooling and star formation (McNamara & Nulsen, 2007, 2012; Fabian, 2012). As the bubbles rise, they lift low entropy, metal-rich gas that

is dispersed in the inner several 10s of kiloparsecs of the cluster (Nulsen et al., 2002; Kirkpatrick & McNamara, 2015; Simionescu et al., 2008; Gitti et al., 2011). Some of this gas may cool and condense in the bubbles' updrafts into molecular clouds (Revaz et al., 2008; McNamara et al., 2016; Voit et al., 2017). Molecular gas is plentiful in brightest galaxies (BCGs) residing at the centres of cool-core clusters, groups and galaxies (Edge et al., 2002; Salomé & Combes, 2003; Pulido et al., 2018; Russell et al., 2019; Olivares et al., 2019).

In Galactic outflows detected in ionized, neutral, and molecular forms, molecular gas flows usually contain most of the mass. Molecular clouds directly fuel star formation and nuclear black holes. Therefore, they have the greatest potential impact on the evolution of galaxies. Several investigations have explored outflow properties including size, mass, velocity, and their relationships to galaxy morphology, AGN luminosity, star formation rate, and stellar mass. Cicone et al. (2014) found a trend between AGN luminosity and outflow rate. They also found that in starburst galaxies, the ratio of mass outflow rate to star formation rate, dubbed the loading factor, is typically $\sim$ 1–4 but increases to upwards of 100 for the most powerful AGN.

Fiore et al. (2017) found that AGN winds are a dominant driving mechanism in massive galaxies at redshifts of two and below. They concluded tentatively that winds are capable of sweeping or destroying molecular gas in massive galaxies. Most studies have focused on relatively small, heterogeneous samples. Fluetsch et al. (2019) compiled a sample of relatively nearby galaxies to study these relations with an eye to understanding selection biases. They found that outflows can be both energy-conserving and radiation pressure driven, and that less than five percent of the gas escapes the host galaxies. No correlation was found between molecular gas outflow rates and radio power. Nevertheless, several instances of jet-powered outflows are known (Morganti et al., 2015, 2013; Mahony et al., 2016).

Radio mode or radio/mechanical feedback is thought to be the agent maintaining the inner cooling regions of hot atmospheres thus preventing star formation in massive galaxies at late times. ALMA observations of central galaxies in clusters with cooling atmospheres have revealed a far more complex picture (Russell et al., 2019; Olivares et al., 2019). While stellar populations in most central galaxies are usually old, those in cooling core clusters are instead often rich in molecular gas and star formation (Edge, 2001; Salomé & Combes, 2003; O'Dea et al., 2008; Donahue et al., 2015). For the past two decades, the Chandra and XMM-Newton observatories have characterized the hot X-ray emitting atmospheres in and around BCGs with fine detail, revealing multi-phase, cooling atmospheres. Detailed observations of the molecular gas content are available for only a dozen systems or so. These studies have revealed molecular gas filaments trailing behind buoyantly rising X-ray cavities and interacting with radio lobes (McNamara et al., 2014; Russell et al., 2014, 2016,

2017a,b; Vantyghem et al., 2016, 2018). These spatial correlations indicate that radio AGN are disrupting and perhaps expelling molecular gas from the central galaxies. Molecular gas may also condense in the updrafts of rising radio bubbles (McNamara et al., 2014, 2016; Russell et al., 2019).

Here we analyze molecular flows in central galaxies and compare them to those in active galaxies from the Fluetsch et al. (2019). Fluetsch did not include outflows driven by radio-mode feedback in central galaxies. In fact, most studies neglect radio-mode feedback as an effective mechanism for driving massive outflows. Our goal is to understand the relative impact these disparate modes of feedback can have on the evolution of galaxies.

In recent years, the Atacama Large Millimeter/submillimeter Array (ALMA) has observed molecular gas in central galaxies with unprecedented spatial and velocity resolution. This combined with sensitive X-ray imaging and nebular line spectroscopy has provided a vivid picture of radio-mode feedback. Such work has revealed some of the most massive molecular gas flows known in the universe. Here we examine ALMA observations of BCGs to decompose the flow and non-flow components. We investigate the relative efficiency and driving power of different feedback modes and we examine their roles in suppressing star formation.

Throughout this chapter, we adopt $H_0 = 70$ km s^{-1} Mpc^{-1}, $\Omega_M = 0.3$ and $\Omega_\lambda = 0.7$.

2.3 Sample selection

Archival ALMA observations of 12 BCGs were analyzed. All targets in our sample lie below a redshift of 0.6 and span the range in the molecular gas mass of 10^7 – 10^{11} M$_\odot$. Star formation rate ranges between a few to ~ 600 M$_\odot$ yr^{-1} and radio mechanical AGN power between 10^{42} – 10^{46} erg s^{-1}. Their stellar masses are greater than 10^{11} M$_\odot$. These properties are summarized in table **??**. Most ALMA archival targets were observed based on their large molecular gas reservoirs (Edge et al., 2002; Pulido et al., 2018). Therefore, our sample is biased, incomplete and does not represent all central cluster galaxies. We consider this bias throughout our analysis. We have included NGC 1275, the central galaxy in the Perseus cluster, observed with the IRAM telescope (Salomé et al., 2011).

The Fluetsch et al. (2019) sample of 45 galaxies with gaseous outflows lies within redshifts of $z < 0.2$ and has stellar masses lying between $10^{10.5}$–10^{12} M$_\odot$, with the majority of galaxies having stellar masses upward of 10^{11} M$_\odot$, comparable to the stellar mass of BCGs in our sample. They include four ULIRGs for which the molecular properties were determined from far-infrared OH transitions. They classify galaxies as Seyfert, low-ionization

nuclear emission-line region (composite) and starburst (star-forming) galaxies based on the BPT-[SII] diagram. They include galaxies with flows in neutral and ionized phases. We refer to these categories as AGN, composite, and starburst galaxies, respectively. Although Fluetsch et al. (2019) sample does not provide a census of molecular outflows in galaxies, it is sufficiently large to derive scaling relations between outflows and galaxy properties, given the lack of high sensitivity millimetre data for a large, volume-limited or mass-limited sample of galaxies. Their sample is still biased as it primarily contains galaxies with enhanced star formation or known AGN. Nevertheless, it is still the largest sample of molecular flows in nearby galaxies spanning a wide range of AGN powers with molecular outflows powered by AGN winds/radiation as well as starbursts. However, their sample does not contain flows driven by radio mode feedback. Therefore, it makes a good reference sample to compare to central galaxies in which the flows are primarily driven by radio mode feedback and some which also host luminous AGN and starbursts, in order to study the relative efficacy of different driving mechanisms. Except for Phoenix, all other BCGs in our sample are at or below a redshift of 0.2 allowing us to compare molecular flows and their driving mechanisms in contemporary galaxies with stellar masses lying within a factor of a few as well as comparable AGN power output. Although galaxies in the two samples reside in different environments, it is likely that most of the galaxies in the Fluetsch et al. (2019) sample have gone through a phase of radio AGN activity during their evolution. Therefore, this comparison is a first step towards understanding the relative impact of radio-mechanical feedback when active compared to other outflow driving mechanisms assuming the radio-jet feedback operates in a similar way in other galaxies as it does in BCGs.

2.4 Data Analysis

We used automated science pipeline scripts provided by ALMA with the data sets to reduce and calibrate the data. For Cycle 0 Early Science data (Abell 1835 and Abell 1664), scripts were modified according to instructions provided on the ALMA website[1] to re-calibrate the data with CASA 4.2. All other data were processed in CASA version 4.7.2. Additional flagging was done for some BCGs such as phase centre correction (Abell 1835), total flux calibration (Phoenix) and self-calibration was performed on some datasets to improve the signal-to-noise.

CASA tasks UVCONTSUB and CLEAN were used to subtract the continuum and generate image data cubes, respectively. We used Briggs weighting with parameter 2 to improve

[1] https://casaguides.nrao.edu/index.php/Updating_a_script_to_work_with_CASA_4.2

sensitivity to faint filaments. The rms noise in the data cubes was found to be close to the theoretical rms.

2.5 Comparison of Molecular Flow Sizes, Speeds, Masses and Power

The outflows studied by Fluetsch are generally unresolved spatially due to their small angular sizes. Their masses and velocities were measured by fitting at least two gaussians to the molecular gas velocity profiles. The area and width of the broader gaussian component provided mass and velocity estimates. In some cases, the flows are resolved and visibly surround the galaxy. However, their morphologies are usually indiscernible due to their small angular sizes.

In contrast, the flows in cluster centrals (BCGs) are well resolved with a variety of morphologies and velocity patterns. Molecular gas in BCGs is often filamentary, extending out from the center with multiple spectral components (Russell et al., 2019; Olivares et al., 2019). In most galaxies, the molecular gas lies outside of the nucleus in an unsettled state. Molecular clouds are rarely observed in ordered motion about the nucleus, as they are in AGN hosting and other galaxies. We consider this off-nucleus gas as a flow in BCGs. Some of this gas may be flowing towards the BCG as opposed to a pure outflow. A simple, comprehensive characterization of their flows that can be compared to the Fluetsch et al. (2019) systems would be desirable.

Although some filaments have smooth velocity gradients, they are much more extended compared to the sizes of molecular gas disks observed in galaxies (Rose et al., 2019b; Boizelle et al., 2017). Their position-velocity (PV) diagrams do not show the characteristic 'S'-shaped curve that represents rotation (see Fig. A2). Some of the molecular gas in A1664 may be forming a disk of molecular gas in the centre (Russell et al., 2014). Similarly, the circumnuclear gas reservoir in phoenix has a smooth velocity gradient from -200 to 200 km s^{-1} suggestive of a disk (Russell et al., 2017a). But the extended filaments that we consider as flows have distinct velocity structures from the circumnuclear gas. Molecular gas disks are detected in very few BCGs such as HydraA (Rose et al., 2019b) and Abell 262 (Russell et al., 2019). We have excluded those BCGs from our sample. In the following subsections, we describe the process of estimating flow properties in BCGs and compare them to flows in the Fluetsch sample.

2.5.1 Flow velocities

Spectra from data cubes were extracted in beam-sized regions centered on each pixel in the entire emission region. They were fitted with a model consisting of one Gaussian component using the LMFIT Python package[2]. A significance of greater than 3σ was imposed for the detection of line emission, evaluated by performing 1000 Monte Carlo iterations. Integrated CO images and velocity centroid maps of BCGs analyzed here are presented in Appendix 1.

Fluetsch et al. (2019) identified outflows spectroscopically, based primarily on the detection of two velocity components in the spectrum of the entire emission region. They calculated flow speed using $\mathrm{FWHM_{broad}}/2 + |v_{\mathrm{broad}} - v_{\mathrm{narrow}}|$, where $\mathrm{FWHM_{broad}}$ is the full width at half maximum of the broad component in the extracted spectrum of the source and v_{broad} and v_{narrow} are the mean speeds of broad and narrow components. This method can be applied only when narrow and broad components are identified. In the absence of multiple components, Fluetsch concluded non-detection of an outflow. To allow for a comparison to their method, we extracted spectra in the entire emission region including all emission structures and fit them with one or two Gaussian components. The prescription described above was applied to estimate outflow velocities in BCGs according to their method.

The outflows in many Fluetsch galaxies are barely resolved spectrally and few are resolved spatially. Therefore, the outflow speeds and gas masses must be large enough for the spectrum to deviate from gaussianity. Applying this method to Abell 2597, Abell 1835, AS1101 and NGC4696, the summed spectra deviate only marginally from gaussianity. Their flows would therefore have been missed were they too distant to be spatially resolved. Nevertheless, some of these systems harbor some of the most massive molecular gas flows known.

We identify gas flows in BCGs and determine their velocities and sizes individually from spatially extended emission components. Gas speeds were estimated as flux weighted average speed along the spatially extended filaments or clumps of gas from their velocity maps within regions we considered as flows. The regions and the corresponding velocity maps are shown in the Appendix. If more than one filament or clump is present, the average speeds of all extended components are considered as the flow speed. Figure 2.1 compares Fluetsch's methodology to ours in systems where both methods can be applied. The flow speeds estimated using the two methods are correlated with a Pearson correlation coefficient of 0.77 and a p-value of 0.001. Speeds estimated using the Fluetsch method are

[2] https://lmfit.github.io/lmfit-py/

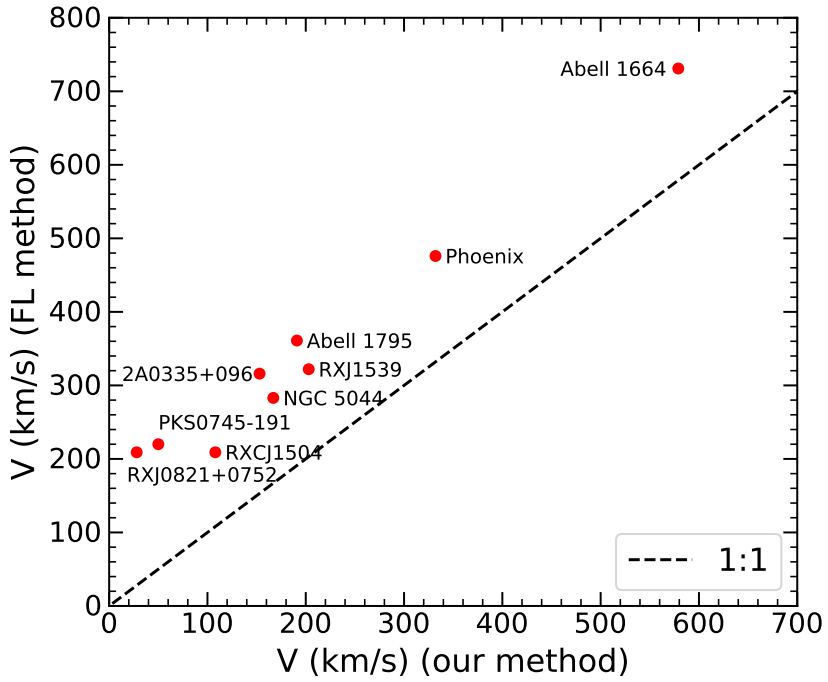

Figure 2.1: Comparison of flow speeds estimated using the Fluetsch method against our method. The black dashed line is the 1:1 relation.

two times higher compared to our method, except for RXCJ0821. The molecular gas in RXCJ0821 lies in two clumps north of the BCG's nucleus. Their mean velocities are close to the BCG's systemic velocity. However, their FWHMs are significantly larger than their mean relative velocities, yielding much higher flow velocities using the Fleutsch method. The Fluetsch method captures a small fraction of the gas that is flowing at high speeds and overestimates the flow velocity. In what follows, we adopt speeds estimated using our method. However, were we to adjust Fluetsch velocities to velocities obtained using our method by dividing them by a factor of two, it does not change our results qualitatively (see Appendix A.2).

Figure 2.2 shows the distribution of flow speeds for all systems. BCG flow speeds lie in the range 50–300 km s^{-1} with a mean of 173 km s^{-1}. Abell 1664 with a speed of 579 km s^{-1} is a moderate outlier. By comparison, the flow speeds of starburst and AGN galaxies lie in the range 50–600 km s^{-1} and 100–800 km s^{-1}, respectively. The mean outflow velocity for AGN and starburst galaxies is 447 km s^{-1} and 243 km s^{-1}, respectively. Thus BCG flow speeds on average lie ∼60% below AGN hosting galaxies but are similar to starburst

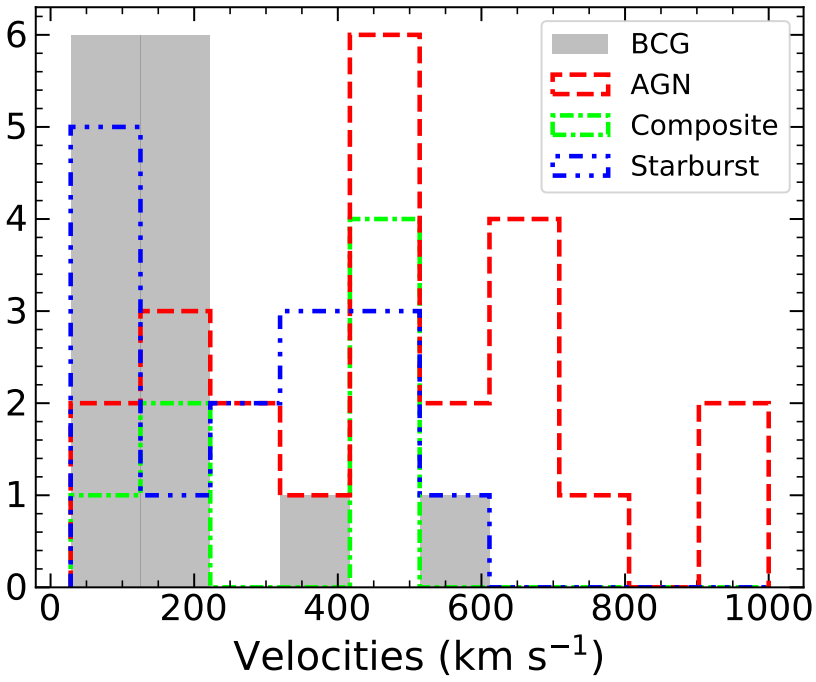

Figure 2.2: The distribution of flow speeds in BCG, AGN hosting, composite and starburst galaxies. The flows in BCGs have relatively lower speeds compared to AGN hosting galaxies.

galaxies.

2.5.2 Flow sizes

Flow projected sizes are determined from the projected lengths of the filaments in ALMA CO images. The velocity profiles of the gas in filaments in most BCGs are distinct from the gas in the central regions of BCGs. Filamentary gas in cluster central galaxies generally has narrow velocity widths with full width at half maximum velocities $\lesssim$100 km s^{-1} and mean recessional speeds of several hundred km s^{-1}. These filaments are considered off-nuclear flows. To examine the filaments we imaged the data cube over the velocity ranges observed in the filament. We then measured the filament sizes from the BCG nucleus to the most distant part of the filament. When multiple filaments are present their sizes are averaged. For example, PKS0745 has three long filaments in the SE, NW and SW directions. We

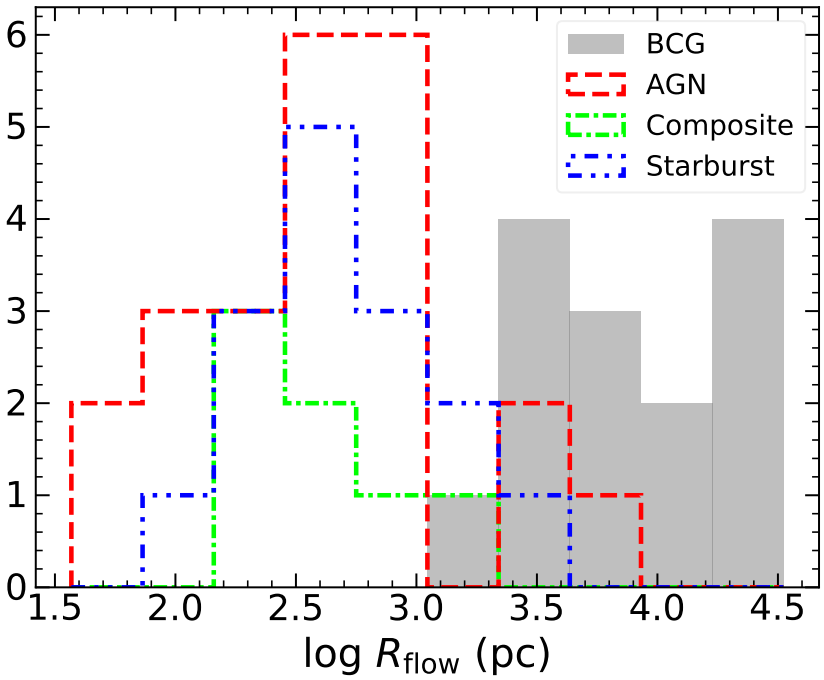

Figure 2.3: Histogram of flow radii in BCGs, AGN, composites and starburst galaxies.

take the length of each filament from the BCG center marked as **x** in Figure A.1 to the average outermost edge of the filament as the size of the flow.

In Figure 2.3 a histogram of flow size in BCGs, AGN hosting, composites and starburst galaxies are presented. BCG flow sizes generally range between 2 and 15 kpc. Phoenix, RXCJ1539 and NGC1275 are exceptions with flows extending out to ∼21, 24 and 33 kpc, respectively. The average molecular flow size is ∼12 kpc in BCGs. AGNs span a broad range of flow sizes from 30 pc to 3 kpc. They are generally much smaller and more compact than those in BCGs with an average flow size of only ∼1 kpc. Molecular flow sizes in starburst and composite galaxies range between 100 pc and 1 kpc. Thus, the molecular flows in active galaxies studied by Fluetsch are generally confined to the nuclear regions. In contrast, the molecular flows in BCGs tend to be 10 to 1000 times larger extending well into the bulge and beyond.

2.5.3 Flow masses

Molecular gas masses in BCGs are calculated using the integrated intensity of the CO line emission. Flow masses were estimated from the CO intensity of spectra extracted from flow regions. The total molecular gas mass was estimated using the spectrum extracted from a region enclosing all detected CO emission. The molecular gas mass is inferred using an empirical expression calibrated for the CO(1-0) line. The integrated line flux ratios of $I_{\mathrm{CO(2-1)}}/I_{\mathrm{CO(1-0)}} \approx 3.2$ and $I_{\mathrm{CO(3-2)}}/I_{\mathrm{CO(1-0)}} \approx 7.2$ are used to convert integrated CO(2-1) and CO(3-2) flux densities to CO(1-0), respectively. The corresponding brightness temperature ratios are CO(2-1)/CO(1-0) = 0.8 and CO(3-2)/CO(1-0) = 0.8. These ratios are based on observed ratios at CO(3-2), CO(1-0) or CO(2-1) and CO(1-0) in BCGs (Russell et al., 2016; Vantyghem et al., 2016, 2017, 2018). They correspond to an excitation temperature of ∼20–25 K and high densities $\sim 10^4$ cm^{-3}. Integrated CO(1-0) flux is converted into molecular gas mass using the equation (Solomon & Vanden Bout, 2005; Bolatto et al., 2013)

$$M_{\mathrm{mol}} = 1.05 \times 10^4 \left(\frac{X_{\mathrm{CO}}}{X_{\mathrm{CO,Gal}}}\right)\left(\frac{1}{1+z}\right) \left(\frac{S_{\mathrm{CO}}\Delta v}{\mathrm{Jy\,km\,s^{-1}}}\right)\left(\frac{D_{\mathrm{L}}}{\mathrm{Mpc}}\right)^2 \mathrm{M}_\odot, \tag{2.1}$$

where $S_{\mathrm{CO}}\Delta v$ is the integrated flux density of the CO(1-0) line, D_{L} is the luminosity distance, z is the redshift of the galaxy and X_{CO} is the CO-to-H_2 conversion factor, with $X_{\mathrm{CO,Gal}} = 2{\times}10^{20}$ cm^{-2} (K km s^{-1})$^{-1}$.

The adopted value of X_{CO} lends to a factor of two or more uncertainty in the gas mass estimates. Its value depends on temperature, density and particularly, the metallicity of the molecular gas (Bolatto et al., 2013). Estimates of X_{CO} are available for Milky Way ($X_{\mathrm{CO,Gal}}$) and nearby galaxies. No direct estimate of X_{CO} is available for BCGs. However, studies have shown that the hot atmospheres surrounding BCGs, from which the molecular clouds have likely condensed, have metallicities lying between ∼0.6–0.8 $Z_\odot$, close to if not below solar metallicity. Furthermore, the line widths of individual molecular gas clouds are comparable to those in the Milky Way (Rose et al., 2019a; Tremblay et al., 2016; David et al., 2014; Heyer & Dame, 2015). CO line ratios are consistent with optically thick molecular gas (Russell et al., 2019). Vantyghem et al. (2017) found that the optically thin ^{13}CO to optically thick ^{12}CO line ratio in one BCG indicated abundances lying within a factor of two of the Galactic value. Therefore, we have adopted $X_{\mathrm{CO,Gal}}$ for BCGs in our calculations apart from Phoenix.

The BCG in the Phoenix cluster is undergoing star formation at a rate of ∼500 – 800 $M_\odot$ yr^{-1} (McDonald et al., 2012b) similar to LIRG/ULIRGs. It has been shown that the use of $X_{CO,Gal}$ in ULIRGs may overestimate the amount of molecular gas by a factor of five (Downes et al., 1993; Solomon et al., 1997; Downes & Solomon, 1998). Therefore, we have adopted $X_{CO} = 0.4{\times}10^{20}$ cm^{-2} (K km $s^{-1})^{-1}$ for Phoenix following Russell et al. (2017a). Fluetsch et al. (2019) use $X_{CO,Gal}$ in their calculations for all galaxies except for LIRGs and ULIRGs for which they use X_{CO} of $0.4{\times}10^{20}$ cm^{-2} (K km $s^{-1})^{-1}$ and $0.6{\times}10^{20}$ cm^{-2} (K km $s^{-1})^{-1}$, respectively, which is in agreement with the factor we assume.

Radio interferometers such as ALMA can underestimate the total flux if the angular size of the emission region is larger than the maximum recoverable scale given by $\sim 0.6\lambda/D_{min}$, where λ is the wavelength of the observation and D_{min} is the shortest baseline. Single dish telescopes generally do not suffer from this problem due to their large maximum recoverable scales. Therefore, we compared our molecular gas mass measurements with molecular gas masses obtained from single-dish observations (Edge, 2001) using the same CO-to-H_2 conversion factor as ours to quantify the missing flux in our observations. The ALMA molecular gas masses are within a factor of the single-dish molecular gas mass measurements. ALMA detected 60 percent more molecular gas in RXCJ0821, while in A1664, A1835 and NGC5044 the ALMA masses lie 25 to 40 percent below the single dish mass measurements. In the latter systems, ALMA may have resolved away some extended molecular gas. These discrepancies do not qualitatively affect our results.

Figure 2.4 shows the molecular gas mass associated with the out(in)flows on a logarithmic scale. BCG molecular flow masses lie between 0.3–12 $\times 10^9$ $M_\odot$ apart from the much smaller masses in NGC 5044 and Centaurus of $10^{7.7}$ $M_\odot$ and $10^{7.5}$ $M_\odot$, respectively. BCG flow masses differ markedly from those in Fluetsch et al. (2019). BCGs possess on average ∼100 times more molecular gas in flows compared to composites ($10^{7.5}$–$10^{8.5}$ $M_\odot$) and starburst galaxies (10^6–10^8 $M_\odot$). On the other hand, a broad mass range is found in AGN galaxies, lying between 10^6–10^9 $M_\odot$. Nevertheless, the most massive flows in BCGs exceed those in AGN by more than a factor of 10.

However, the total molecular gas masses in BCGs are comparable to those in (Fluetsch et al., 2019) (Fig 2.5). By comparison, the average total molecular gas mass in BCGs is $\sim 10^{10}$ $M_\odot$, while it is $5{\times}10^9$ $M_\odot$ in AGN and $3{\times}10^9$ $M_\odot$ in composite and starburst galaxies.

About half of the total molecular gas mass in BCGs is found in filaments. Some BCGs like Perseus are filament-dominated, in which almost all of the molecular gas is in filaments. In AGN-hosting galaxies the amount of molecular gas in the outflow is only ∼10 percent. It is even lower in composite and starburst galaxies at ∼3 percent.

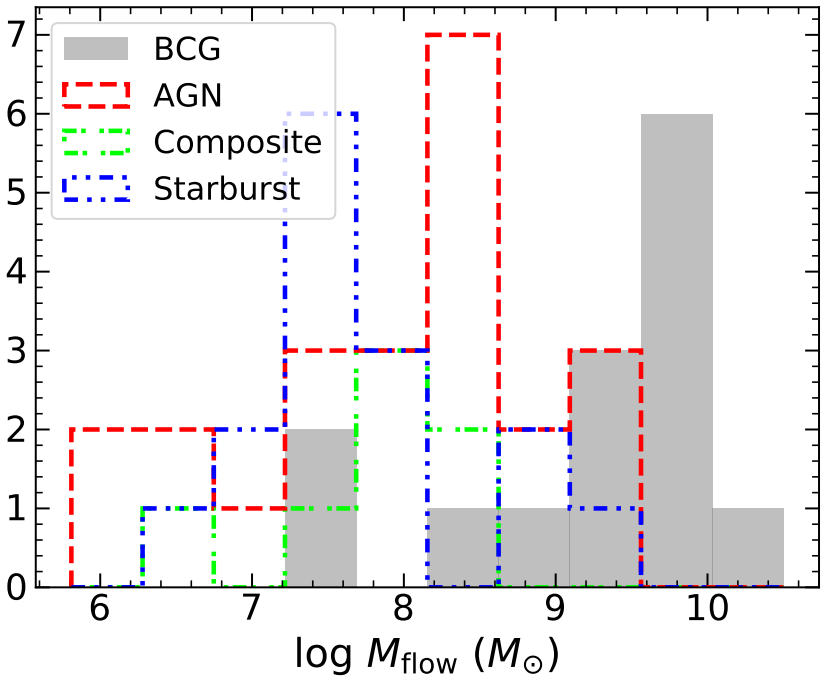

Figure 2.4: Histogram of the mass of molecular gas in outflows of BCGs, AGNs, composites and starburst galaxies.

On a cautionary note, many BCGs analyzed here were selected for observation based on their high molecular gas masses during the early ALMA cycles. Therefore they do not represent the molecular gas masses of average BCGs. We have kept this in mind as we draw scientific inferences from the data.

2.5.4 Measurement uncertainties

The true sizes of molecular flows and their velocities are systematically underestimated due to projection. Furthermore, when observed in emission we do not know what side of the nucleus the filaments are located. Unless absorption against the continuum is observed, it is very difficult to determine whether the gas is moving towards or away from the AGN (Rose et al., 2019a). Therefore, whether the filaments in an individual object are flowing in or out is unknown. Both inflows and outflows can be present at the same time. Observed velocities will be lower if both inflowing and outflowing gas is present along the line of sight.

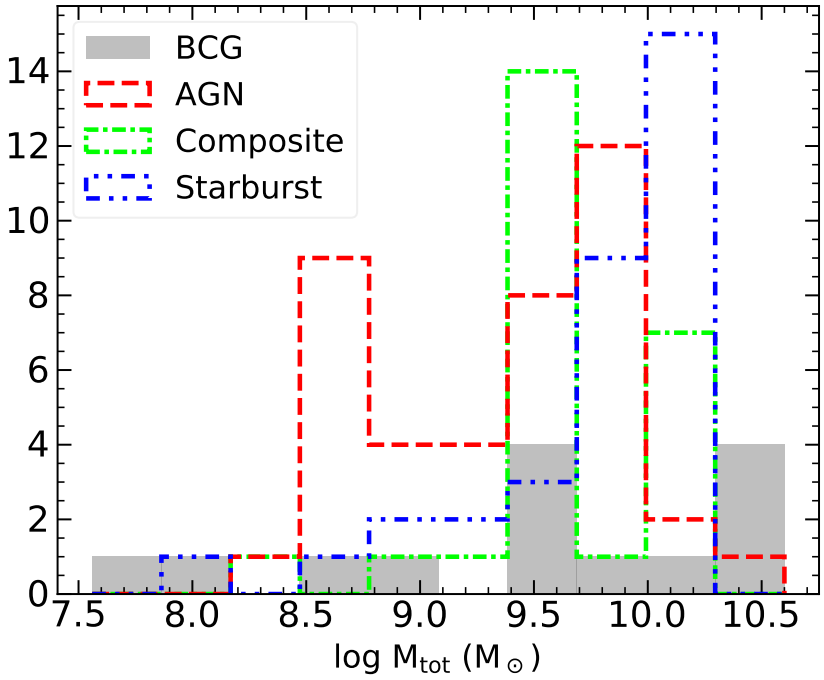

Figure 2.5: Histogram of total molecular gas mass in BCGs, AGNs, composites and starburst galaxies.

For example, in PKS0745, flux weighted average velocity is only 50 km s^{-1}, however, there is a component at $\sim$200 km s^{-1} in the extended filament. The low-velocity gas could have detached from the flow and slowed down or infalling onto the central galaxy. These effects would introduce a factor of a few uncertainty in velocity in most objects. Although these effects are difficult to quantify, we adopt 0.3 dex uncertainty in velocity.

The primary mass uncertainty comes from the application of $X_{\rm CO}$, which contributes 0.3 dex (Bolatto et al., 2013). Statistical uncertainties due to the fitting the total intensities add about $\lesssim$20 percent. Thus the average error on the mass of the outflow may be as large as 0.31 dex. Orientation and projection introduce scatter in both velocity and radius measurements. Including this scatter, the overall average error on flow properties is $\sim$0.5 dex.

2.6 Energy, Momentum, AGN radiation

AGN release mechanical energy and radiation capable of displacing the gas around them. In ULIRGs and quasars, AGN power is correlated with the kinetic power of the flows (Cicone et al., 2014), consistent with the AGN's energetic output driving the flows. The output is in the form of fast nuclear winds and radiation, and radiation pressure from young stars. In this section, we compare molecular flow energy and momentum fluxes in BCGs to the radiative energy and momentum fluxes of their AGN. We then compare those relations with AGN, composite and starburst galaxies to study the difference between these systems.

2.6.1 Flow momentum flux vs $L_{\rm AGN}/c$

Apart from a few known quasars hosted in BCGs with radio bubbles, the mechanical AGN power dominates the power budget usually by an order of magnitude or more (Russell et al., 2013). Nevertheless, some systems with powerful radio activity also emit nuclear X-rays. For the sake of completeness, we compare the nuclear radiation emerging from BCGs to that of the active galaxies in Fleutsch.

Here, $L_{\rm AGN}$ denotes the total isotropic radiated power emerging from the BCG's nucleus. Russell et al. (2013) estimated the nuclear X-ray luminosities ($L_{\rm nuc}$) in the $2-10$ keV energy range using photometric and spectroscopic methods. For those systems, we adopted their photometric value for $L_{\rm nuc}$. For the remaining sources (Phoenix and RXCJ0821), we

BCG	z	log $M_{\rm flow}$ ($M_\odot$)	log $M_{\rm tot}$ ($M_\odot$)	$R_{\rm flow}$ (kpc)	$v_{\rm flow}$ (km s^{-1})	$\dot{M}_{\rm flow}$ ($M_\odot$ yr^{-1})	log $P_{\rm Mech}$ (erg s^{-1})	log $L_{\rm Nuc}$ (erg s^{-1})	SFR ($M_\odot$ yr^{-1})	log ($M_\star$) ($M_\odot$)	Ref.
(1)	(2)	(3)	(4)	(5)	(6)	(7)	(8)	(9)	(10)	(11)	(12)
2A0335+096	0.0346	8.31	8.59	2	153	17	43.949	< 40.80	0.47	11.73	[a]
Abell 1664	0.128	9.56	9.87	6.3	579	341	44.04	< 41.50	13.18	11.1	[b]
Abell 1795	0.063	9.36	9.52	8.3	191	54	43.133	< 41.24	3.47	11.84	[c]
Abell 1835	0.252	10	10.6	12	61	52	45	< 42.78	117.49	10.57	[d]
Abell 2597	0.0821	10	10.3	15	61	42	44.278	< 41.73	3.98	11.51	[e]
PKS0745-191	0.1028	9.7	9.89	4.1	50	63	45.7	42.11	13.49	11.71	[f]
Phoenix	0.596	10.5	11.1	21.4	332	501	45.85	44.37	616.6	12.48	[g]
RXCJ1504	0.216902	9.7	10.4	18	108	30	44.96	42.66	85.11	11.7	[h]
RXCJ0821	0.109	10.21	10.32	4	28	72	44.4	< 41.14	37	11.06	[i]
NGC5044	0.00928	7.4	7.56	2.8	167	2	42.78	39.70	0.22	11.38	[j]
NGC4696	0.00987	7.52	7.95	4	222	2	43.11	< 39.67	0.16	11.79	[k]
RXCJ1539	0.075766	9.51	10.11	23	203	29	42.76		1.86	11.36	[k]
Abell S1101	0.05639	9.03	9.06	8.3	160	21	44.89	< 40.99	1		[k]
NGC1275	0.01756	9.02	9.68	33.3	117	17	43.9	42.71	70.79	11.38	[l,m]

Table 2.1: Properties of BCGs in the sample. **Columns:** (1) BCG name, (2) redshift, (3) mass of the flow, (4) total molecular gas mass, (5) radius of the flow, (6) speed of the flow, (7) flow rate, (8) mechanical power of the AGN, (9) nuclear 2-10 keV luminosity, (10) star formation rate, (11) stellar masses estimated from 2MASS K-band mangitudes following Main et al. (2017), (12) references: [a] Vantyghem et al. (2016); [b] Russell et al. (2014); [c] Russell et al. (2017b); [d] McNamara et al. (2014); [e] Tremblay et al. (2016); [f] Russell et al. (2016); [g] Russell et al. (2017a); [h] Vantyghem et al. (2018); [i] Vantyghem et al. (2017); [j] David et al. (2014); [k] Olivares et al. (2019); [l] Salomé et al. (2011); [m] Lim et al. (2008).

used archival *Chandra* observations to estimate nuclear luminosity/upper limits using Russell's photometric method. The presence or absence of a nuclear point source was verified by generating an image in the 3–7 keV band and visually inspecting for a central point source. When absent, upper limits for nuclear luminosities are presented. $L_{\rm nuc}$ was converted to total bolometric AGN radiative luminosity ($L_{\rm AGN}$) by multiplying it by a bolometric correction. For Compton thick AGN, the bolometric correction is $\kappa_{bol} \sim 30$, with an intrinsic uncertainty of 0.2 dex (Brightman et al., 2017). Our targets are likely Compton thin, so we expect the bolometric correction to be smaller than the one for Compton thick AGN. Low luminosity type-2 AGN have X-ray bolometric correction factors of ∼10 (Lusso et al., 2012). Therefore, we adopt $\kappa = 10$ for our calculations. AGN X-ray luminosity is sensitive to short-term AGN variability and can be underestimated.

The flow momentum flux is calculated as $\dot{M}v$, where $\dot{M}$ is the mass flow rate in gm s^{-1} and v is the flow speed in cm s^{-1}. $\dot{M}$ is estimated by dividing the mass of the flow by the time it takes the flow to reach its projected size (R/v). The rate of momentum output in radiation from the AGN is $L_{\rm AGN}/c$.

In figure 2.6, the flow momentum flux is plotted against radiative momentum flux $L_{\rm AGN}/c$. The diagram is intended to probe the ability of radiation emitted by the nucleus to drive a flow. Indicated in the figure are flow to AGN radiation momentum flux ratios $\dot{M}v/(L_{\rm AGN}/c) = 1, 5, 20$. According to nuclear wind-driven models, systems in which the ratio lies between 1 and 5 are able to be driven by radiation. Higher values of momentum flux ratios can be obtained by radiation driven flows when the gas in the central regions has high IR optical depth, as in highly obscured AGNs and ULIRGs. However, at kpc scales, the optical depth of the medium is generally too low for outflows to attain momentum flux ratios greater than 5. The energy conserving flows generally have momentum flux ratios above 5. All points lie above the one-to-one line, indicating that radiation is generally unable to drive the flows in these systems. These quantities are correlated in AGN and composite galaxies with a Pearson-r correlation coefficient of 0.73 at greater than 99 percent significance, including systems with either $L_{\rm AGN}$ or $\dot{M}$ upper limits. This indicates that even if AGN radiation pressure is unable to power a flow on its own, it may contribute significantly in high power AGN (Fluetsch et al., 2019).

As expected, BCGs show no correlation between the flow momentum flux and the AGN radiative momentum flux (Pearson r-value of 0.24, the 50 percent confidence level). This lack of correlation suggests that radiation pressure has little influence on flows in BCGs.

The momentum ratios for AGN and composite galaxies lie in the range predicted by nuclear wind-driven outflow models discussed in section 2.8. Still, the large scatter in the relationship makes it difficult to determine whether flows in these systems are energy con-

serving, momentum conserving, or a combination of both. In BCGs, the rate of change of flow momentum exceeds the radiative momentum input by ≥ 20, more than the maximum theoretical prediction for energy conserving flows. The only exception is Phoenix, which has a ratio of $\sim$0.2. Phoenix is the most powerful and highly star-forming BCG. It has an active AGN depositing a large amount of energy into its surrounding medium in both mechanical and radiative form in nearly equal amounts. That is reflected in the plot above, where the nuclear luminosity of Phoenix is $\sim 10^{46}$ erg s^{-1}, similar to quasars. Phoenix also has a high star formation rate (McDonald et al., 2019). Therefore, the conditions in the Phoenix BCG are similar to those in ULIRGs and quasars. Therefore, Phoenix is expected to be like ULIRGs, with a radiation pressure driven, momentum conserving flow. However, the molecular gas in Phoenix is closely tied to its radio bubbles, rather than star formation or the quasar. The bubbles are apparently doing most if not all of the work.

2.6.2 Momentum

Momentum may be conserved in some gas flows. After the hot shocked gas radiates away most of the kinetic energy, its momentum is left behind and drives the flow. As discussed in sections 2.5.3 and 2.5.1, flow speeds in BCGs on average are similar to flow speeds in star-forming galaxies and lower than AGNs. However, higher molecular gas masses are often found in BCGs. Therefore, their flow momenta are higher on average compared to AGN, composite or starburst galaxies (see figure 2.7). A broad range of flow momenta are found in AGNs, lying between 10^{46}–10^{50} g cm s^{-1}. The flow momenta in BCGs lies between 10^{49}–10^{50} g cm s^{-1} with an average of 2.3×10^{50} g cm s^{-1}. This figure is five to ten times larger than in AGN, composite and starburst galaxies whose average flow momenta are 6.6×10^{49}, 1×10^{49} and 1.7×10^{49} g cm s^{-1}, respectively. A small fraction of AGN galaxies also have a high flow momentum.

2.7 Gas Flows and Mechanical Power

BCGs often host powerful radio/mechanical AGN. The mechanical power output of the AGN is estimated as the power required to inflate the buoyantly rising bubbles of relativistic plasma that are fed through jets from the vicinity of the central SMBH (McNamara & Nulsen, 2007). These bubbles are observed as cavities in X-ray images. X-ray cavities are detected in all sources in our sample. The energy required to inflate a bubble is given by $E = 4PV$, where P and V are the pressure and volume of the bubble, respectively, where the bubble is approximately in pressure equilibrium with the surrounding ICM (Churazov

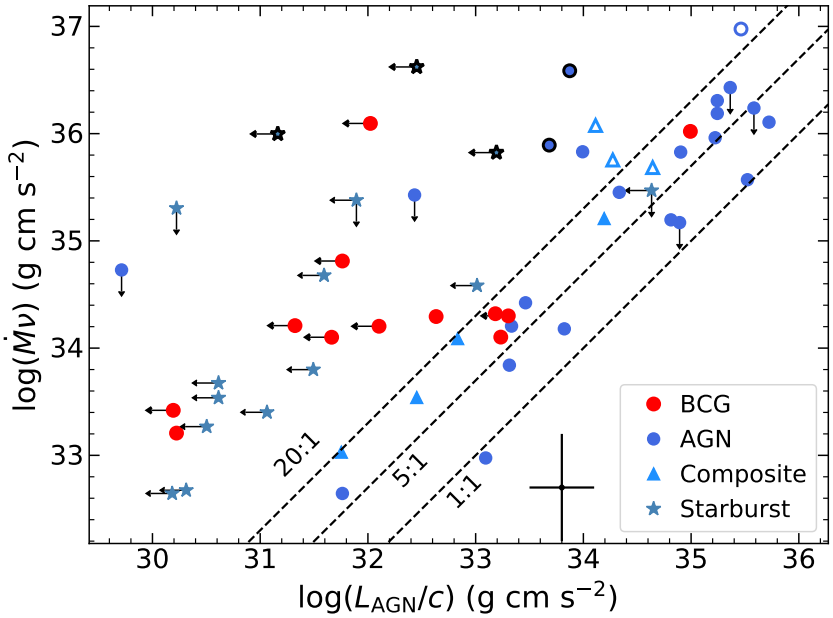

Figure 2.6: Relationship between the flow momentum rate and the AGN radiation momentum rate. The three dashed lines represent nuclear wind-driven model predictions for energy conserving (20:1), momentum conserving (1:1), and radiation pressure-driven (5:1) flows, respectively. Red circles are denoted by BCGs, AGNs by blue circles, composites by light blue triangles and star-forming galaxies by blue stars. Symbols with white circles in the middle are galaxies with flows detected in OH and symbols with black marker edges are fossil flows from the Fluetsch sample, respectively. The black point with error bars in the bottom right corner represents the average error bar on each point.

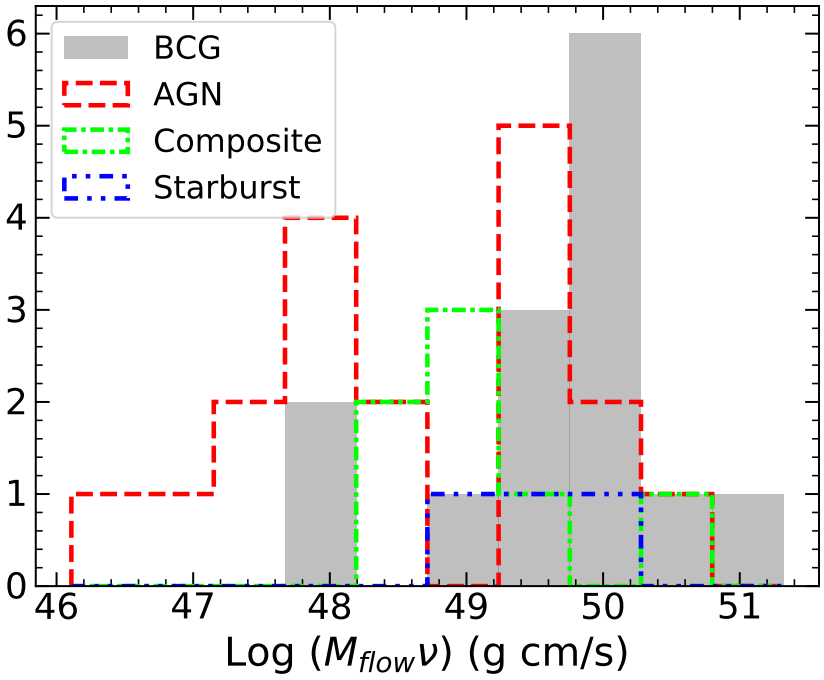

Figure 2.7: The histogram of flow momenta ($M_{\rm flow}\,\langle v_{\rm flow}\rangle$) in BCGs, AGN, composite and starburst galaxies.

et al., 2000). The mechanical power of the AGN ($L_{\rm mech}$) can be obtained by dividing the energy by the buoyancy time of the bubble. Cavity power measurements were taken from the literature (Bîrzan et al., 2012; Hlavacek-Larrondo et al., 2015; McDonald et al., 2015; Vantyghem et al., 2018; Calzadilla et al., 2019).

Their mechanical powers lie between $\sim 10^{43}$–10^{46} erg s^{-1}, one to two orders of magnitude larger than their nuclear radiation powers. Their mechanical powers are comparable to the radiative powers of AGN and some composite galaxies. Using the mechanical powers as $P_{\rm drive}$ for BCGs in the relationship between $P_{\rm drive}$ and $\dot{M}$ using linear regression gives a slope and intercept of 0.42±0.25 and 0.97±0.40 $M_{\odot}$, respectively. It is shown in Fig. 2.8 by a dotted line. The Pearson correlation coefficient 0.61 with a p-value of 0.02 indicates, again, a weak correlation. Thus, despite being comparable to the radiative powers of AGN and composite galaxies, mechanical powers are poorly correlated with the molecular gas flow rate.

This poor correlation is true for all systems including those in Fluetsch. While trends are seen and AGN have ample power to drive the flows, the process is complex and inefficient, with most AGN power either radiated away or being deposited in other forms.

The ample mechanical powers and close association of molecular gas filaments with X-ray cavities in several systems suggest molecular clouds are lifted by the rising bubbles or are condensing in their updrafts. Whether this is true in all systems is not clear. Evidence suggests that at least some molecular gas condenses from cooling hot gas lifted behind the X-ray cavities. Filaments may grow due to interpenetration of hot and cold gas (Liu et al., 2019). Extended molecular filaments are detected towards multiple generations of cavities in the Perseus cluster (Salomé et al., 2006). However, in some instances, the mass of molecular gas is close to and may exceed the displaced atmospheric gas mass, which would be difficult to explain by uplift unless the molecular gas was created by multiple AGN cycles (Russell et al., 2019). The scatter in the trend between the molecular filament mass and the mechanical power indicates a complex relationship between molecular gas and the AGN. This is true for the systems in Fluetsch, which also exhibit large scatter in their trends.

2.8 Lifting mechanism

The relationship between the kinetic energy flux of the gas flow and the lifting force provides a measure of the coupling between the power source and the gas. It is an easily-determined quantity in real and model systems and thus places interesting constraints. We define the

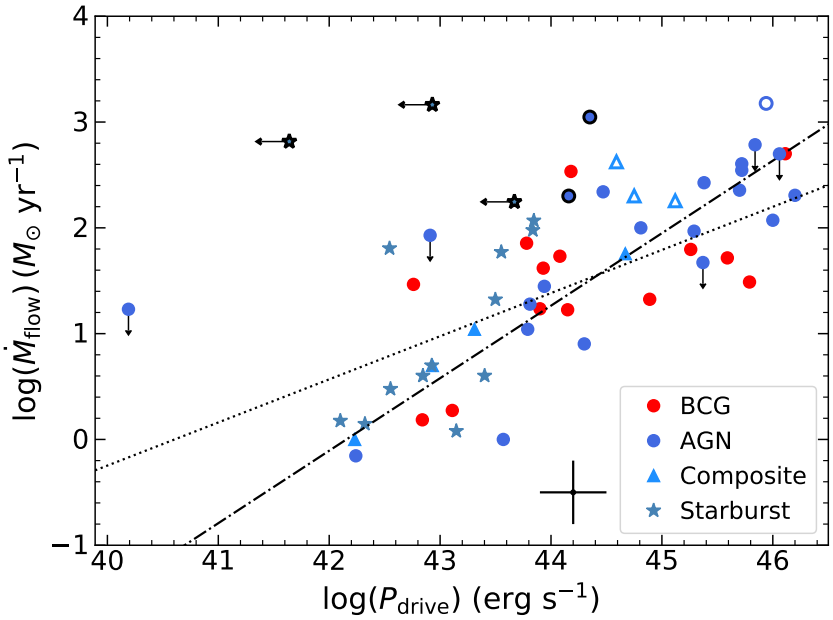

Figure 2.8: The power of the driving mechanism is plotted against the molecular flow rate. The red symbols indicate BCGs. For starburst galaxies, their star formation power is used as $P_{\rm drive}$. Dark blue circles, light blue triangles and murky blue stars represent AGN, composite and starburst galaxies from Fluetsch et al. (2019), respectively. The white filled symbols are flows detected in OH, and fossil flows are denoted by symbols with a black border. The dashed and dotted lines are the best fit lines for BCGs and Fluetsch galaxies, respectively.

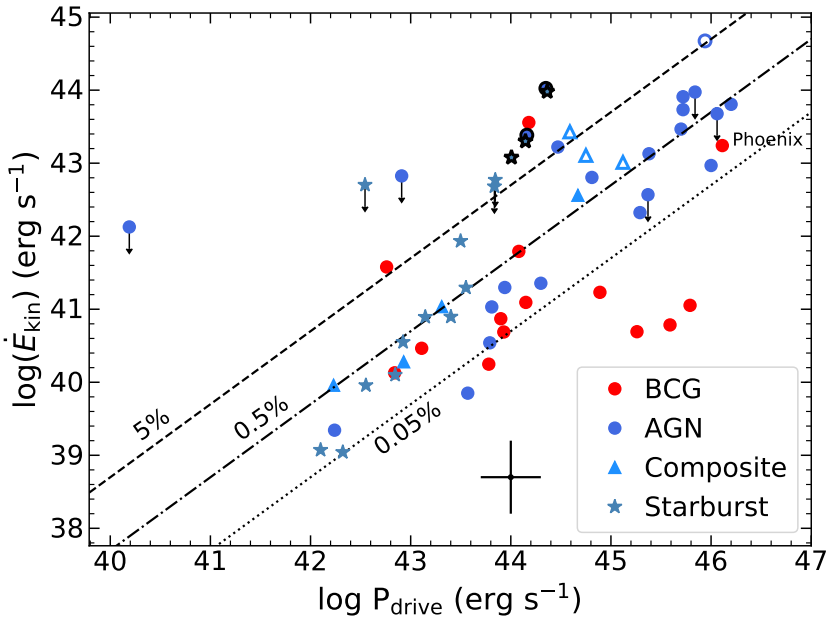

Figure 2.9: The figure shows the relationship between the kinetic power of flows and the mechanical powers in BCGs. For the Fluetsch galaxies, the x-axis represents the bolometric AGN luminosity. The black lines represent flow powers 5 percent (dashed), 0.5 percent (dashed-dotted) and 0.05 percent (dotted) that of bolometric AGN luminosity. Symbols are as in figure 2.8.

molecular flow kinetic energy flux as $0.5\dot{M}v^2$, where $\dot{M}$ is the mass flow rate and v is the average speed of the flow. The power for the Phoenix cluster BCG is indicated by the sum of its nuclear radiation and mechanical powers.

Figure 2.9 shows that the kinetic energy fluxes of molecular gas in most systems lie near or below a few percent of the AGN or starburst power. The radio/mechanically-driven BCGs are indistinguishable from the others in most BCGs, indicating that all mechanisms couple inefficiently to the molecular clouds and at similar levels. Some BCGs such as A1835, A2597 and PKS0745 lie much below others as a result of low flow speeds. The gas in these systems may have decoupled from the flow and slowing down. While a trend is observed in other systems, the scatter in kinetic energy flux at a given power spans 2-3 decades. Some scatter may be attributable to AGN variability. But the radio AGN show a similar scatter to nuclear AGN and starbursts. Mechanical power is averaged over $10^7 - 10^8$ yr, which is comparable to the timescales for accelerating the molecular clouds. Nuclear AGN vary on much shorter timescales. So the scatter is more indicative of both the weak coupling and the complex nature of feedback.

The three lines in Fig 2.9 were chosen to reference the fractions of AGN radiation power expected in energy conserving (5%), momentum conserving (0.5%), and radiation pressure driven (0.05%) flows. Most Seyfert and composite galaxies lie in the theoretically expected ranges. Thus, the coupling between AGN power and molecular flow kinetic energy in BCGs and other systems are broadly similar, despite very different acceleration mechanisms.

2.8.1 Lifting Factor

Molecular gas flows in BCGs generally have higher masses and extend to larger distances on average than the systems in Fluetsch et al. (2019). These properties indicate that radio AGN are generally more capable than nuclear winds, radiation, and starbursts at propelling molecular clouds out of the centers of galaxies, at least at the present epoch.

This phenomenon is explored further in Figure 2.10, where we compare the product of the mass and flow size per unit power. We refer to this as the lifting factor. The radio-mechanical power is adopted for BCGs. For AGN in the Fluetsch sample, we adopted the bolometric AGN luminosity. For starburst galaxies, we adopted the star formation power estimated from star formation rates using the relation $P_{\rm SFR}$ (erg s^{-1}) $= 2.5 \times 10^{41}$ SFR ($M_\odot$) from (Veilleux et al., 2005). This conversion factor is consistent with the factor measured independently in the central galaxy Abell 1835 (McNamara et al., 2006) which is included in our sample. This single example offers reassurance that the conversion relation of Veilleux et al. (2005) applies to BCGs.

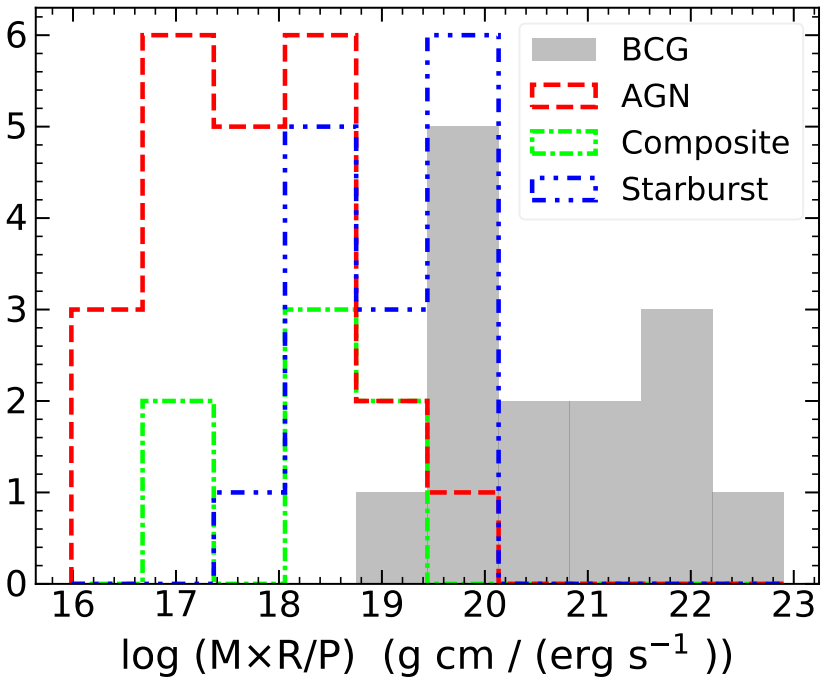

Figure 2.10: Histogram of flow distance times the flow mass divided by the power of the driving mechanism for BCGs, AGN, composite and starburst galaxies. This quantity is referred to as the lifting factor in the text.

Figure 2.10 shows BCGs have higher lifting factors on average than other outflow systems, indicating that radio-mechanical feedback is more effective per unit power at lifting large masses to greater distances than nuclear AGN and starbursts. The lifting factor for starbursts (H2 galaxies) is considerably larger than for AGNs. The starbursts overlap the lifting factors of the weakest BCG flows, but BCGs outperform all by more than an order of magnitude using this figure of merit.

Figure 2.10 can be interpreted in the context of Figure 2.9. In Figure 2.9 we show that the molecular kinetic energy fluxes against driving power are of similar magnitude between the BCGs and galaxies in the Fluetsch sample. At first blush, Figure 2.9 and Figure 2.10 appear to be inconsistent with each other. This apparent inconsistency is attributable to the large differences in the timescale and size of the flows. The AGN in Fluetsch are driving smaller masses of molecular gas over shorter distances but at higher speeds. The much larger masses, distances and timescales in BCGs compensate such that the kinetic energy fluxes per unit power are similar. However, the total mass displaced over time is much larger in BCGs for a given mean power.

The large range of lifting factors may be due to variations in flow characteristics including the volume affected by radio, nuclear, and star-formation activity and the ability of the working surfaces to couple to the ambient gas. This coupling is always weak but varies greatly (Fig. 2.9).

Radiation pressure wind energy is released on smaller scales close to the AGN, where radiation intensity is strong, and the particle number density is high. At larger distances the medium becomes tenuous, and the radiation intensity drops rapidly. The outflow then transitions into a momentum conserving flow and rapidly slows down (Veilleux et al., 2020). Therefore, radiation driven flows are less efficient at lifting a large amount of mass to vast distances.

The large lifting factor of radio-mechanical feedback in BCGs is attributable to the large volume of impact and the relatively long timescales radio bubbles are able to lift gas in the surrounding interstellar medium and atmosphere. Radio bubbles couple to the gas in the inner kpc (Mukherjee et al., 2018; Guo et al., 2018) lifting the low entropy gas in their wakes to high altitudes through drift and entrainment (Pope et al., 2010). This is observed in real systems as high metallicity atmospheric gas located in the wakes of rising X-ray bubbles extending in some instances to altitudes of tens of kpc (Kirkpatrick & McNamara, 2015).

Radio bubbles encompass a large range of sizes and volumes, with diameters of a few kpc to over 200 kpc. A typical bubble appearing as an X-ray cavity is elliptical in projection with an average semi-major and semi-minor axis of 11.4 kpc and 7.7 kpc, respectively

(Rafferty et al., 2006; Calzadilla et al., 2019; McDonald et al., 2015; Hlavacek-Larrondo et al., 2015; Vantyghem et al., 2017). Assuming an ellipsoidal 3D shape, the average volume of a bubble is 10^{68} cm^3. In contrast, the average volume of the AGN wind-driven outflows is $\sim 10^{65}$ cm^3, assuming cylindrical geometry with a radius and height of $\sim$1 kpc, respectively. Starbursts typically occur within the central 1 kpc. The energy injection region is typically up to $\sim$2 kpc in extreme situations, after which the flow starts slowing down (Schneider et al., 2020). Thus, the affected volume is approximately 16^{65}–10^{66} cm^{-3}. The volume would be smaller considering a more realistic bi-conical geometry. Therefore the working volume of radio-mechanical feedback is much larger and affects a much larger mass for a given ambient gas density.

Another key factor is the long lifting timescales of radio/X-ray bubbles. Their typical observed ages lie between 10–20 million years (Bîrzan et al., 2004). But many survive for $\sim$ 100 million years or longer (Brienza et al., 2021). While the jet launching phase typically lasts for $\sim$10 million years, comparable to a typical quasar lifetime (Martini & Schneider, 2003; Bird et al., 2008; Schawinski et al., 2015), radio bubbles propelled outward by buoyancy continue to draw in and lift gas in their updrafts. Therefore, a single radio event can continue to drive gas outward long after a quasar of similar power shuts down. Once it shuts down the gas slows down in the galaxy's gravitational potential and by ram pressure and drag forces.

We have considered here only the displaced molecular gas in BCGs. The effects shown in Figure 2.10 are likely larger. Rising radio bubbles also lift and displace hot gas from the central atmosphere. *Chandra* has observed metal enriched gas preferentially along the radio jet axes (Kirkpatrick et al., 2011; Simionescu et al., 2008; Gitti et al., 2011). Similar features are reproduced in hydrodynamic simulations indicating 10^9–10^{10} M$_\odot$ of metal rich gas lifted from central regions of galaxy clusters (Duan & Guo, 2018; Qiu et al., 2020; Li et al., 2015).

The atmospheric mass displaced by cavities is comparable to or larger than the molecular gas masses (Russell et al., 2019). Fluetsch et al. (2019) found the molecular masses in their sample exceeded the atomic and neutral phases by roughly 40 times. Therefore, in order to compare our systems with Fluetsch, we have not included the hot gas masses. But were we to do so the flow rates and masses would increase by a factor of two or more.

2.9 Star Formation

Here we explore relationships between feedback, outflows, and star formation. We adopt BCG star formation rates (SFR) from McDonald et al. (2018) who used several methods

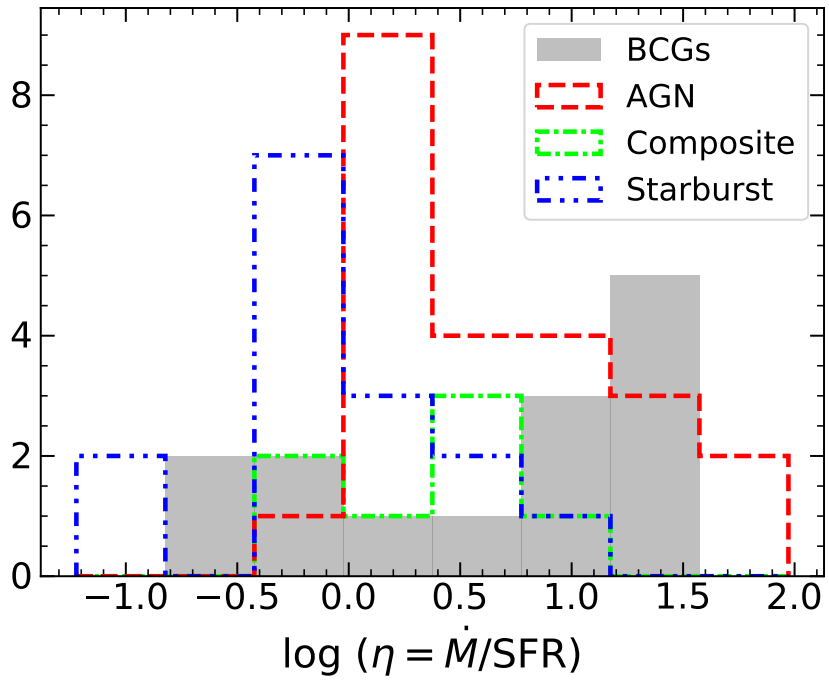

Figure 2.11: Histogram of log of the mass loading factor in BCGs, AGNs, composite and starburst galaxies.

to estimate the SFRs. For Pheonix, they decomposed the spectrum to separate the AGN component from stellar radiation. For the remaining objects, they adopted the logarithmic mean of multiple SFRs for each system found from the literature. The average logarithmic scatter in measurements of SFRs for BCGs is determined to be 0.28 dex. The SFR measurement for RXCJ0821 is taken from O'Dea et al. (2008).

2.9.1 Mass loading factor

The mass loading factor η is defined as the ratio of the molecular gas flow rate to the star formation rate ($\eta = \dot{M}/SFR$). A high value of η indicates that the AGN can sweep the gas from the galaxy as quickly as star formation consumes it. Low η indicates that star formation will consume a significant amount of gas before it can be removed from the inner regions of the galaxy. The histogram in figure 2.11 shows the distribution of η for different galaxy types, including the fossil galaxies in the Fluetsch sample. The majority of the star-forming galaxies have mass loading factors $\leq$1. This is expected from feedback models for star-forming galaxies in which supernova explosions are the primary outflow driving mechanism. The galaxies hosting AGN from the Fluetsch sample and BCGs have a broad range of η from 0.1 to $\sim$100. However, the majority of those galaxies have $\eta > 1$.

High values of η found preferentially in BCGs and AGN galaxies indicate that much gas is displaced from these systems before it can form stars. Therefore, star formation may be suppressed or quenched assuming the gas leaves the galaxy and does not return. In the next section, we show that very little molecular gas leaves these systems.

2.9.2 Does Radio-mode Feedback Suppress Star Formation?

The left panel of Fig. 2.12 shows the relationship between the total molecular gas mass and the star formation rate for BCGs and the Fluetsch galaxies. Two clear trends are seen in Figure 2.12. Linear regressions of the form log SFR ($M_\odot$ yr^{-1}) = a log $\frac{M_{\rm tot}}{10^9 M_\odot}$ + b were fitted separately to the data for the Fluetsch galaxies and BCGs. The values of parameters (a, b, Δa, Δb) for BCGs and Fluetsch galaxies are (1.13, 0.23, 0.26, 0.24) and (1.66, 0.67, 0.43, 0.23), respectively. Δa and Δb are the 1σ errors. The best fit-lines for BCGs and Fluetsch galaxies are shown by the dashed and dashed-dotted lines, respectively.

The values of the parameter a indicate the two populations have different slopes. BCGs have a lower total star formation rate per unit molecular gas mass compared to galaxies from the Fluetsch sample. The segregation becomes strikingly apparent for total molecular gas masses greater than $\sim 10^9$ $M_\odot$. To test the statistical significance of the difference

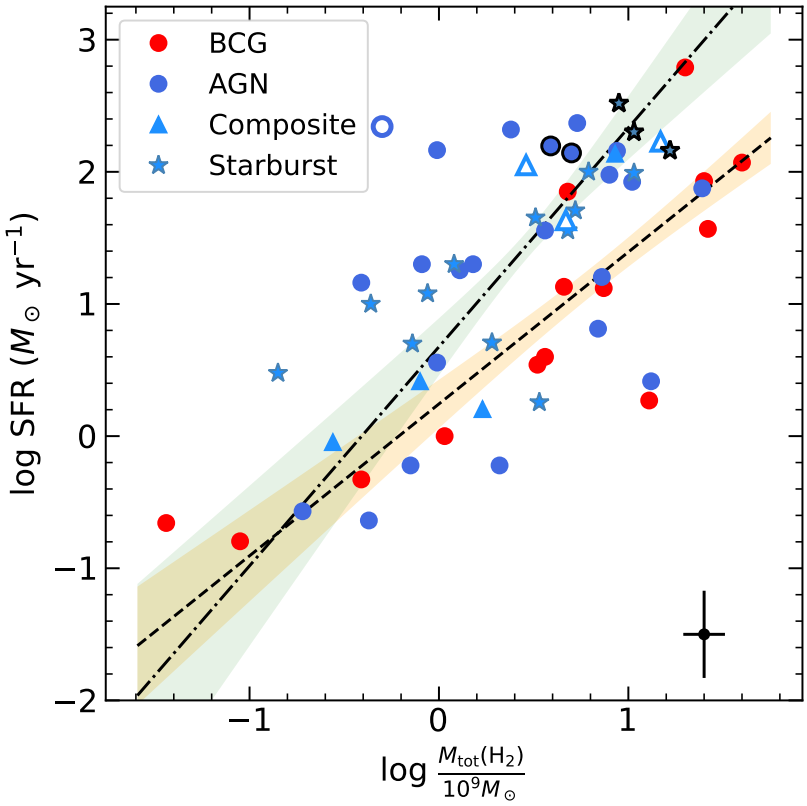

Figure 2.12: The left panel shows the total molecular gas mass plotted against the SFR of host galaxies. The dashed line and orange region show the best-fit line and 1σ confidence interval for BCGs, respectively. The dashed-dotted line and the green shaded region show the same for all Fluetsch galaxies. All symbols are as in figure 2.8.

observed between the two best-fit lines, we conducted a two-sample t-test with a null hypothesis that the coefficients of the two linear regressions are equal. The t-statistic for the slope is 5.6 with a p-value smaller than 0.005. Similarly, the t-statistic for the intercept is 5.5 with a p-value smaller than 0.005. Therefore, we can confidently reject the null hypothesis. The observed difference between BCGs and Fluetsch galaxies in the relationship between their SFR and $M_{\rm tot}$ in log space is statistically significant. Given the small sample size, we cannot determine whether the separate trends are due to selection bias.

The picture changes when atomic and molecular gas masses are considered together. The right panel of Fig. 2.12 shows the same relationship when both atomic and molecular gas components are taken into account for Fluetsch galaxies. In this analysis, we consider only molecular gas in the BCGs. Only upper limits for atomic gas masses for a small number of BCGs are available. Babyk et al. (2021) has shown that based on H I upper limits, the ratio of molecular to atomic gas mass in these systems lies well above unity. Therefore, we do not expect H I masses to substantially alter the location of the BCGs in these figures. This is not true for the Fluetsch systems.

H I gas masses are available for 18 Fluetsch galaxies. For the remaining galaxies, their H I gas mass was assumed equal to the average of the observed H I gas masses for galaxies in the Fluetsch sample. In all except for a few galaxies, the atomic gas mass exceeds the molecular gas mass. When both gas phases are considered together, Fluetsch galaxies contain $>10^9$ $M_\odot$ of gas, which is comparable to molecular gas masses in BCGs. However, no clear relationship is found between the total (H I+H_2) gas mass and SFR in Fluetsch galaxies.

To further investigate these potentially interesting trends, we compared the star formation in BCGs and galaxies from Fluetsch with the Kennicutt-Schmidt (KS) relation. KS relates the star formation rate surface density ($\Sigma_{\rm SFR}$) to the total (H I+H_2) cold gas surface density (Kennicutt, 1998). The KS relation is well-characterized, fits a broad range of galaxy classes, and scales non-linearly as $\Sigma_{\rm SFR} \propto \Sigma^{1.4}_{\rm HI+H_2}$.

We compared the SF law in BCGs and Fluetsch galaxies with the KS relation. We adopted star formation rates in BCGs listed in Table **??**, and the remaining star formation rates were taken from Fluetsch et al. (2019). In most Fluetsch galaxies, star formation occurs in the circumnuclear region within ∼1 kpc. Star formation rates in galactic disks typically lie between 1–20 $M_\odot$ yr^{-1} (Kennicutt, 1998). Therefore, we have adopted the area of a 1 kpc radius region around the nucleus to estimate gas and star formation surface densities for Fluetsch galaxies with star formation rates greater than 20 $M_\odot$ yr^{-1}. For the remaining galaxies from the Fluetsch sample, we obtained their angular diameters

from NED[3]. We used blue band diameters from the RC3 - Third Reference Catalog of Bright Galaxies (Corwin et al., 1994) and estimated areas assuming elliptical shapes. In eight BCGs, the areas of the star formation regions were estimated using UV-band images from the Hubble Telescope. The star formation regions in these BCGs are confined within roughly 3 kpc to 10 kpc of the center. Star formation in Phoenix and Perseus extend up to ∼25 kpc in filamentary structures. For the remaining BCGs, we adopted a conservative area of the inner 3 kpc region centered on the nucleus. In some BCGs (e.g., Abell S1101, RXCJ1539.5, PKS0745), molecular gas is more extended than the star forming region. Therefore, the molecular gas surface densities may be overestimated by a factor of ∼2 in these systems.

Figure 2.13 shows the star formation law in BCGs and Fluetsch galaxies when only molecular gas surface density is used for all galaxies. The best-fit relation for all galaxies is given by:

$$\Sigma_{\rm SFR} = 10^{-3.09\pm0.49}\Sigma_{\rm H_2}^{1.34\pm0.17}, \tag{2.2}$$

where, $\Sigma_{\rm SFR}$ is in $M_\odot$ yr^{-1} kpc^{-2} and $\Sigma_{\rm H_2}$ is molecular gas surface density in $M_\odot$ pc^{-2}. The overall distribution appears consistent with the KS relationship. The dispersion around the KS relation is larger than the observational uncertainties alone, implying real variance from galaxy to galaxy. Some of this variance may be attributed to variations in the $X_{\rm CO}$ factor used to convert CO surface brightness to molecular gas mass (see Kennicutt & Evans, 2012, for review, and references therein). Most BCGs fall into the intermediate density star formation regime occupied by normal spiral disk galaxies and the inner regions of the Milky Way. The star formation surface densities of most Fluetsch galaxies are higher than the BCGs and are typical of those observed in circumnuclear starbursts and ULIRGs. This is to be expected as the Fluetsch sample contains several ULIRG and starburst systems.

The Fluetsch galaxies lie systematically above the KS relation, such that they have higher than normal star-formation-rate surface densities compared to their molecular gas mass surface densities. Whether this departure is real or due to measurement bias is unclear. The KS relation is properly characterized as the sum of the atomic and molecular gas surface densities. We consider here only the molecular gas mass because H I emission is rarely observed in BCGs, whose cold gas reservoirs are likely dominated by molecular gas with H_2/H I ratio unity or above (Babyk et al., 2021).

Why BCGs have lower star formation rates per molecular gas mass compared to the Fluetsch galaxies is unclear. The location of the Fluetsch galaxies above the KS law while the BCGs follow the law suggests the Fluetsch galaxies have higher than normal star formation rate densities. The BCGs are outwardly normal. This difference may be

[3] https://ned.ipac.caltech.edu/

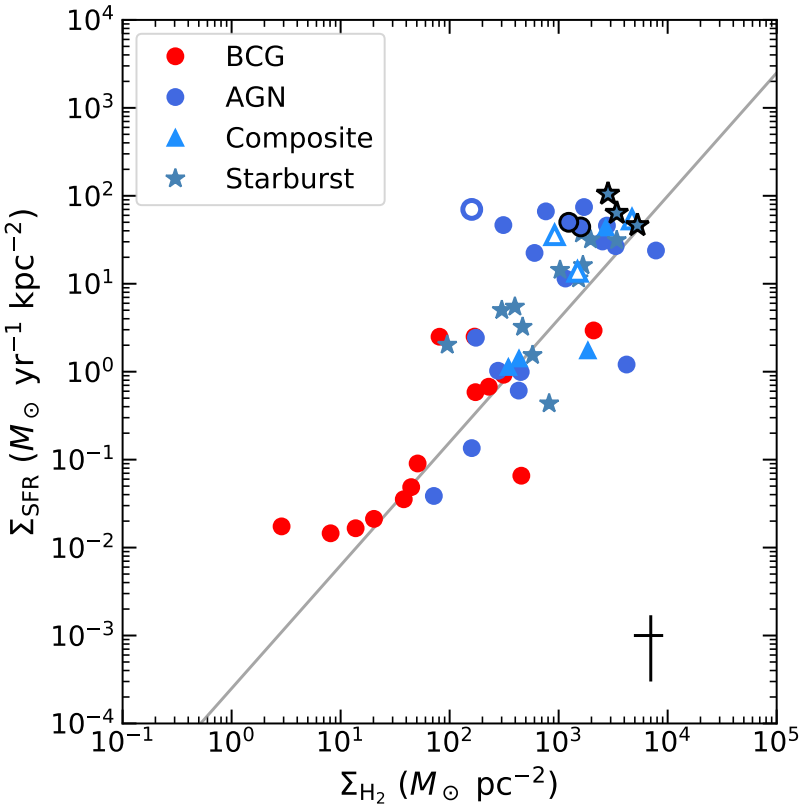

Figure 2.13: The figure expresses the relationship between the molecular gas surface density and the SFR surface density for BCGs and FL galaxies. The grey line shows the global Kennicutt-Schmidt relation (Kennicutt, 1998). Symbols are as in figure 2.8.

related to the fact that half of the total molecular gas in BCGs is found in off-nuclear filaments and is rarely seen in circumnuclear disks (Russell et al., 2019; Olivares et al., 2019). The filaments, being dynamically disordered and perhaps younger than disk gas, may be less prone to gravitational instabilities leading to star formation. The magnetic field may further reduce fragmentation. Mixing with hot surrounding gas and magnetic reconnection may reheat the cold filaments before star formation can ensue (Fabian et al., 2011; Churazov et al., 2013). The gas in the nuclear regions is also dynamically disturbed in many BCGs. The lack of ordered structure in the nucleus suggests that the gas is dynamically young or is continually destroyed and reformed within the central galaxy, preventing it from being consumed by star formation on short timescales. Perhaps one or more of these factors reduces the efficiency of star formation per unit local free-fall time in BCGs compared to AGN, composite and starburst galaxies. These suggestions are speculative and merit rigorous treatment in the future.

2.10 Fate of the Outflowing Gas

The final disposition of the outflowing gas depends on many factors including, the loading factor, the speed of the flow relative to the escape speed, and the rates of formation and destruction of molecular clouds. Figure 2.11 indicates broad similarity across all feedback modes in nearby AGN, albeit with a large scatter. Loading factors near and above unity indicate that winds are as effective or more effective than star formation at depleting the gas supply.

The degree to which star formation is delayed or suppressed depends largely on whether the molecular gas escapes the galaxy. Fluetsch found that in systems with the highest outflow speeds, only a few percent of the molecular gas escapes entirely. In most instances escape is negligible. If the currently outflowing gas returns to the galaxy in molecular form, it would be available for future star formation. This scenario is almost certainly true in BCGs, where molecular gas velocities are low compared to both the free-fall speeds and escape speeds (Russell et al., 2017a,b, 2019). This is compounded by ram pressure forces on the gas by the surrounding hot atmosphere. The emerging picture is a fountain where hot and possibly cold molecular gas is lifted behind the bubbles. The gas eventually cools. Most will likely return to the galaxy, but some molecular gas may be destroyed. The details are unclear.

To compare the molecular gas speeds to the escape speeds, we adopt the Hernquist profile to model a galaxy's gravitational potential. The estimated escape velocities are

found using the following formula:

$$v_{\rm esc} = \sqrt{\frac{2GM}{r+a}} \tag{2.3}$$

where a is the scale radius, which is related to the effective radius as $R_e \sim 1.8153a$, and M is the stellar mass of the galaxy taken from table **??**. To obtain an approximation to the escape velocity for the Phoenix cluster BCG, we adopt the value 17 kpc from McDonald et al. (2012b). For the remaining galaxies, we use an empirical relation between effective radius and stellar mass for local elliptical galaxies from McIntosh et al. (2005) to determine R_e. This method overestimates the effective radius for Phoenix by ∼65 percent. Therefore, we adjusted effective radii to take this factor into account. The escaped gas was defined as the molecular gas with a velocity greater than the escape velocity of the galaxy. To estimate the escaped gas fraction, we integrated the spectrum above the positive and below negative escape velocity and compared it to the total integrated intensity of the flow.

We found that for all BCGs the escaped gas fraction is negligible. The high-velocity gas in Abell 1664 has sufficient velocity to escape the central region of the BCG. But it lies well below the escape velocity of the central cluster halo and will likely return.

As the gas cannot leave the galaxy, it will likely return. Thus some of the molecular gas in BCGs is almost certainly flowing inward. As discussed in section 2.5.2, it is extremely difficult to distinguish an outflow from an inflow with gas seen in emission. However, molecular gas is seen in absorption against the nuclear continuum of some systems (David et al., 2014; Tremblay et al., 2016) has revealed both in- and out-bound molecular gas with velocities between -45 km s^{-1} and 283 km s^{-1} (Rose et al., 2019a). The absorption velocities are broadly consistent with the molecular fountain model.

2.11 Concluding Remarks

We have shown that mechanical energy released by radio jets can have a far more dramatic impact on galaxies compared to nuclear radiation (QSOs) and winds in contemporary active galaxies. This is also true in ancient massive galaxies lying at high redshift. The relative impact of radio-mechanical feedback, characterized here as the lifting factor, is qualitatively similar to the situation in high redshift radio galaxies experiencing both quasar and radio-mechanical feedback. In a study of 24 radio galaxies lying at $z \sim 2$, (Nesvadba et al., 2017) examined the energy and momentum imparted on the surrounding ionized gas by star formation, radio jets, and nuclear AGN. They found that while starburst winds play a minor role, radio jets are generally more effective than quasars at powering gas motions.

Likewise, Kellermann et al. (2016) found that 20% of contemporary quasars lying between $z = 0.2 - 0.3$ are radio-loud, double-lobed systems, akin to those at higher redshift. Furthermore, (Jarvis et al., 2019) noted that compact radio jets with relatively modest radio luminosities hosted by some quasars lying within the Kellermann et al. (2016) redshift range are interacting with and driving outflows of nebular gas. Assuming radio jets are operational during 20% of the life of a quasar, as the Kellermann et al. (2016) results may imply, their large lifting factors indicate that radio-mechanical feedback would have a significant effect on the evolution of their host galaxies.

A difference between the Nesvadba study and ours apart from the epoch is the ability to examine the three forms of feedback occurring simultaneously in the same galaxies. While this approach is rarely possible in the contemporary Universe, some central cluster galaxies are simultaneously experiencing powerful nuclear AGN, starbursts, and radio-mechanical feedback. For example, IRAS 09104, is a radio galaxy with large X-ray cavities surrounding a quasar host lying at $z = 0.44$. Its quasar power exceeds its radio-mechanical cavity power by more than an order of magnitude. Yet its cavities are driving $\sim 4.5 \times 10^{10}$ $M_\odot$ of molecular gas out of the central galaxy with little help from the quasar (O'Sullivan et al., 2021). The same is true for the iconic Phoenix cluster central galaxy (Russell et al., 2017a) where radio-mechanical feedback is the primary source of energy and momentum input to its $\sim 10^{10}$ $M_\odot$ well of molecular gas. We now understand that this feedback mechanism has been operating effectively through much of the history of central cluster galaxies (Ma et al., 2013; Hlavacek-Larrondo et al., 2015) and a broader spectrum of massive galaxies (Nesvadba et al., 2017).

Powerful radio AGN are found commonly in massive giant ellipticals (Best et al., 2003, 2005; Heckman & Best, 2014) often hosting dense, high pressure atmospheres. Radio AGN are also found in giant ellipticals in less dense atmospheres capable of driving both HI and molecular flows (Morganti et al., 2005). In these systems the radio energy may be a significant fraction of the thermal energy in their atmospheres, indicating that the radio jets are heating the atmospheres and driving away hot gas from their elliptical galaxy hosts (Webster et al., 2021a; Morganti et al., 2021).

How far down the radio luminosity function radio-mode feedback is affecting galaxy evolution is unknown. Radio surveys such as NVSS and First detect primarily low radio luminosity galaxies (Tadhunter, 2016). But even low power radio galaxies trace much higher mechanical powers (Bîrzan et al., 2008; Croston et al., 2018) and presumably higher lifting factors. Recent observations suggest that the mechanical feedback could be significant in 10% of Seyfert galaxies (Webster et al., 2021b) whose hosts are spiral rather than elliptical galaxies. Even dwarf galaxies experience AGN feedback (Manzano-King et al., 2019), some driven by mechanically-powerful radio jets (Mezcua et al., 2019; Davis et al., 2022).

The upshot here is that when active, radio jets can strongly influence the evolution of galaxies from their nascency to mature contemporary galaxies. The systems studied here do not represent the general population of galaxies. Instead, they are snapshots of an active period through which most massive galaxies transit. It would be premature to draw broad conclusions about the influence of radio-mode feedback on the general population of galaxies and their nuclear black holes. This must await further investigations of large samples of galaxies observed across the electromagnetic spectrum from radio to X-rays.

2.12 Summary

Molecular gas properties are examined in 14 active galaxies (BCGs) centred in clusters with cooling atmospheres. The molecular gas properties and power output from AGN and star formation were compared to 45 local active galaxies compiled by Fluetsch et al. (2019). Our results are summarized as follows:

• BCGs centered in cooling atmospheres contain $\sim 10^8\ M_\odot$ to upwards of $10^{10}\ M_\odot$ of molecular gas. Thirty to seventy percent of the gas lies outside of the nucleus in extended, filamentary structures that appear to be moving relative to the BCG. Gravitationally stable structures, such as large-scale disks, are rare (Olivares et al., 2019; Russell et al., 2019). In contrast, only a few to ten percent of the total molecular gas mass in contemporary AGN and starburst galaxies examined by Fluetsch et al. (2019) is flowing inward or outward. The remainder presumably lies in disks or other stable structures.

• Molecular clouds surround or lie beneath X-ray cavities inflated by radio jets in many systems. The clear association of molecular clouds with X-ray cavities in systems such as the Perseus cluster (NGC 1275), the Phoenix cluster, Abell 1835 and others indicate that molecular clouds are being lifted outward, clearing the nucleus of gas. Molecular clouds may also be condensing from atmospheric gas lifted in the updrafts of the rising radio bubbles (cavities). The molecular mass lifted by radio bubbles can exceed the masses of gas flows studied by Fluetsch et al. (2019) by factors of 10–100.

• Radio bubbles are able to lift molecular material to altitudes of ~ 10 kpc and beyond, with flow sizes on average $\sim$10 times larger compared to active galaxies compiled in (Fluetsch et al., 2019). Cluster outflows tend toward lower velocities than those in the comparison sample. However, their momentum fluxes are, on average, an order of magnitude larger.

• We introduce the lifting factor, a parameter that is the product of the mass and size of the molecular flow divided by the driving power. The driving power is characterized by the measured AGN power or the starburst power. This parameter indicates that radio-mode feedback is vastly more capable of driving large gas masses to higher altitudes per unit of driving power than other active systems. This result is consistent with similar measurements for powerful radio galaxies at redshifts beyond 2 (Section 11).

• Loading factors vary broadly in BCGs from $\sim 0.1 - 100$. This range is similar to the active galaxies compiled by Fluetsch et al. (2019). Only a few percent at most of the AGN mechanical power in BCGs is transmitted to the molecular gas. This fraction is also similar to the systems in Fluetsch et al. (2019).

• The star formation rate per gram of molecular gas in BCGs is five to ten times lower than the most massive systems with AGNs and starbursts studied by Fluetsch et al. (2019). As molecular gas is closely associated with star formation, this deficit indicates, tentatively, that star formation in BCGs is suppressed compared to other systems.

• Molecular cloud velocities in BCGs lie well below escape speeds. Similar to the systems in Fluetsch et al. (2019), little or no molecular gas is able to escape the galaxy. Radio-mechanical feedback is likely driving a fountain of hot and cold gas that eventually returns to the central galaxy. This process may delay or suppresses star formation relative to other active galaxies.

Radio-mechanical feedback (radio-mode) is more complex than is commonly assumed. Radio sources not only heat their surrounding atmospheres but also drive molecular clouds out of their host galaxies. In some instances, radio-mode feedback may promote the condensation of molecular clouds from their hot atmospheres that would sustain long-term feedback needed to prevent the outsized growth of galaxies. Radio lobes are more capable of driving large masses of molecular gas to higher altitudes than contemporary starbursts and quasars. These effects may be most prominent in dense cluster atmospheres where the cooling gas supply is plentiful and buoyancy forces are large. Radio/X-ray bubbles encompass large volumes of gas that vastly exceed other AGN, where buoyancy effectively drives gas outward long after the AGN has ceased to power the radio lobes.

Understanding when molecular clouds are inbound or outbound is fraught with uncertainty. That most molecular gas lies off the nucleus shows much of it is outbound. But because their speeds lie well below the escape speed, some of the gas must be inbound. Our results will thus be biased to some degree. But quantities such as the lifted mass will be

affected by no more than a factor of two and will not qualitatively affect our conclusions. Lacking a complete sample, we are subject to selection bias, which likely will affect the properties of lower molecular gas mass systems that are undersampled. Selection biases will be addressed as sample sizes increase and unbiased samples become available.

Chapter 3

Radio jet-ISM interaction and the impact of radio-mechanical feedback in Abell 1795

In the previous chapter, we showed that radio-mechanical feedback can drive outflows of molecular gas in galaxies which can suppress star formation. However, most of the gas in galaxies does not escape. It either falls back fueling the BH and central starbursts or mixes with the hot gas and is heated to high atmospheres. However, when the radio jets are active, they can compress the gas in the outflow, thereby triggering star formation in positive feedback. In this chapter, we study one such well-studied system, Abell 1795 using the new XSHOOTER spectrum of the Hα and molecular gas filament together with previous multiwavelength observations to study the interaction between the radio-jets, ISM of the galaxy and star formation in the molecular gas outflows triggered by radio-jets.

The work in the following chapter has been submitted for publication to MNRAS. I am the first author of the manuscript. I was responsible for the reduction and analysis of the XSHOOTER, MUSE and ALMA data and I wrote the manuscript. The second author is my supervisor. Third author H. R. Russell led the XSHOOTER proposal to obtain the data. The remaining authors are collaborators who provided comments on how to improve the manuscript before submission for publication.

3.1 Abstract

We present XSHOOTER observations with previous ALMA, MUSE and *HST* observations to study the nature of radio-jet triggered star formation and the interaction of radio jets with the interstellar medium in the brightest cluster galaxy (BCG) in the Abell 1795 cluster. Using *HST* UV data we determined an ongoing star formation rate of 9.3 $M_{\odot}$ yr^{-1}. The star formation follows the global Kennicutt-Schmidt law, however, it has a low efficiency compared to circumnuclear starbursts in nearby galaxies with an average depletion time of ∼1 Gyr. The star formation and molecular gas are offset by ∼ 1 kpc indicating that stars have decoupled from the gas. We detected an arc of high linewidth in ionized gas where electron densities are elevated by a factor of ∼4 suggesting a shock front driven by radio jets or peculiar motion of the BCG. An analysis of nebular emission line flux ratios suggests that the gas is predominantly ionized by star formation with a small contribution from shocks. We also calculated the velocity structure function (VSF) of the ionized and molecular gases using velocity maps to characterize turbulent motion in the gas. The ionized gas VSF suggests that the radio jets are driving supersonic turbulence in the gas. Thus radio jets can not only heat the atmosphere on large scales and may quench star formation on longer timescales while triggering star formation in positive feedback on short timescales of a few million years.

3.2 Introduction

The Active Galactic Nucleus (AGN) feedback has become an integral part of galaxy simulations to limit the growth of massive galaxies via star formation and to explain the presence of young stellar populations in low redshift galaxies (e.g. Kauffmann & Haehnelt, 2000b; Schawinski et al., 2006; Croton et al., 2006; Scannapieco et al., 2012). Recent discoveries of massive gas outflows driven by intense radiation or radio-jets have demonstrated how effectively the energy released by an AGN can interact with its host environment (eg. Morganti et al., 2005; Nesvadba et al., 2006; Feruglio et al., 2010; Ruffa et al., 2019, 2022). By heating and expelling cold gas from a galaxy's centre, the AGN activity can limit the fuel available for star formation and accretion onto the supermassive black hole (SMBH) and thereby regulate galaxy growth.

The AGN feedback mainly occur in two phases, the "quasar mode" and the "radio mode". The quasar mode occurs when the cold gas accretes efficiently on the central SMBH, forming an accretion disk that emits at all wavelengths. The intense radiation and winds from the accretion disk disrupt the surrounding gas and terminate star formation in a negative

feedback (Fabian, 2012; Tombesi et al., 2015; Veilleux et al., 2020). In the low accretion efficiency regime, the radio mode feedback dominates (Russell et al., 2013). The radio jets inject energy into the atmospheres of galaxies and galaxy clusters by blowing bubbles, often seen as cavities or surface brightness depressions in X-ray images. The atmosphere is heated by a combination of shocks (Randall et al., 2011), turbulence (Zhuravleva et al., 2014), and the enthalpy released as the cavities rise, leading to suppression of cooling and star formation (McNamara & Nulsen, 2007, 2012; Donahue & Voit, 2022).

Although radio mode feedback is thought to maintain balance in the inner hot atmospheres of galaxies and clusters, AGN with pronounced radio jets are also prone to positive feedback (Zinn et al., 2013; Gaibler et al., 2012). Theoretical models predict positive feedback scenarios where a collimated jet or outflow compresses the surrounding interstellar medium (ISM) to trigger star formation, and stars form within radiatively-driven outflows as this material is compressed, cools and fragments (eg. Silk, 2013; Ishibashi & Fabian, 2012; Zubovas et al., 2013; Bieri et al., 2016). Star formation rates from jet-ISM interactions are observed to be limited (eg. van Breugel et al., 1985a; Crockett et al., 2012; Cresci et al., 2015; Salomé et al., 2016; Santoro et al., 2016). However, a different class of models and numerical hydrodynamical simulations have predicted an even more intriguing scenario where stars can form *inside* the outflowing clouds (Ishibashi & Fabian, 2012; Fabian, 2012; Zubovas et al., 2013; Yu et al., 2020). Some of these models expect that stars can form in this mode at a rate of up to 10-100 $M_\odot$ yr^{-1}. This exciting new mode of star formation would generate stars with high radial velocities, hence with kinematic properties different with respect to the galactic disk, and could contribute to the formation of the spheroidal components of galaxies (bulge, halo). Therefore, star formation in these flows would contribute to the morphological evolution of galaxies (eg. Gaibler et al., 2012) and could explain key aspects of galactic structure, including the mass-radius relation of early-type galaxies (eg. Ishibashi & Fabian, 2014) and 'inside-out' galaxy growth, where compact $z \sim 2$ galaxies form the cores of present-day massive ellipticals (van Dokkum et al., 2010; Ishibashi & Fabian, 2012).

Radio-jet induced star formation within their host galaxies has been detected in many objects at low (Nesvadba et al., 2021; Salomé et al., 2017, 2015) and high redshifts (Emonts et al., 2014; Nesvadba et al., 2020). Recent Very Large Telescope (VLT) observations of local ultra-luminous infrared galaxy (ULIRG) IRAS F23128-5919 obtained the first detection of star formation in outflowing gas occurring at a rate of 30 $M_\odot$ yr^{-1}, which is ~ 25 percent of the global star formation rate in this system (Maiolino et al., 2017). Although with lower resolution, recent studies using the MaNGA survey have found evidence for positive feedback and star formation in outflows in a significant fraction of galaxies (Gallagher et al., 2019; Rodríguez del Pino et al., 2019). Here we study another example of

well-resolved star formation within molecular gas flows driven by radio jets in the BCG of Abell 1795 galaxy cluster.

The central elliptical galaxy of the nearby cluster Abell 1795 hosts a powerful radio source, 4C 26.42, which is driving two massive 10^9 $M_\odot$ molecular gas flows (Fig. 3 Russell et al., 2017b). These extended cool gas filaments are each $\sim$ 7 kpc in length and visible in soft X-ray, Hα, CO and bright streams of star formation (eg. McNamara & O'Connell, 1993; McNamara et al., 1996a; Salomé & Combes, 2004; Crawford et al., 2005). The filaments project exclusively around the outer edges of two radio bubbles that have been inflated by the jet (van Breugel et al., 1984a; Fabian et al., 2001). The close spatial association with the radio lobes, together with smooth velocity gradients along their lengths and narrow velocity dispersions, show that the molecular filaments are gas flows entrained by the expanding bubbles as described in section 3.1 in (Russell et al., 2017b). For thick, clumpy shells of molecular gas around the radio bubbles, the column depth is greatest around the peripheries, and therefore this morphology will be detected as bright rims, as observed. The south (S) molecular filament appears to form an extension of a bright stream of young stars that are visible in *HST* FUV observations, but appears disconnected from the central clump and spatially offset from the UV emission (shown in Fig. 3.8). This striking spatial anti-correlation suggests that the molecular gas flow could be fuelling this burst of star formation. In this chapter, we study the interplay between the radio-jets, ionized and molecular gas and star formation using high spatial resolution multiwavelength observations of Abell 1795.

Throughout this paper, we use flat ΛCDM cosmology with $H_0 = 70$ km s^{-1} Mpc^{-1}, $\Omega_\mathrm{m} = 0.3$ and $\Omega_\Lambda = 0.7$. We adopt a redshift of 0.063001 (see section 3.3.5), where 1 arcsec corresponds to 1.21 kpc.

3.3 Observations and Data Reduction

3.3.1 XSHOOTER

The galaxy spectra were obtained with the X-SHOOTER spectrometer at the European Southern Observatory's Very Large Telescope (ESO-VLT) (Vernet et al., 2011). We selected 11″-long slit for all arms. The slit width was 1″ in the ultraviolet B (UVB) arm, and 0.9″ in the visible (VIS) and near-infrared (NIR) arms. This setting gives a spectral resolution of 5100, 8800 and 5300 in UVB, VIS and NIR arms, respectively. The full width at half maximum (FWHM) was 0.126 nm, 0.12 nm and 0.882 nm for UVB, VIS, and NIR arms

corresponding to velocity resolutions of $\sim$ 88 , 45 and 151 , respectively. The observations were taken between April 2018 and March 2019. The seeing during observations varied between 0.57″–1.24″ FWHM across exposures with a mean seeing of $\sim$0.84″. The slit was positioned with a position angle of 19° as shown in the left panel of Fig. 3.1. This orientation and slit width was chosen to enable the slit to sample both the S outflow filament and the star-forming knots to the NE of the nucleus whilst providing the required spectral resolution. Observations were executed in the OFFSET mode and interleaved with blank sky exposures of equal duration as that of the source, obtained at about 1 arcmin from the galaxy, for sampling the background. For each exposure, standard star observations were taken for flux calibration. The on-source integration time was 2 hours in the UVB and NIR bands, respectively, and 1 hour in the VIS band with a total integration time of 5 hours.

We performed data reduction and calibration in the ESOREFLEX software (version 2.11.0) using the recommended X-SHOOTER pipeline (version 3.5.0) (Freudling et al., 2013) following the standard steps summarised below (Modigliani et al., 2010). We analyzed each individual exposure independently. The data were corrected and calibrated for detector bias and dark current, detector pixel-to-pixel sensitivity variations, wavelength calibration, instrument and detector efficiency and response and background sky subtraction. The flux calibration was performed by analyzing the standard star spectrum to determine instrument and detector response. The final data product is a wavelength corrected, flux calibrated and background subtracted 2D spectrum of the slit for each exposure.

The observations were taken during different times of the year and the spectra generated by the pipeline were in the topocentric reference frame. Therefore, we applied radial velocity correction to change the spectrum to the barycentric frame of reference and resampled the spectrum at the original wavelength grid using `spectres`[1] package in Python for each exposure (Carnall, 2017). We then combined individual exposures for each arm to obtain the final 2D spectrum of the filament in UVB, VIS and NIR bands. We corrected the spectrum for Galactic foreground extinction estimated from the dust maps of Schlafly & Finkbeiner (2011) by adopting R_V of 3.1, the standard value for the diffuse ISM and Cardelli et al. (1989) extinction curve. The combined UVB and VIS band spectrum is shown in Fig. 3.2. We divided the area of the slit into 10 regions of $1.1'' \times 1''$ and extracted the spectrum from each region. Region 1 is $\sim$9.5 kpc to the S of the nucleus and region 10 is $\sim$3 kpc to the NE of the nucleus as shown in the left panel of Fig. 3.1. The BCG nucleus lies close to region 8.

[1] https://spectres.readthedocs.io/en/latest/

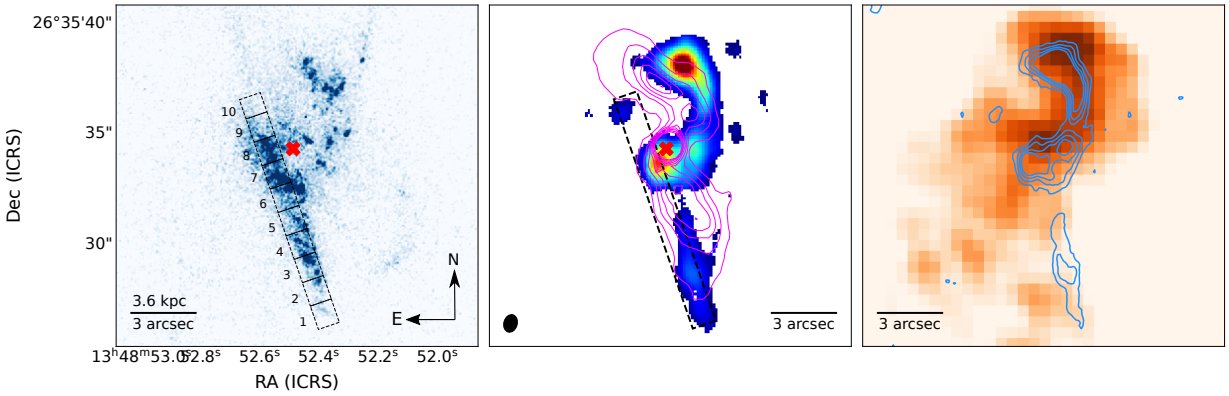

Figure 3.1: Left: *HST*F150LP image of the star formation in Abell 1795. The black dashed box shows the position of the X-SHOOTER slit. The numbers indicate the regions along the slit used to extract the spectra for studying gas and stellar kinematics. Center: Integrated CO(2-1) total intensity map with ALMA for velocities between −340 and 150 km s^{-1}. The dashed black box represents the orientation of the XSHOOTER slit relative to the molecular gas. We show radio contours at 8 GHz from the Very Large Array (VLA) from Bîrzan et al. (2008) in magenta. Right: *Chandra* 0.5–7 keV X-ray image shows the hot X-ray gas emission with molecular gas contours from CO overlaid in blue, where levels correspond to flux densities of 0.2, 0.3, 0.4 and 0.5 Jy/beam km/s. The red "X" denotes the location of the nuclear radio source.

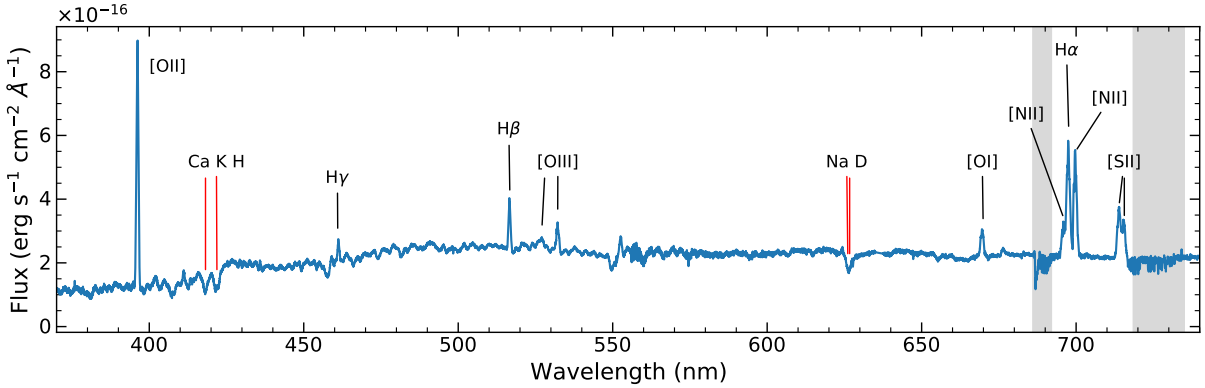

Figure 3.2: Combined UVB and VIS arm one-dimensional XSHOOTER spectrum of the slit in the observed frame. Grey regions are affected by atmospheric telluric lines. Nebular emission lines and stellar absorption lines (red) are indicated.

3.3.2 MUSE

We also analysed Multi-Unit Spectroscopic Explorer (MUSE) integral field unit (IFU) spectrograph data for Abell 1795. The observations were carried out on 05 February 2015 in seeing limited WFM-NOAO-N configuration (Program ID: 094.A-0859(A), PI: Hamer). The data were published and Hα velocity maps were discussed in Olivares et al. (2019). We reanalyzed the data to study other nebular emission lines together with ionized gas kinematics traced by Hα. Three exposures with an exposure time of 900s each were taken with a total on source integration time of 2700s. (Olivares et al., 2019) analyzed only one exposure with 900 s of on source integration time. For out study, we included all exposures for better signal to noise ratio. The field of view of $1' \times 1'$ covered the entire BCG including extended S Hα filament in a single pointing. Throughout the observation, the average seeing was $1.36''$.

The data were processed with esoreflex framework using MUSE pipeline version 2.8.5 (Weilbacher et al., 2020) with automated bias subtraction, wavelength and flux calibration, as well as illumination-, flat-field, and differential atmospheric diffraction corrections and sky subtraction. The final MUSE datacube maps the entire galaxy in the range 4750 Å$< \lambda <$9350 Å with a spectral resolution of $\sim$2 Å. The data were corrected for foreground Galactic absorption as explained in the previous section.

3.3.3 ALMA

The Atacama Large Millimeter/submillimeter Array (ALMA) observed Abell 1795 between 11 and 14 June 2016 for 72 minutes as part of program 2015.1.00623.S (PI: Helen Russell). Russell et al. (2017b) analyzed the data and discussed in detail the properties of the molecular gas in Abell 1795. For the purpose of this work, we re-analyzed the ALMA data and reproduced some of the results.

The data sets were calibrated with the ALMA pipeline reduction scripts in CASA version 4.7.2 (McMullin et al., 2007). We performed the standard phase calibration. Additional self-calibration did not improve the image root mean square (rms) noise. Line-free channels were used to subtract the continuum emission from the *uv* plane using the task UVCONTSUB. We then deconvolved and imaged the continuum subtracted CO(2-1) visibilities using the CLEAN algorithm with natural weighting to improve the sensitivity towards filamentary emission.

The final data cube is binned in 10 km s^{-1} channels with a per channel rms sensitivity of 0.64 mJy beam^{-1} and has a synthesized beam of $0.8'' \times 0.6''$ with a position angle of

−15.4 deg.

We summed the flux in each pixel in the data cube in a beam-sized region centred on the pixel. Then the spectrum of each pixel was fitted with one or two Gaussian components using the LMFIT package when emission was detected at greater than the 3σ threshold, based on Monte Carlo simulations of the spectrum with 1000 iterations. The best-fit parameters from this analysis were used to make velocity and FWHM maps of the molecular gas emission. All fluxes and linewidths are corrected for primary beam response.

3.3.4 *HST* and VLA data

We used Hubble Space Telescope (*HST*) images taken with F150LP, F702W and F555W filters in our analysis. All images were obtained from the Hubble Legacy Archive[2]. The F702W and F555W images each have total integration time of 1780 s (Proposal ID: 5212, PI: Trauger) and the F150LP image has the total integration time of 1300 s (Proposal ID: 11681, PI: Sparks).

We also used the Very Large Array (VLA) L and X band radio maps of the central radio source in Abell 1795 at 1.4 GHz and 8.2 GHz frequencies, respectively, from Bîrzan et al. (2008). We refer the reader to their paper for the details of data analysis.

3.3.5 Systemic velocity

We adopt a redshift of 0.063001±0.000016 corresponding to observed barycentric systemic velocity of 18887.2±4.8 km s^{-1} based on stellar population synthesis modelling of the spectra extracted from central region of the BCG as described in section 3.4.1. All velocities in this paper are calculated with reference to this velocity. We note that our adopted systemic velocity is 77.6 km s^{-1} smaller than the velocity adopted in Russell et al. (2017b); Olivares et al. (2019).

3.4 Data Analysis

3.4.1 Stellar kinematics

One of our goals is to study the motion of young stars in the filament of A1795. In principle, this can be done by allowing different velocities for young and old stellar components in

[2] https://hla.stsci.edu/

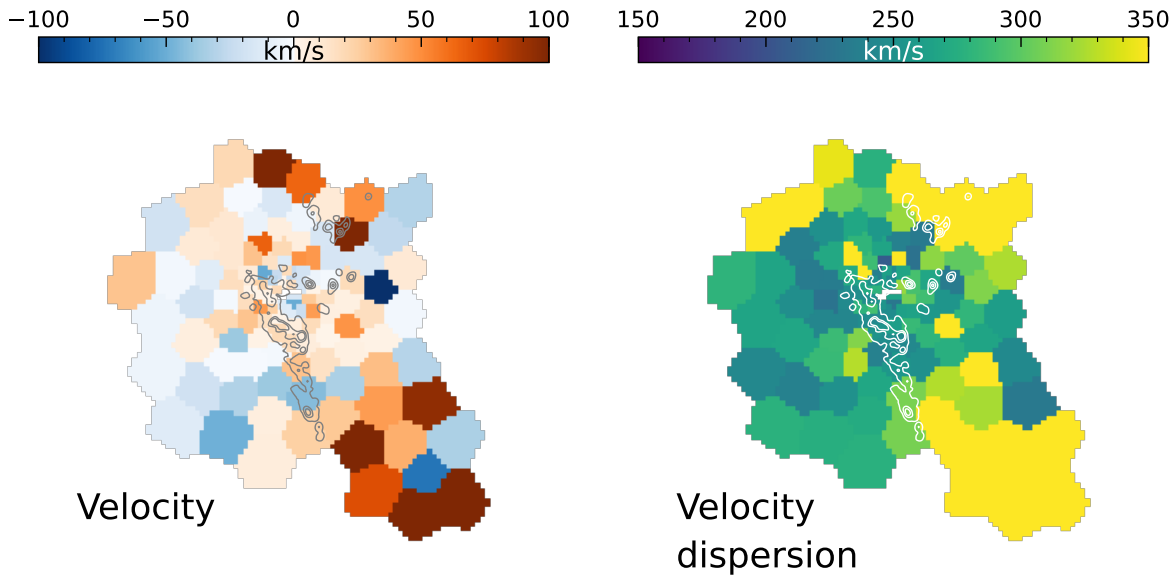

Figure 3.3: Voronoi binned stellar kinematics maps of A1795 with MUSE data. The left and right panels show velocity and velocity dispersion in the units of km s^{-1} in each bin, respectively. Each Voronoi bin has a line-free continuum signal-to-noise ratio of at least 50. The *HST*FUV150LP image contours smoothed with a gaussian kernel of 7 pixels indicating star formation are overlaid.

Region	Method 1		Method 2	
	Velocity (km/s)	σ (km/s)	Velocity (km/s)	σ (km/s)
1	34 ± 6	249 ± 6	-56.42 ± 17.09	261 ± 22
2	12 ± 5	270 ± 6	83.90 ± 12.08	298 ± 14
3	-5 ± 4	259 ± 5	-100.85 ± 6.99	212 ± 9
4	-5 ± 4	235 ± 5	-37.92 ± 5.60	231 ± 7
5	0 ± 4	232 ± 4	-24.82 ± 6.46	223 ± 8
6	7 ± 5	239 ± 6	19.22 ± 5.09	229 ± 7
7	0 ± 4	236 ± 5	18.06 ± 5.12	232 ± 7
8	-2 ± 4	243 ± 4	16.88 ± 5.66	236 ± 8
9	9 ± 3	235 ± 4	9.09 ± 6.20	241 ± 8
10	-2 ± 4	232 ± 5	9.65 ± 9.82	276 ± 13

Table 3.1: The table shows stellar velocities and velocity dispersions obtained using the two methods described in section 3.4.1.

the stellar kinematics fitting. However, in practice, it is extremely difficult to deblend the nebular line emission from stellar features due to the degeneracies introduced by additional degrees of freedom. The spectra of young stars are dominated by strong H and He absorption lines. The H absorption lines overlap with nebular emission lines and are very difficult to isolate. The presence of strong He absorption lines would allow the extraction of stellar kinematics of young stars. However, we did not detect He absorption lines in the spectrum of A1795. In the UVB band, less than 20% flux comes from a young (spectral type O to A stars) stellar population Crawford et al. (2005). The remaining flux is dominated by an older population of stars. The kinematics of the young stars can be determined from the broad sodium D (NaD) absorption lines at $\lambda\lambda$5890,5896 Å which are detected in the spectra. In the following section, we describe the methods used to study the kinematics of the stars using NaD lines and stellar kinematics fitting.

We used the penalized pixel-fitting (PPXF)[3] package to determine the line of sight velocity distribution (LOSVD) (Cappellari, 2017). The PPXF package uses Gauss-Hermite polynomials to parametrize the LOSVD. It measures deviations from pure Gaussian LOSVD. We fitted the spectra with a high-resolution stellar population synthesis library of González Delgado et al. (2005) (GD05) with Geneva isochrones. The GD05 library has a very high spectral resolution with an FWHM of 0.6Å. The resulting stellar velocities lie within $\sim$30 km s^{-1} of the systemic velocity with no clear gradient along the filament. The velocity

[3] https://pypi.org/project/ppxf/

dispersions lie in the range 230–270 km s^{-1}.

We tried estimating the kinematics of young stars by fitting the NaD lines manually. The NaD lines are a commonly observed feature in the spectra of early-type galaxies. In the presence of strong continuum and absorption lines, it is possible to separate NaD absorption into two components, one from the ISM and one from the stars, by fitting stellar population synthesis models. However, the continuum in our spectrum is weak and the absorption lines are affected by sky lines. Therefore, we extracted the observed frame spectrum from 6216Å and 6306Å which covers the absorption lines and part of the continuum. We fixed the Naλ5890/Naλ5896 ratio to 1.1 and fit absorption lines with a single Gaussian absorption profile. Regions of the spectrum affected by sky lines were masked during fitting. These fits overestimated the true FWHM, therefore we scaled them to match the FWHM calculated using ppxf following Hamer et al. (2016). Table 3.1 shows the velocities and standard deviations ($\sigma = \mathrm{FWHM}/2\sqrt{2\ln 2}$) of the stars estimated using both methods. In both cases, velocities are comparable to within 100 km s^{-1} of the systemic velocity. There is no velocity gradient along the filament. The velocities estimated using this method differ from the velocities estimated using the first method. The velocities estimated using ppxf uses the shape of the entire stellar continuum which also includes the Ca H & K lines and other features. The NaD absorption lines suffer from contamination from atmospheric lines adding extra uncertainty. In outer regions of the slit further away from the BCG where the difference between the two methods is largest, the absorption lines are weak making an accurate determination of their shape and location difficult and more uncertain. In inner regions, the difference in velocities is very small.

We also separately estimated stellar velocities of old stars in the BCG using the MUSE data cube. We applied the Voronoi tesselation technique using Vorbin[4] package (Cappellari & Copin, 2003). The MUSE data were binned into tesselations with a minimum signal-to-noise ratio of 50 in the line-free continuum. We modeled the spectrum extracted from each bin with PyParadise package[5]. PyParadise iteratively performs linear least squares fitting of line emission masked stellar continuum spectrum of every spectral unit. It also estimates best-fit line-of-sight velocity distribution with a Markov Chain Monte Carlo (MCMC) method independently. In Figure 3.3, we show the stellar velocity and velocity dispersion map of the entire BCG including the inner filament. The size of all Voronoi bins along the filament is comparable to the size of regions in the XSHOOTER slit. The stellar velocities are nearly uniform, with velocities lying between 50—100 km s^{-1} of the systemic velocity. There is no indication of a velocity gradient. The extension of bins to the SW is due to a nearby galaxy. The velocity dispersions in Abell 1795 vary between

[4] https://pypi.org/project/vorbin/
[5] https://github.com/brandherd/PyParadise

230—320 km s^{-1}. The stellar velocity dispersion in the central 1″ radius region is 259±18 km s^{-1} consistent with the central stellar dispersion values reported in the literature (e.g. Loubser et al., 2018).

The UV band imaging using *HST* clearly shows the presence of young stars in the filament and near the BCG centre. However, due to most of the light in the spectrum being dominated by older stars in the galaxy and the presence of strong nebular lines, we are unable to study the kinematics of the young stars in the BCG.

3.4.2 Ionized gas morphology

We used PyParadise to estimate the emission line fluxes in each spaxel in the MUSE data cube. The best-fit stellar continuum was generated for each spaxel as explained in the section above. It is subtracted from the spectrum, and the residuals are fit with a chain of linked Gaussians for each emission line with common velocity centroid, velocity dispersion and priors on emission line ratios. The errors in emission line fluxes are estimated from the Monte-Carlo bootstrap approach. The products from PyParadise were then used to make maps of Hα velocity, FWHM and flux.

In Figure 3.4 left panel, we show the flux density map of Hα gas in Abell 1795. The peak ionized Hα gas emission lies ∼0.6 kpc SE of the nuclear radio source, nearly co-spatial with the molecular gas in projection. There is a 7.6 kpc long bright filament of Hα wrapped around the outer edge of the north (N) radio lobe. There is another filament spanning nearly 14 kpc running NE to SW of the nuclear source. The S part of this filament extending 9.5 kpc to SW of the nucleus is nearly co-spatial with the radio lobes. The N filament is twice as bright as the S filament. These filaments are surrounded by fainter Hα emission. The MUSE FOV also covers the S outer ∼54 kpc long filament of Hα that coincides with the bright filament seen in X-ray images of the cluster (Crawford et al., 2005).

The total Hα luminosity in the zoomed-in region shown in Fig 3.4 covering the BCG and inner filaments is (4.180±0.002)×10^{41} erg s^{-1}. We can then estimate the mass of the ionized gas as (Osterbrock & Ferland, 2006),

$$M_{\rm ion} = \frac{\mu m_H L_{\rm H_\alpha}}{\gamma n_e}, \tag{3.1}$$

where μ is the mass per hydrogen atom which we fix to 1.4, m_H is the hydrogen mass, $L_{\rm H_\alpha}$ is the Hα luminosity and n_e is the electron density, which is 100 cm^{-3} (see section 3.7.2) and γ is the effective line emissivity. Assuming that the ionized gas is at a temperature of

Region	Velocity (km/s)			FWHM (km/s)		
	Comp 1	Comp 2	Comp 3	Comp 1	Comp 2	Comp 3
1	−96.66±0.25	−126.26±2.50		84.61±6.39	225.70±6.39	
2	−89.08±0.85	−130.13±1.14		70.62±1.59	163.71±1.59	
3	−185.83±0.61	−114.92±1.57		57.19±1.89	172.03±1.89	
4	−42.82±1.02	−191.76±2.61	123.88±2.08	110.08±2.67	149.01±5.62	192.33±4.53
5	−28.76±1.03	109.14±1.75	−154.72±9.67	102.37±3.00	185.91±3.16	294.02±14.92
6	−12.66±1.53	1.23±1.33		169.66±6.45	430.48±6.45	
7	−31.07±1.91	−364.60±2.96	59.89±1.70	129.58±5.83	162.59±7.58	482.85±3.03
8	−31.53±2.71	−258.54±4.60	136.16±8.76	153.42±8.96	303.08±7.74	397.57±12.94
9	−271.38±1.16	−127.74±6.91		148.38±9.26	576.07±9.26	
10	−267.79±0.47	−246.88±2.83		140.42±1.72	425.56±1.72	

Table 3.2: The velocities and velocity FWHM of the Hα emitting gas were measured by fitting multiple Gaussian components to their emission profiles in different regions extracted from the X-SHOOTER spectrum. The components are sorted according to their narrow to broad FWHM.

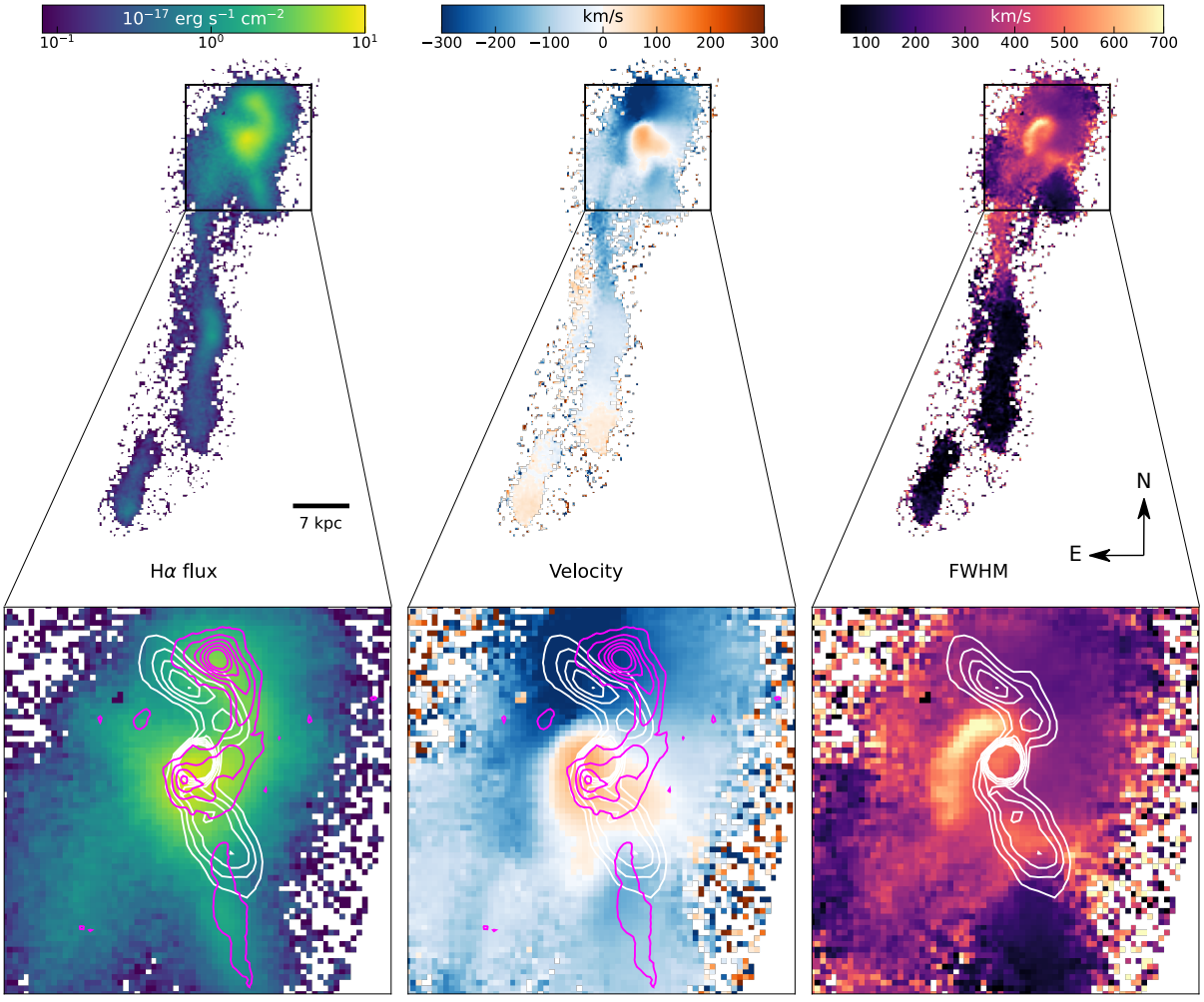

Figure 3.4: The figure shows the Hα flux (left), velocity (centre) and FWHM (right) map created from the MUSE data cube. Pixels where the FWHM is less than 800 km s^{-1} are shown. The VLA radio contours at 8 GHz from Bîrzan et al. (2008) are overplotted in white. ALMA CO(2-1) contours are shown in magenta in the left panels for comparison.

12,000 K, $\gamma \sim 3 \times 10^{-25}$ erg cm^3 s^{-1} (Baron & Netzer, 2019). The ionized gas mass in the galaxy is (1.640±0.001)×10^7 M$_\odot$.

3.4.3 Ionized gas velocity structure

The middle panel of Fig. 3.4 shows the velocity centroid map of Hα. The Hα gas in the centre surrounding the central radio source is redshifted to velocities of 100 km s^{-1} with respect to the BCG. The redshifted gas appears wrapped around the southern radio lobe in 'V'-shaped wings that extend out to ∼4.8 kpc on either side. They have a smooth velocity gradient from ∼0 km s^{-1} at the edges to 100 km s^{-1} at the centre of the BCG. There is a sharp change in velocities of the ionized gas at the edges of the redshifted gas from ∼100 km s^{-1} to −150 km s^{-1} to the E, W and S of the 'V-shaped wings. The gas immediately to the N–NE of the redshifted gas ∼2 kpc away from the BCG centre is blueshifted to velocities of −320 km s^{-1}, resulting in a sharp velocity change of ∼ 420 km s^{-1}. The reasons for sharp changes in velocity are not clear. It is likely that we are seeing separate Hα filaments projected along the line of sight where the redshifted gas is on the near side and blueshifted gas is on the far side. In that case, it would indicate that the redshifted gas is inflowing and the radio jets punched a hole in the gas causing the 'V'-shaped velocity structure, where the gas directly along the path of the radio jet is being blown away. Alternatively, the sharp change in velocity suggests that the region is experiencing a shock either caused by radio jets or the peculiar motion of the BCG in the cluster medium. Sloshing due to the peculiar motion of the BCG may also contribute to the observed velocity structure of the ionized gas. The sharp velocity gradient of 420 km s^{-1} is close to the BCG's peculiar velocity of 368 km s^{-1} with respect to the cluster's average velocity (Zabludoff et al., 1990). Alternatively, the gas may have cooled from the surrounding hot gas through interaction with the radio lobe in its wake. However, the Hα luminosity observed in Abell 1795 exceeds the luminosity expected if the gas were condensing from the hot ICM (McDonald et al., 2012a). Therefore, it is probably a combination of both.

The region of the sharp changes in velocities of the ionized gas is co-incident with large FWHM, as seen in the right panel of Fig. 3.4. In a region that appears like an arc to the N–NE of the central radio source where the velocity gradient is most extreme, the ionized gas has very high FWHM between 600–700 km s^{-1}. In the centre and along the inner edges of the 'V'-shaped wings, the FWHM are 400–500 km s^{-1}. The high FWHM along the boundary of the 'V'-shaped wings also drop sharply to ∼250 km s^{-1} to the NE of the nucleus, roughly co-spatial with the N molecular gas filament. The inner S filament has a narrow FWHM of 100–150 km s^{-1}. The arc of very high FWHM could be a result of beam smearing, where the region of sharp velocity gradient is poorly sampled due to large

seeing during observations. It can blend spectral features at different line of sight velocities leading to flattened spectrum and increased observed line of sight velocity dispersion. For example, a similar effect has been shown to greatly exacerbate the observed line of sight velocity dispersion at the centre of a galaxy for a single-component disk model (Davies et al., 2011). Still, the possibility of a shock cannot be completely ruled out. Higher spatial resolution spectroscopic studies of that region may provide a deeper insight. We note that Crawford et al. (2005) reported a rise in FWHM in the N filament. We do not detect any significant changes in FWHM in the N filament. Perhaps the single gaussian component fit does not capture the broad component properly if it is present.

We also estimated the gas velocities in the XSHOOTER spectrum of the inner filament. The simultaneous fit with the PPXF including gas emission lines leaves some residual structures. Therefore, we fitted gas emission lines manually. We subtracted the best-fit stellar continuum obtained from PPXF from the spectrum of the filament in each region of the slit to remove stellar absorption in H Balmer lines and the continuum. We fitted the residuals containing nebular gas emission line fluxes outside of PPXF. First, we simultaneously fitted Hα, [NII] doublet and [SII] doublets (Hα-[NII]-[SII] complex) with one Gaussian component for each line. The fit was performed such that all emission lines in this complex had the same velocities and line widths. Their intensities were allowed to vary independently. The relative intensities of the two [NII]6548,6584 lines were fixed to match the relative values of their Einstein transition coefficients. If there was significant flux in the residual with one Gaussian component, we fitted one or two more Gaussian components. The velocities and velocity widths of each component were independent of each other. The parameters of the fit were used to calculate the fluxes, velocities and line widths of all emission line components. The velocities and FWHM of the Hα lines from the XSHOOTER spectrum are shown in Table 3.2. We repeated this procedure separately for [OII] doublets, Hβ-[OIII] complex, and [OI] emission lines.

The velocity structure of the Hα gas is complex with several velocity components in the central regions. The average Hα velocity of all components in each region of the slit varies from -110 km s^{-1} in region 1 to -250 km s^{-1} in region 10. The outer regions (regions 1,2 and 3) of the filament have a narrow FWHM between 60–80 km s^{-1}, but require an additional broad component with an FWHM between $\sim$150–200 km s^{-1}. Regions 4,5,7 and 8 required three Gaussian components to account for all line emissions with velocities between -364 and 123 km s^{-1}. The velocity FWHM of these components vary from 50 to 250 km s^{-1} (see Fig. A1).

It is worth noting that the gas velocities are very distinct from the velocities of stars. The majority of the light in the MUSE spectrum is dominated by older F-K-type stars. The young stars forming within the gas in the filament are expected to have a smooth

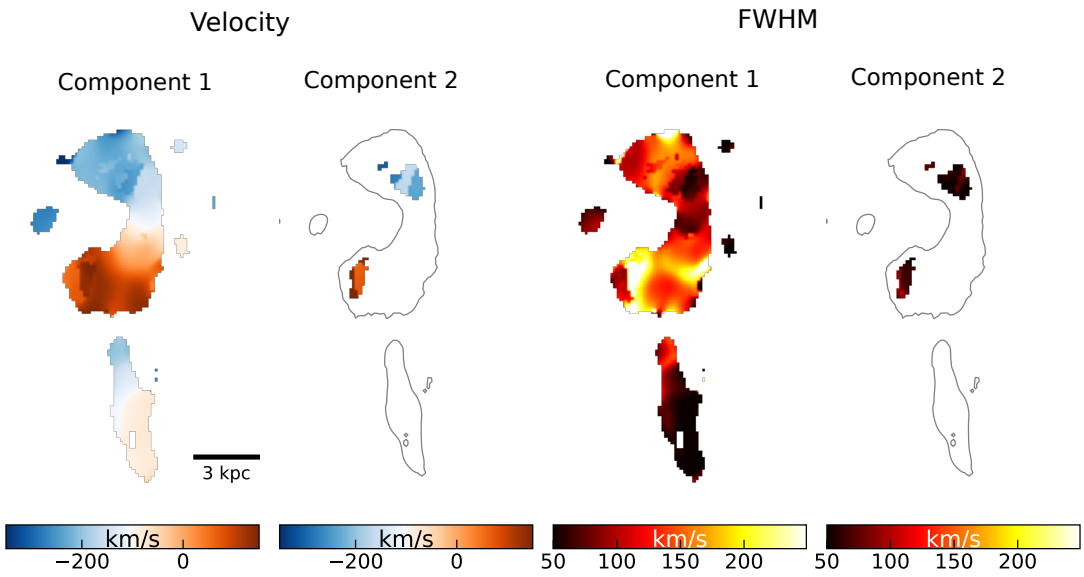

Figure 3.5: Velocity and FWHM maps of the two gaussian components in the spectrum of CO(2-1) observation are shown in the left and right panels, respectively. A 0.05 Jy km s^{-1} contour of the total CO(2-1) flux map for the first component is shown in both panels to guide the eye.

velocity gradient if they formed from the gas in the filaments. However, it is not possible to estimate the velocity of young stars from our data. Therefore, the nature of their motion remains unclear.

3.4.4 Molecular gas morphology

The majority of molecular gas in Abell 1795 is in filamentary structures to the N and S of the BCG. The S filament extends out to $\sim$ 9 kpc from the BCG centre. It is fainter than the N filament, containing 10 per cent of total molecular line emission, and is disconnected from the central lump of molecular gas. The N filament is clumpy and curved in an inverted 'C' shape and contains roughly 50 per cent of total molecular gas emission. Unlike S filament, it is connected to the central gas reservoir. A comparison with 5 GHz radio contours from Bîrzan et al. (2008) shows that the N filament wraps around the outer edge of the N radio jet. It is fainter at 2.4 kpc (2 arcsec) NW of the nuclear continuum source where the radio jet bends by $\sim$90° as shown in the middle panel of Figure 3.1. The S molecular gas

filament appears nearly co-spatial with the southern radio jet in projection in the sky plane. Molecular gas often forms on the edge or around radio bubbles from gas that was pushed away or lifted by the bubbles or jets (see for e.g. Russell et al., 2019). It is possible that the molecular gas has formed around the radio jets, but it appears co-spatial in projection. The central clump of molecular gas is slightly offset from the nuclear continuum source, with its brightest emission being 0.96 kpc (0.8 arcsec) SE of the nucleus, where the radio jet bends sharply by $\sim$90°.

There is a clear interaction between the molecular gas and the radio jets. The molecular emission peaks are nearly co-spatial with the bends in the radio jet. Either the central radio source is precessing (van Breugel et al., 1984b) or the collision of the radio jets with the dense ISM at surface brightness peaks in the molecular gas changes the path of the expanding radio lobes (van Breugel et al., 1985b; McNamara & O'Connell, 1993; McNamara et al., 1996b).

3.4.5 Velocity structure of the molecular gas

The velocity structure of molecular gas is fairly smooth in Abell 1795. The CO(2-1) emission in most of the regions can be well described by a single Gaussian component. However, a second component is required in two regions closer to the nucleus and in the N filament, where the radio jet takes sharp turns. The velocity and FWHM maps of both components are shown in Fig 3.5. The southern molecular gas filament has a smooth velocity gradient from -80 km s^{-1} to -200 km s^{-1} from the outer to the inner region. The FWHM is narrow in most of the filament at $\sim$40 km s^{-1} but increases to $\sim$100 km s^{-1} towards the inner region. The N filament has a narrower velocity gradient from -100 km s^{-1} to -370 km s^{-1}. The FWHM is fairly constant between 60 km s^{-1} to 100 km s^{-1} with no clear gradient. At the end of the N filament, it increases up to 300 km s^{-1}. The central reservoir has velocities between -30 km s^{-1} to 130 km s^{-1} and broader FWHM between $\sim$100 km s^{-1} and 250 km s^{-1}. The gas in the central region is dynamically distinct from the gas in the filaments. There is no indication of a rotating disk of molecular gas in the centre.

The second emission component located near the centre has velocities of $\sim$60 km s^{-1} with narrow FWHM of $\sim$70 km s^{-1}. The two velocity components are closer in velocity but their FWHM differ by $\sim$170 km s^{-1}. The second emission component in the N filament is blueshifted by 50 km s^{-1} compared to the first component with similarly narrow FWHM of $\sim$ 70 km s^{-1} as the first component.

3.4.6 Molecular gas mass

The molecular gas mass is estimated using the relation from Bolatto et al. (2013) as follows

$$M_{\rm mol} = 1.05 \times 10^4 \left(\frac{X_{\rm CO}}{X_{\rm CO,Gal}}\right)\left(\frac{1}{1+z}\right)\left(\frac{S_{\rm CO}\Delta v}{\rm Jy\,km\,s^{-1}}\right)\left(\frac{D_{\rm L}}{\rm Mpc}\right)^2 {\rm M}_\odot, \tag{3.2}$$

where $S_{\rm CO}\Delta v$ is the integrated flux density of the CO(1-0) line, $D_{\rm L}$ is the luminosity distance, z is the redshift, $X_{\rm CO}$ is the CO-to-H_2 conversion factor and $X_{\rm CO,Gal} = 2{\times}10^{20}$ cm^{-2} (K km s^{-1})$^{-1}$. The CO(1-0) flux density is estimated from CO(2-1) using the integrated line flux ratio CO(2-1)/CO(1-0) ≈ 3.2 based on similar ratios observed in BCGs (Russell et al., 2016; Vantyghem et al., 2016, 2017, 2018).

A major source of uncertainty in the mass estimate is the uncertainty in the $X_{\rm CO}$ factor. We assume the Galactic value for this factor which has an uncertainty of about 30% (Solomon et al., 1987). The true value of $X_{\rm CO}$ depends on the metallicity, temperature and density of molecular clouds (Bolatto et al., 2013). No direct estimates of $X_{\rm CO}$ are available for BCGs. However, the metallicities in the atmospheres of BCGs are close to the solar value and the linewidths of molecular gas clouds are similar to the molecular cloud linewidths observed in the Milky Way (Rose et al., 2019a; Tremblay et al., 2016). In RXCJ0821 BCG, the molecular gas was found to be optically thick indicating abundances close to the Galactic value (Vantyghem et al., 2017). Therefore, we believe the Galactic $X_{\rm CO}$ factor is appropriate for this BCG as well. If the true conversion factor is similar to that of ULIRGs, the molecular gas masses would be smaller by a factor of up to 5.

The total molecular gas mass in the BCG is $(3.2 \pm 0.2) \times 10^9$ M$_\odot$. Nearly fifty per cent of molecular gas mass is in the N filament with a mass of $(1.5 \pm 0.2) \times 10^9$ M$_\odot$. The S filament has a molecular gas mass of $(3.8 \pm 0.4) \times 10^8$ M$_\odot$.

3.5 Comparing CO and Hα emissions

To observe the coupling between Hα and molecular gas, we created combined MUSE and ALMA maps. We made CO moment 0, 1 and 2 maps with only one Gaussian component per spaxel similar to the method described in section 3.3.3. We applied an offset of $\sim 1.72''$ in RA to the MUSE Hα maps to align them with the ALMA images. The offset was determined by visually matching Hα and CO photocentroids and filaments assuming they are aligned. All features are aligned such that the uncertainty in alignment is smaller than the spatial FWHM of both instruments after applying the offset. Then the ALMA

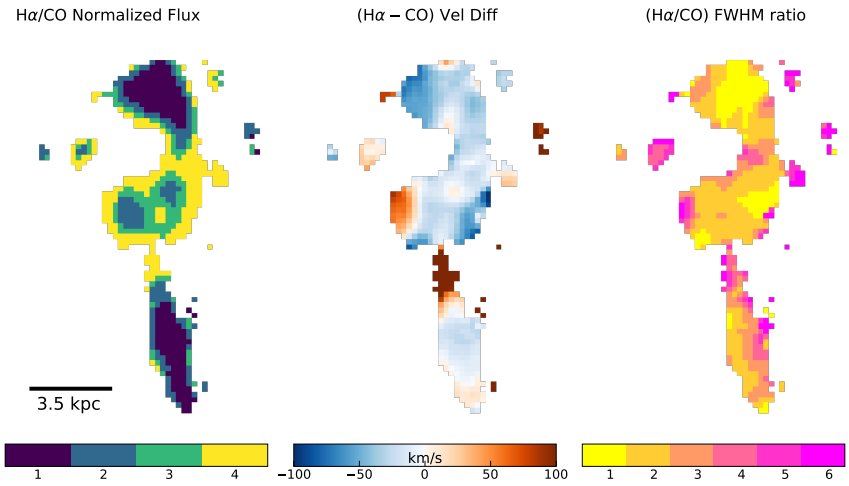

Figure 3.6: The figure shows maps of the ratio between the Hα and CO(2-1) linear normalized flux ratio, line-of-sight velocity difference and the ratios of their FWHM from ALMA and MUSE observations.

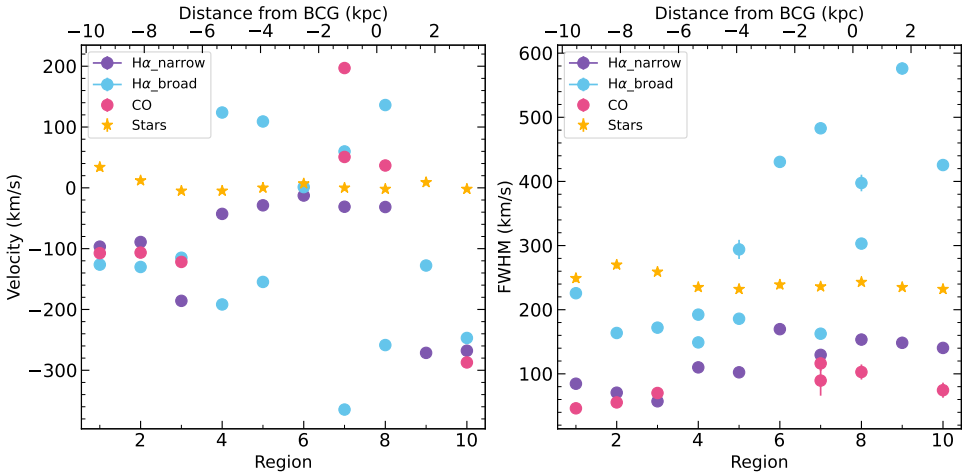

Figure 3.7: A comparison of the Hα, molecular gas and stellar velocities (left panel) and FWHM (right panel) in regions along the XSHOOTER slit. Stellar velocities using ppxf are plotted. The physical distances of regions from the nuclear radio source are shown on the top x-axis, where negative distances indicate regions to the south of the nucleus (see Fig. 3.1). The molecular gas is comoving with the Hα gas in the outer regions of filaments. The gases appear dynamically disconnected in central region.

image was reprojected onto the MUSE image using the REPROJECT package in Python. In Fig. 3.6, we show maps of the ratio of normalized Hα/CO(2-1) fluxes in the left panel. The flux ratio does not show strong spatial variation in the filaments indicating that the two phases are strongly coupled. In the central regions, Hα is 2–4 times brighter compared to the filaments perhaps because of additional ionizing radiation from the AGN, young stars and interaction with the radio lobes. The middle panel of Fig. 3.5 shows the velocity centroid difference between the two gas phases. The ionized gas appears to be comoving with the molecular gas in most of the galaxy as indicated by a fairly constant velocity gradient. However, at the inner end of the S filament and E end of the central clump, the ionized gas has a velocity in excess of 100 km s^{-1} relative to the molecular gas. The molecular and ionized gases are very likely directly physically related where most of the ionized gas is the outer region of molecular gas clouds. Therefore, they are expected to have the same velocity structure. The FWHM of the Hα gas is 2–4 times higher than the FWHM of the molecular gas. This is consistent with observations of ionized and molecular gas in other BCGs (Tremblay et al., 2018; Olivares et al., 2019). The Hα gas is more extended than the molecular gas. Therefore, the line of sight crosses more Hα gas than molecular gas, perhaps with different layers of gases at different speeds, resulting in a broad FWHM. The ionized gas also has a higher temperature and lower density. Therefore, it can be shock excited relatively easier than the molecular gas increasing its FWHM.

We compared the velocity and FWHM of the Hα gas to that of the molecular gas within regions used in the XSHOOTER slit. We extracted the molecular gas spectrum and fitted it with one or more Gaussian components similar to the process described in section 3.4.3. In this way, we can see the effect of a line of sight on the velocities. Figure 3.7 shows the relationship between velocities and FWHM of the two gas phases along the XSHOOTER slit. The velocities of narrow components of Hα gas are comparable to velocities of the cold molecular gas in the outer regions of both the N and the S filaments (regions 1-3 and 10). In central regions, the coupling between the two phases is more complex. The FWHM of Hα gas is more than 10 times the FWHM of molecular gas for the broad component. The interaction between the radio jet and the ISM is strongest in central regions. Central regions also overlap with dust. If the ionized and molecular gases are mixed with dust, individual layers of ionized gas along the line of sight moving at different velocities will suffer different levels of extinction depending on the location of the dust. It will affect the shape of the emission lines resulting in velocities appearing shifted compared to true their velocities. In the rest of the filament, at least one component of the Hα gas appears coupled to the molecular gas. Thus, multiple gaussian components could be tracing the gas at different locations along the line of sight moving at different speeds.

3.6 Star formation

The bright UV emission seen in *HST* images hints at recent or ongoing star formation in Abell 1795. The UV emission predominantly appears around radio lobes in filaments and the central region with several bright knots of UV emission. It is co-spatial with the molecular gas in the centre and in the N filament of the galaxy. However, it is offset from the molecular gas filament to the S of the galaxy. The southern molecular gas filament is broken from the central gas clump, however, the southern UV filament appears continuous (see Fig.3.8, the middle panel). A similar trend is observed in the central reservoir where bright knots of star formation seen in the UV image is offset from the bright molecular gas emission regions.

Several studies have estimated the total star formation rate in A1795 between less than 1 $M_{\odot}$ yr^{-1} to 20 $M_{\odot}$ yr^{-1} (McDonald et al., 2010; Crawford et al., 2005; McNamara & O'Connell, 1989; Hicks & Mushotzky, 2005; Donahue et al., 2011) using various techniques and data at different wavelength ranges. Most star formation rate estimates using UV imaging lie between 10 and 20 $M_{\odot}$ yr^{-1} depending on the assumed star formation history and the initial mass function (IMF). For our analysis, we estimated the UV star formation rate using an *HST* UV image.

Big blobs of UV emission seen in ground-based observations are well-resolved in *HST* UV images. We measured the flux of the entire UV emission region in the *HST* F150LP image. We used Starburst99[6] code (Leitherer et al., 1999) to generate model spectra of young stellar populations assuming solar metallicity ($Z \sim 0.02$) and GENEVA 2000 tracks. We used both continuous star formation and single burst star formation histories assuming the Salpeter IMFs with slopes of 1.3, 2.3 and 3.3. We used the models with an age of 10^7 years, which is consistent with the sound speed rise time of inner radio bubbles of $\sim$7 Myr (McNamara et al., 1996a), as well as the age of the young stellar population of $7.5^{+2.5}_{-2.0}$ Myr in the S filament estimated using far-UV spectroscopy (McDonald et al., 2014). We applied foreground extinction to model spectra assuming a colour excess of E(B-V) of 0.0116 based on dust maps of Schlafly & Finkbeiner (2011). We also applied intrinsic extinction calculated from the ratio of Hα and Hβ emission line fluxes integrated over the area covering the star-forming filaments and scaled using methods described in section 3.7.1. We estimated average intrinsic extinction A_V $\sim$0.6 in the galaxy using Cardelli et al. (1989) extinction curve. The extincted models were convolved with the *HST* F150LP filter to establish a relationship between star formation rate and UV flux. The total SFR in 7 kpc radius aperture is 9.3$\pm$0.4 $M_{\odot}$ yr^{-1} and 21.3$\pm$3.1 $M_{\odot}$ yr^{-1} for

[6] https://www.stsci.edu/science/starburst99/docs/default.htm

continuous and instantaneous star formation histories, respectively, for IMF slope of 2.3. An IMF slope of 1.3 yields lower SFRs of 1.5±0.1 and 8.1±1.2 $M_\odot$ yr^{-1}, respectively, for the two star formation histories. Assuming a top-heavy IMF with a slope of 3.3 yields unrealistically high SFRs of 581 and 758 $M_\odot$ yr^{-1}. Therefore, the IMF slope in A1795 is most likely bottom-heavy with a slope between 1.3 and 2.3.

3.6.1 Radio lobe-ISM interaction

Almost all star formation knots appear on the outer regions of radio lobes providing strong evidence for star formation triggered by radio lobes. Similar spatial association between radio lobes and star formation is observed in several radio galaxies (Duggal et al., 2021; Lacy et al., 2017). Radio lobes can potentially compress the gas in the interaction region and send shocks causing gravitational collapse. We calculated the pressure in the region of interaction between the radio lobes and the ICM following methods described in Lacy et al. (2017, section 4.2) that are summarized below. The pressure in the interaction region required to produce the observed synchrotron radio emission assuming minimum energy density is given by:

$$p_{\rm me} = \frac{u_{\rm me}}{3} = \frac{7}{9}\frac{B_{\rm me}^2}{2\mu_0}, \tag{3.3}$$

where

$$B_{\rm me} = 5.69\times10^{-9}\times\left[\frac{1+\kappa}{\eta}(1+z)^{(3-\alpha)}\times\frac{1}{\theta_x\theta_y\ s\ \sin^{1.5}\phi}\frac{S_0}{\nu_0^\alpha}\frac{\nu_2^{\alpha+0.5}-\nu_1^{\alpha+0.5}}{\alpha+0.5}\right]^{\frac{2}{7}}, \tag{3.4}$$

μ_0 is the permeability of free space, κ is the ratio of energy in free particles to electrons assumed to be 100, η is the filling factor of the emission region assumed to be 1, $\theta_x = 1.2''$ and $\theta_y = 1.1''$ are beam sizes, s is the path length through the source which we estimate to be 4 kpc, ϕ is the angle between the magnetic field and line of sight assumed to be 45°, $S_0 = 0.03$ Jy/beam is the mean surface brightness of the emission, $\alpha = -0.8$ is the spectral index, ν_0 =1.5 GHz is the observed frequency and $\nu_1 = 120$ GHz and $\nu_2 = 0.3$ GHz are the upper and lower cutoffs of the synchrotron spectrum. We used the VLA L band image of A1795 at 1.5 GHz to calculate the mean surface brightness in the region and the radio beam size while keeping all other parameters the same as in Lacy et al. (2017). The pressure in the interaction region estimated using above method is 3×10^{-10} dyn cm^{-2}. The thermal pressure of the ICM calculated from X-ray observations at 5 kpc is $\sim4.5\times10^{-10}$ dyn cm^{-2}. It is comparable to the pressure in the interaction region suggesting that the region of interaction between radio lobes and the ICM is not overpressured and that radio lobes can

only produce weak shocks. The minimum pressure required to support the molecular gas in Abell 1795 is $\sim 10^{-8}$ dyn cm^{-2} (Russell et al., 2017b). It is larger by at least an order of magnitude suggesting that the structure of gas is supported by magnetic fields. Thus, radio jets can create low-velocity shocks in the gas in the interaction region, that could couple more effectively to the ISM than strong shocks (Appleton et al., 2013).

3.6.2 The role of dust

Dust also plays a key role in cooling the gas and facilitating star formation. The left panel of Fig. 3.8 shows a strong dust lane in the galaxy along with star-forming locations. The dust is draped around the N radio lobe, co-spatial with the molecular gas in projection, perhaps entrained by the radio lobe. Typically dust would sputter in the hot atmosphere of the ICM on a short timescale of $\sim$1 Myr (Vogelsberger et al., 2019). However, its presence suggests that it is shielded, perhaps by magnetic fields. Donahue et al. (2011) detected Polycyclic Aromatic Hydrocarbons (PAHs) which are the smallest dust grains and molecular hydrogen lines at $\sim$8–13 μm in the rest frame using *Spitzer* mid-IR spectrum, and also concluded that the dust is shielded from the ICM and X-ray radiation. However, dust can also grow quickly to detectable levels from cooling of warm ($< 10^7$ K) gas drawn up by radio jets (Qiu et al., 2020). Edge et al. (2002) detected molecular H_2 and FeII 1.6μm lines in their IR spectrum of the BCG. They used a larger 1.22 arcsec wide slit centred on the BCG nucleus where there is a significant amount of dust. We did not detect H_2 or FeII emission lines in the NIR XSHOOTER spectrum of the S filament at a level of 1×10^{-16} erg s^{-1} cm^{-2} $^{-1}$. There is no visible level of dust in the southern filament in *HST* images. Dust could be hidden behind the stars, therefore not being visible. Nevertheless, the presence of dust in the centre and the N filament could have enhanced the cooling of molecular gas and star formation in those regions.

3.6.3 Star formation efficiency

We compared the star formation surface brightness with molecular gas surface brightness to study the efficiency of star formation. First we aligned the *HST*F555W and *HST*702W images with the *HST*150LP image such that the bright star-forming knots at the far end of the N filament visible in the UV and optical images are aligned. We then determined the offset between the central bright point source seen in the optical images which does not have a UV counterpart, with the location of the ALMA nuclear continuum source assuming they are both originating from the AGN. The offset determined also aligned the

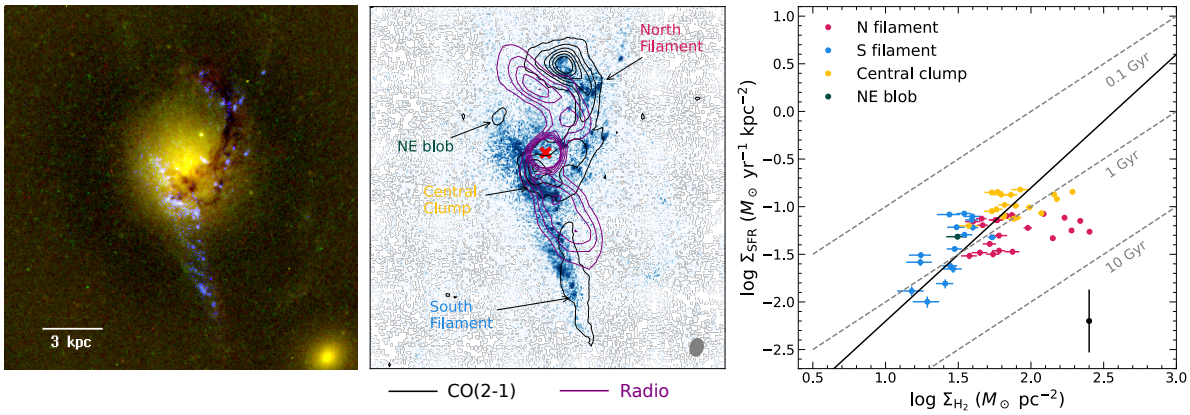

Figure 3.8: The left panel shows an RGB image with smoothed model subtracted *HST*F702W and *HST*F555W images in red and green, respectively, and *HST*F150LP image in blue. The middle panel shows the *HST*F150LP image overlaid with CO(2-1) line emission contours in black and VLA X-band radio contours in purple. The right panel shows the relationship between $\Sigma_{\rm SFR}$ and $\Sigma_{\rm H_2}$ in ALMA beam-sized regions for different areas across the galaxy. The black line shows the global Kennicutt-Schmidt relation. Dashed grey lines show different molecular gas depletion timescales.

molecular gas and dust lanes very well. Then, we smoothed the *HST* image by a Gaussian kernel whose FWHM and position angle were the same as that of the synthesised beam in the ALMA image. We then re-sampled the *HST* image onto ALMA's pixel grid using the `reproject` package in Python. The CO(2-1) and UV fluxes were calculated in ALMA beam-sized regions. The CO(2-1) flux was converted to molecular gas mass as explained in section 3.4.6 and SFRs were estimated from UV fluxes as explained in section 3.6 assuming continuous SFH and an IMF slope of 2.3.

The right panel of Fig. 3.8 shows the relationship between $\Sigma_{\rm SFR}$ and $\Sigma_{\rm H_2}$ in different parts of the galaxy estimated by dividing the SFR and molecular gas mass by beam area in appropriate units, respectively. Most of the points lie close to the Kennicutt-Schmidt (KS) relation (Kennicutt, 1998) shown as a black line, characterized as $\Sigma_{\rm SFR} \propto \Sigma_{\rm gas}^{1.4}$. A few regions in the N filament lie well below the KS relation. They are located where the radio jet bends around the brightest molecular gas emission in the N filament suggesting that the star formation efficiency is lower in these regions. Alternatively, either the molecular gas mass is overestimated or the star formation is underestimated. The molecular gas mass can be overestimated if the $X_{\rm CO}$ conversion factor is lower. The $X_{\rm CO}$ factor depends primarily on the density, metallicity and temperature of the molecular gas. In highly

starforming regions, the $X_{\rm CO}$ is up to a factor of five below its Galactic value, due to high gas temperature and velocity dispersion (Bolatto et al., 2013). These regions have high molecular gas FWHM (see Fig. 3.5) suggesting that molecular gas masses could have been overestimated. On the other hand, star formation can be underestimated if the underlying IMF is top-heavy. However, top-heavy IMF yields very high star formation rates which is unlikely to be the case.

These results indicate a lower star formation efficiency than circumnuclear star formation in nearby star-forming galaxies with similar gas densities. This is in agreement with the jet-induced star formation observed in other galaxies (see e.g., Salomé et al., 2016; Zovaro et al., 2019). We estimated average molecular gas depletion times due to star formation ($\tau_{\rm depl,SFR} = {\rm M_{H_2}/SFR}$) of 1 Gyr assuming star formation continues at 9.3 $M_\odot$ yr^{-1}. The $\tau_{\rm depl,SFR}$ in the S filament and the central clump is $\sim$ 0.8 and 0.9 Gyr, respectively. It is twice as long in the N filament at 1.7 Gyr. These timescales are much longer than the age of the stellar population and the radio lobes. However, most of the molecular gas in Abell 1795 is flowing. Assuming it is being driven out of the galaxy at a rate of $\sim$ 54 M$_\odot$ yr^{-1} (Tamhane et al., 2022), the molecular gas in the galaxy will be depleted within $\sim$6$\times$10^7 years, which is much shorter than $\tau_{\rm depl,SFR}$. Thus, although radio jet-ISM interaction may have triggered star formation, this form of star formation has lower efficiency and may be quenched eventually by the negative feedback of radio jets.

3.6.4 The offset between stars and molecular gas

The break in the southern molecular gas filament is coincident with bright Hα and UV emission. Overall, the southern molecular gas filament is offset from the star-forming filament by $\sim$0.4 kpc in the perpendicular direction if the molecular gas filament were to extend to the centre and $\sim$1 kpc in the direction of the filament. Similar offsets between star formation and cold gas have also been found in NGC1275 and simulations of AGN feedback (Canning et al., 2014; Li et al., 2015). We discuss two possibilities when this can happen.

First, the ram pressure of the expanding radio lobes has most likely triggered star formation in Abell 1795. If molecular gas was present at all locations where star formation is observed, then the star formation may have consumed it in the inner region of the S filament and its NE extension. Supernova feedback from young stars can also destroy the molecular gas around them. Assuming that the region of S star-forming filament that lacks molecular gas previously had molecular gas with the same surface density as in the S molecular gas filament, star formation would have to proceed at 70 M$_\odot$ yr^{-1} to consume

the molecular gas within 10^7 years, which is the time since the onset of star formation. This star formation rate is 5–7 times longer than observed star formation rates. At the observed SFR, it would take few 10^8 yrs to consume the molecular gas in that region, which is about an order of magnitude or more longer than the age of radio lobes and inner X-ray cavities (Kokotanekov et al., 2018). Even if we assume that the star formation proceeded at a higher rate than observed, it is not clear why gas in other parts of the S filament has not yet been consumed. If we assume that the ram pressure due to radio lobes is not strong enough in the outer part of the molecular gas filament to trigger star formation, it still does not explain the large amount of molecular gas in the N filament, where star formation is observed in the region of interaction between radio jets and molecular gas.

Alternatively, stars formed in the molecular gas filament have decoupled from the flow and are moving in the gravitational potential of the galaxy without significant resistance, whereas the molecular gas is acted upon by the ram pressure from the radio lobes and the ICM. It is similar to gas stripping in jellyfish galaxies, where the ram pressure of the ICM strips the gas from infalling galaxies while the stars in the galaxy are unaffected (see for example, Fumagalli et al., 2014). If the S filament is an inflow, stars would always lead the gas, as the gas would slow down due to the ram pressure of the ICM and radio jet. It can also explain the extension of the UV emission to the NE of the BCG nucleus, where the stars falling ballistically would overshoot the nucleus and are moving in that region. In this scenario, the stars are leading the gas by $\sim$1 kpc. For a $\sim$7 Myr old stellar population to have 1 kpc separation from the molecular gas, it would need to have an initial velocity of $\sim$400 km s^{-1} in the rest frame of the BCG, for filament with a cylindrical filament with diameter of 100 pc and a density of 2 cm^{-3} (see section 4.2 of Li et al., 2018). The It is higher than the stellar velocity dispersion in the BCG of 297 km s^{-1} but close to the average velocity of cluster galaxies of 368 km s^{-1} relative to the BCG. On the other hand, if the S filament is an outflow, the spatial offset can arise if the molecular gas decelerates slower than the stars, thus traveling further. Velocity of young stars in the filament maybe able to confirm whether S filament is an inflow or an outflow. A high-resolution far-UV spectrum of the inner filament where the contribution of old stars and nebular emission lines would be minimal is required to obtain the velocities of young hot stars in the filament.

3.7 Emission line ratios

As discussed in section 3.4.2, the products of PyParadise allowed us to make maps of emission line fluxes. We use these maps to determine the excitation state of the ionized gas, its density and dust extinction in the galaxy as discussed in the sections below. The

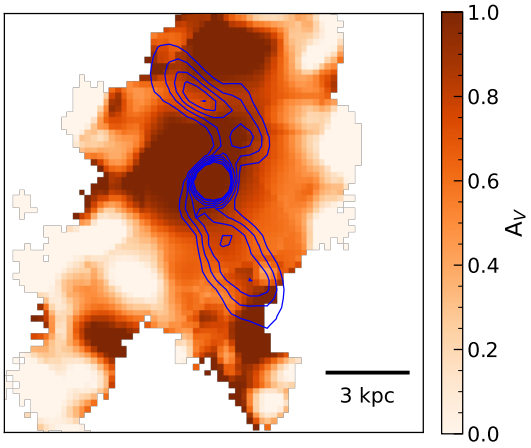

Figure 3.9: A map of extinction in the visual band (A_V) calculated as explained in section 3.7.1. Radio contours in the VLA X-band are overlaid in blue.

original maps were noisy. We smoothed the MUSE data cube by a Gaussian kernel with FWHM of 1″.3, equal to the seeing during the observations and fit spectra from each spaxel using PyParadise as discussed in section 3.4.2 to reduce the noise in the maps of low-intensity nebular emission lines.

3.7.1 Extinction map

Abell 1795 hosts a very prominent dust filament in the N roughly co-spatial with the molecular gas as shown in the left panel of Fig. 3.8. Therefore we expect significant dust extinction in the galaxy. We estimated the amount of visual extinction (A_V) by making a map of the ratio of Hα/Hβ Balmer decrement and scaled it to calculate E(B−V) as follows (Domínguez et al., 2013):

$$E(B-V) = \frac{2.5}{k(\lambda_{\mathrm{H}\beta}) - k(\lambda_{\mathrm{H}\alpha})} \log_{10}\left[\frac{(\mathrm{H}\alpha/\mathrm{H}\beta)_{\mathrm{obs}}}{(\mathrm{H}\alpha/\mathrm{H}\beta)_{\mathrm{int}}}\right], \tag{3.5}$$

where $k(\lambda_{\mathrm{H}\beta}) \approx 3.7$ and $k(\lambda_{\mathrm{H}\alpha}) \approx 2.63$ are extinction curves evaluated at Hβ and Hα wavelengths, respectively, given by Cardelli et al. (1989) and we assume $(\mathrm{H}\alpha/\mathrm{H}\beta)_{\mathrm{int}} \approx 2.86$ for an electron temperature of T=10^4 K and electron density of $n_e = 10^2$ cm^{-3} for Case B recombination. A_V is then simply calculated as $R_V \times$ E(B−V), where $R_V = 3.1$.

In Figure 3.9, we show the map of A_V in the BCG. Only spaxels with S/N>3 for both lines were considered. The spaxels with $A_V < 0$ were masked. As expected, there is a significant amount of extinction in the centre and the N filament with A_V exceeding 1 mag. The S filament has much lower extinction, indicating a low amount of dust compared to the N filament. It is consistent with the absence of a visible level of dust in the optical image of the S filament (see left panel of Fig. 3.8), as well as the non-detection of dust emission features in the NIR XSHOOTER spectrum of the S filament. Again we note that if most of the gas is on the near side of dust along the line of sight, it will not suffer from as much extinction as it would if dust and gas are mixed or if the gas is on the far side of dust in the S filament. The average extinction in the region covering both filaments is 0.6. Interestingly, the dust in the centre is predominantly to the NE of the nucleus, roughly co-incident with the shocked region, assuming the extinction map traces dust in the galaxy. Also, the north radio lobe appears to bend around the north blob of dust. It is also the location of the brightest CO emission indicating a large amount of molecular gas. Therefore it appears that the gas has changed the direction of the radio lobes. We use this extinction map to deredden emission line fluxes in the galaxy in a similar way as in the process described in section 3.6. In the following sections, emission line fluxes in each spaxel are corrected by the level of extinction measured in that spaxel.

3.7.2 Electron density

The high-resolution spectra allow us to resolve the [SII] doublets. The relative intensities of [SII]λ 6716 to [SII]λ 6731 can be used to estimate electron density (n_e) in the gas, since the doublets are sensitive to the effects of collisional de-excitation and insensitive to variations in electron temperature, due to their similar excitation energies. Therefore, their excitation rate depends on the ratio of the collision strengths and the ratio of line intensities depends only on the density of the gas (Osterbrock, 1989). We scaled the [SII]λ 6716/[SII]λ 6731 ratios to get estimate n_e following the procedure given in Proxauf et al. (2014), where we assumed electron temperature $T_e \sim 10^4$ K. This method is only reliable for gas densities between 100 and 1000 cm^{-3}. In Figure 3.10, we show the n_e map of the BCG. The electron densities in the filament are $\sim$ 100 cm^{-3} and potentially lower, as for densities lower than 100 cm^{-3}, [SII] line ratio becomes ineffective and can only provide an upper limit. In the center, $n_e \sim 100$ cm^{-3}. It is consistent with previous studies and [SII] line ratios found in other BCGs (Crawford et al., 1999; Hamer et al., 2016). To the N-NE of the centre, on the outer edge of the central radio source, electron densities are enhanced to $\sim$400 cm^{-3}. This feature is co-spatial with the high FWHM arc shown in Figure 3.4. As discussed in section 3.4.3, it could be a result of two separate gas filaments along the line

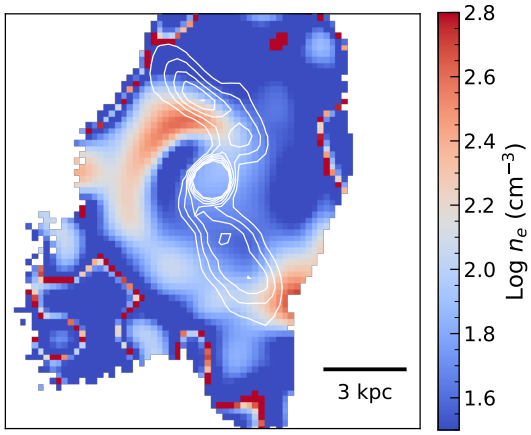

Figure 3.10: The figures show an electron density map derived from [SII]λ 6717 / [SII]λ 6732 as explained in section 3.7.2. Radio contours in the VLA X-band are overlaid in white.

of sight superimposed in projection and beam smearing. However, if the region is shocked, the density contrast between the pre and post-shocked medium is likely greater than four, suggesting the shock could be isothermal. In that case, the shocked gas will radiate away its energy and cool rapidly to form cold gas.

3.7.3 Excitation state

The [NII] to Hα ratio can probe the excitation state of the gas due to its sensitivity to AGN. Generally, star formation has a softer radiation field than AGN. Thus, changes in the [NII]/Hα ratio in a galaxy indicate different gas excitation mechanisms in different parts of a galaxy. In Figure 3.11, we show the [NII]/Hα map of the BCG. The ratio in the S filament is less than 0.7, whereas, in the centre surrounding the radio lobes, the ratio is more than 1. It decreases gradually away from the centre. At $\sim$4 kpc south of the nucleus, the ratio changes sharply from $\sim$0.85 to less than 0.7. The transition occurs at the tail end of the redshifted 'V'-shaped redshifted wings observed in Fig. 3.4. The excitation ratio in the region of high FWHM arc is highest at closer to 1. This suggests that the gas in the central region is more highly ionized by AGN activity than the gas in the outskirts, perhaps by shocks or AGN photoionization. The higher levels of gas excitation towards the

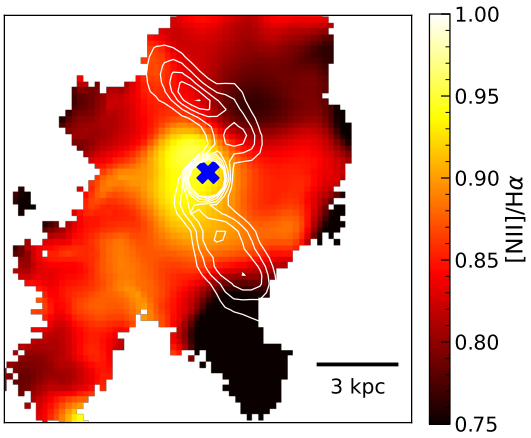

Figure 3.11: The ratio of [NII]/Hα represents the excitation state of the ionized gas. The blue cross denotes the location of the nuclear radio source. The VLA X-band radio contours are overlaid in white.

centre compared to outer regions indicates an increasing contribution from AGN similar to the trend observed in other BCGs (Hamer et al., 2016). In the following section, we try to disentangle the relative contribution of different excitation mechanisms.

3.7.4 Optical diagnostic diagrams

The broad wavelength coverage of the spectrum allows us to use ratios of various gas emission lines to try to determine gas excitation mechanisms. The most commonly used diagnostics line ratios are [NII] λ6583/Hα, [OI] λ6300/Hα, [SII] λ6716, 6731/Hα, and [OIII] λ5007/Hβ, the so-called BPT diagnostic diagrams (Baldwin et al., 1981). They are generally used to approximately differentiate between different excitation mechanisms. Figure 3.12 shows BPT diagnostic diagrams of the BCG generated using MUSE spaxels of individual line maps. Regions predominantly populated by star-forming, AGN and composite galaxies as identified by Kauffmann et al. (2003); Kewley et al. (2001) and Schawinski et al. (2007) are shown by grey solid, dashed and dash-dotted lines, respectively. The points are coloured by the regions in which they sit. The vast majority of points have composite or LINER-like ionization sources involving [NII] and [OI] lines as shown in the left panel of the first and the third row. The right panels show the distribution of points

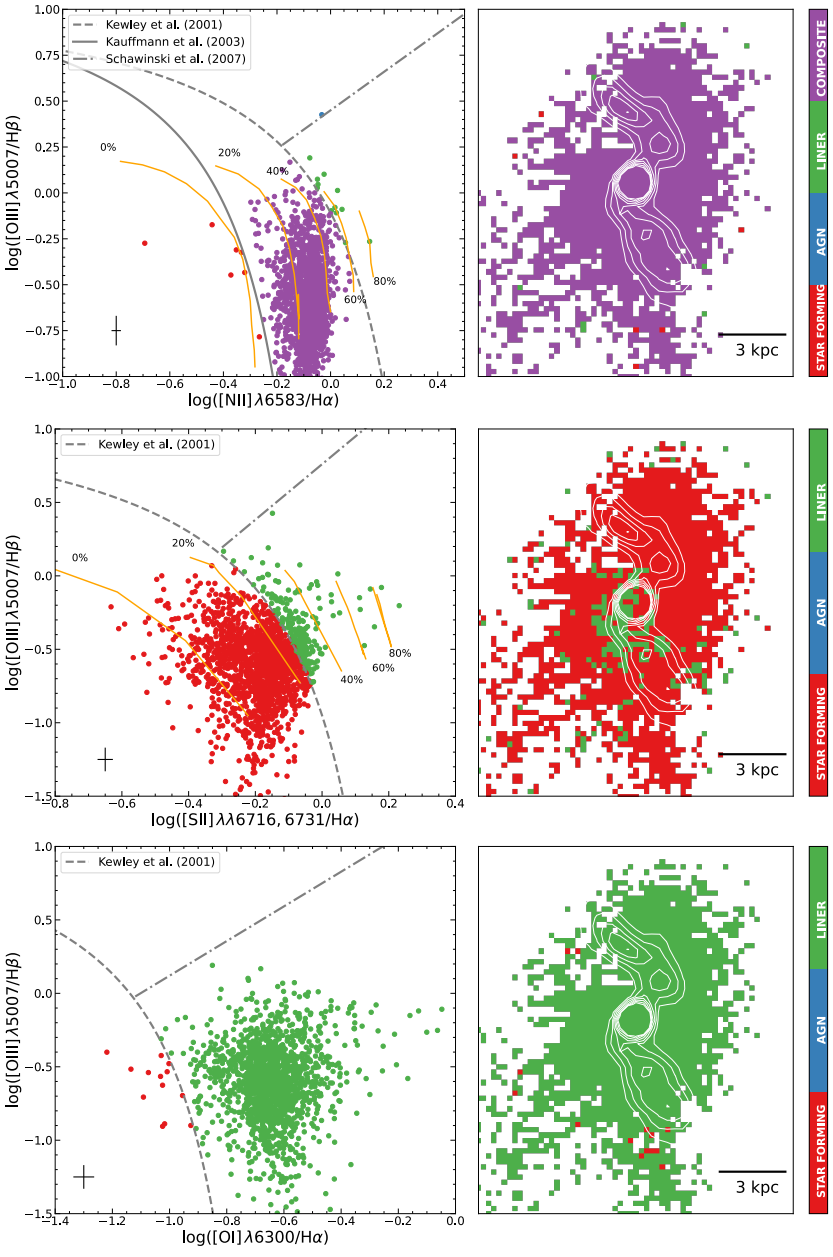
Kewley et al. (2001)
Kauffmann et al. (2003)
Schawinski et al. (2007)
0%
20%
40%
60%
80%
log([OIII]λ5007/Hβ)
log([NII]λ6583/Hα)
log([SII]λλ6716, 6731/Hα)
log([OI]λ6300/Hα)
3 kpc
COMPOSITE
LINER
AGN
STAR FORMING

Figure 3.12 *(previous page)*: The figure displays the emission line diagnostic diagrams. The left panel of the top, middle and bottom row shows the standard BPT diagnostic diagrams using the [OIII]λ5007/Hβ plotted against [NII]λ6583/Hα, [SII]$\lambda\lambda$6716,6731/Hα and [OI]λ6300/Hα line ratios, respectively. The right panel in each row displays the location of spaxels on the galaxy colour-coded by the well-known theoretical classification boundaries in BPT diagrams (Kewley et al., 2001; Kauffmann et al., 2003; Schawinski et al., 2007) shown as grey dashed and dotted lines in the left panels. We also show in the top left panel composite star formation + shock ionization models of McDonald et al. (2012a) as orange curves with the contribution of slow shocks indicated next to the curves. Radio contours at 8 GHz are shown in white. Spaxels with S/N>3 for all lines were included.

in the BPT diagram on the sky. The composite and LINER-like points are uniformly distributed throughout the BCG with no variation, similar to the findings in Abell 2597 (see Tremblay et al., 2018, Fig. 15). However, the BPT diagram involving the [SII] (second row in Fig. 3.12) line shows that the majority of points have star formation as their primary source of ionization. Interestingly, the region surrounding the radio jets shown in the centre has LINER-like ionization (green points). This region is the location where the jet takes a sharp turn by $\sim$90 degrees. Thus it is highly likely that this region is excited by shocks from the radio jets.

The classification in BPT diagrams is not completely unambiguous. Certainly, the situation is more complex and both mechanisms may be acting at the same time with varying relative contributions depending on the location in the galaxy as discussed above. We also plotted the "slow shock + stellar photoionization" models of McDonald et al. (2012a) as orange lines with a varying contribution of slow shocks. The models with 20-40 per cent contribution from shocks represent a majority of the data points well, consistent with results of McDonald et al. (2012a). In the central regions, shocks may be the dominant source contributing to more than 50 per cent. Although these models explain the data reasonably well, other mechanisms such as conduction (Sparks et al., 2012), cosmic ray heating (Ferland et al., 2009; Fabian et al., 2011; Johnstone et al., 2012) and thermal radiation from the cooling flow (Polles et al., 2021) may also contribute.

3.8 Velocity structure function in Abell 1795

It is clear that the radio lobes are interacting and influencing the motion of cold and ionized gases. The radio lobes can drive turbulence in the ISM of the BCG which can produce

local density fluctuations that may seed star formation (Krumholz & McKee, 2005), while simultaneously supporting the gas against gravitational collapse at larger scales (Klessen et al., 2000). One common way to study turbulence is through the velocity structure function (VSF) which is a statistical tool to access the properties of velocity fluctuations. We computed the first order VSF of the Hα and molecular gas by first masking pixels with velocity errors greater than 10 km s^{-1}. We only considered $16'' \times 16''$ region centred on the BCG that covers all molecular gas filaments and inner Hα gas filaments. The velocity maps in Fig. A2 show the location of pixels in the BCG and the different regions used to calculate the VSF. For each velocity map, we compute the VSF by calculating the absolute difference between the velocities of each unique pair of pixels as $|\delta v|$ and the projected separation between those pixels (l). We then binned and averaged the data in groups of l. There is a small difference between the spatial resolutions of the ALMA and MUSE data. We smoothed the ALMA image to the resolution of MUSE and computed the VSF to examine the effect of the resolution. We found that for low-resolution VSF, power at all scales is suppressed marginally (<0.1 dex). The slope of the VSF remains relatively unchanged. We show the VSF with the native resolution for both ALMA and MUSE data.

In the left panel of Figure 3.13, we show the VSF for the molecular gas. The total VSF for the molecular gas peaks and flattens at a pair separation of ∼5 kpc, corresponding to $|\delta v|$ ∼250 km s^{-1}. The peak is most likely caused by the velocity difference between the central clump and the outer edge of the N molecular gas filament, separated by a projected distance of ∼5.5 kpc. The VSF of the total Hα gas in the BCG flattens at ∼ 7 kpc scale corresponding to $|\delta v|$ ∼120 km s^{-1}, as shown in the right panel of Fig. 3.13. The length scale corresponding to the VSF peak may indicate the driving scale of turbulence, which is comparable to the size of the radio lobes. For reference, we show the turbulent velocity of the X-ray gas inferred from X-ray surface brightness fluctuations (Zhuravleva et al., 2014), and turbulent velocity measured by Hitomi for the Perseus cluster (Hitomi Collaboration et al., 2016), respectively, indicated by red and green shaded regions in the right panel. The similarity of turbulent velocities of hot and cold phases suggests that radio-mechanical feedback can drive turbulence in cold filaments.

The Hα VSF has a slope of ∼1/2 until it peaks. At scales between 1 and 3 kpc, the molecular gas has a slope of $\gtrsim$1/2, which is characteristic of supersonic turbulence (Federrath, 2013) mixed with a smooth velocity gradient (Hu et al., 2022a). Above 3 kpc scales, the VSF of individual molecular gas filaments becomes steeper with a slope of 1, indicating that the velocity gradient dominates at these scales. However, for the total molecular gas VSF, the steepening starts at ∼2 kpc with a slope exceeding 1. This is likely due to the N filament intersecting the central gas clump. An extreme example of such steepening would be observed in an ordered motion similar to that in a circumnuclear

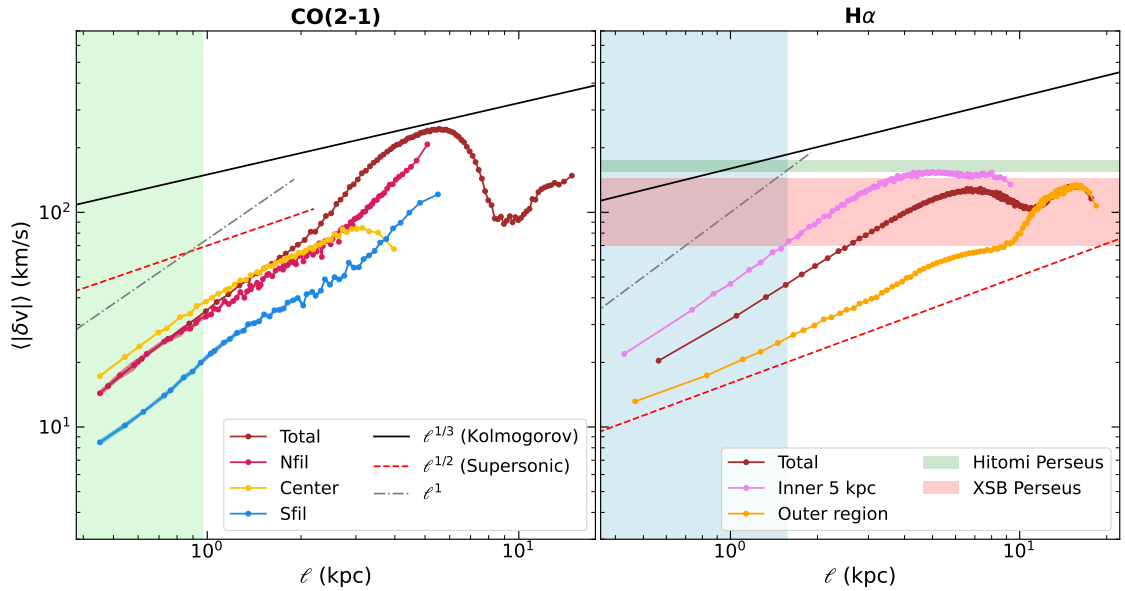

Figure 3.13: The figure shows the velocity structure function of the cold molecular gas (left panel) and warm ionized gas (right panel) traced by ALMA CO(2-1) and MUSE Hα observations, respectively. The thickness of the lines indicates the errors in each bin. To guide the eye, we show the solid black line with a slope of 1/3 for Kolmogorov turbulence, a dashed red line with a steeper slope of 1/2 for supersonic turbulence and a grey dash-dotted line representing a linear relationship between the velocity scale and the spatial scale l. Spatial scales smaller than the spatial resolution of MUSE and ALMA are shown by shaded blue and green vertical regions, respectively. Different regions used in calculating the VSF are shown in Fig. A2.

disk with a radius of a few kpc and velocity shifts of $\sim \pm 100$ km s^{-1}. It can dramatically increase the VSF amplitude at small separation.

The VSF of the filaments have been examined in other BCGs such as Perseus, Abell 2597 and Virgo galaxy cluster (Li et al., 2020). The observed VSF slope of 1/2, characteristic of supersonic turbulence, indicates the turbulent motion of cold gas driven by X-ray cavities or radio lobes. However, analysis of individual filaments in the Perseus cluster, accompanied by numerical simulations (Qiu et al., 2021; Hu et al., 2022a) showed that velocity gradients characterized by a VSF slope of 1 may dominate at scales larger than a few kiloparsecs, especially viewed from an angle close to the flow direction. In the case of Abell 1795, therefore, the VSF is likely dominated by the laminar motion of the filaments and is limited by the observed size of the filaments. The large observed filaments are likely made of smaller unresolved filaments or sheets of molecular gas. Higher resolution observations probing smaller scales are required to probe the nature of turbulence in the molecular phase.

Although the power-law slope of the VSF is often attributed to turbulence, some studies have suggested that it could also be a result of laminar gas flows and large eddies formed in the gas being uplifted behind bubbles blown by radio jets (Zhang et al., 2022). Therefore, caution needs to be taken when interpreting the VSFs. In addition to laminar flows and orientation effects, the presence of magnetic fields can suppress turbulence and steepen the slope of the VSF (Bambic et al., 2018; Mohapatra et al., 2022). Multiple indicators suggest that the cold gas filaments are magnetized as discussed in the paper. Therefore, magnetic fields may also contribute to steepening of the VSF in Abell 1795. Nevertheless, the Hα gas VSF slopes, flattening scale and turbulent velocities point to supersonic turbulence mixed with velocity gradients and orientation effects. Large statistical studies of VSF of many systems sampled by different lines of sight may be able to provide a better understanding of the VSF. Assuming that the VSF is characterised by supersonic turbulence, and if it cascades down to the scales of giant molecular clouds (GMCs), the star formation efficiency is expected to follow the KS-relation (Krumholz & McKee, 2005). We are unable to probe the turbulence at the scales of GMCs. However, simulations suggest that the star formation can also generate supersonic turbulence in GMCs on sub-pc scales and suppress its efficiency over time (Hu et al., 2022b). Thus we tentatively find that on a timescale of a few million years, radio jets can drive supersonic turbulence which can trigger star formation locally with lower efficiency than starbursts, but comparable to or higher than star formation in galactic disks.

3.9 Conclusions

We studied the interaction between radio jets and the ISM and the nature of radio-jet triggered star formation in Abell 1795 by combing VLT XSHOOTER, MUSE, ALMA and *HST* data. We determined the star formation rate using the UV *HST* images of the BCG and star formation efficiency by combining it with the ALMA molecular gas data. Using the nebular gas emission line ratios derived from MUSE IFU data, we were able to determine the level of extinction, electron density, excitation level and ionization mechanism in the BCG. We also detected a shock-like feature ∼2 kpc N-NE of the nucleus. The results are summarised below.

• We measured extinction corrected ongoing UV star formation rate of 9.3 $M_\odot$ yr^{-1} in the BCG. The star formation rate has a low efficiency with an average depletion time of ∼1 Gyr. However, the efficiency of star formation is location dependant and it is even lower in the region of interaction between radio jets and the gas. The offset between star formation and the molecular gas in the S filament suggests that the stars have decoupled from the molecular gas and are moving in the gravitational potential of the BCG while the gas motion is being continually affected by the radio jets and the surrounding medium.

• The ionized gas traced by the Hα emission line is more extended than the molecular gas. The BCG has a total Hα luminosity of $(4.180\pm0.002)\times10^{41}$ erg s^{-1}, corresponding to ionized gas mass of $(1.640\pm0.001)\times10^7$ $M_\odot$. The velocity map of Hα reveals a 'V'-shaped wing of redshifted gas wrapped around the southern radio lobe with velocities of ∼100 km s^{-1}. In other parts of the BCG, the ionized gas is blueshifted to velocities lying between −100 to −370 km s^{-1}, similar to the velocities of molecular gas, suggesting that the two gas phases are co-moving. The FWHM map reveals an arc of high FWHM with values reaching ∼700 km s^{-1} to the N-NE of the nucleus. Other areas of the BCG have FWHM of ∼250 km s^{-1}, roughly 2-3 times the FWHM of the molecular gas.

• We measured an average extinction of 0.6 in the star-forming filaments in the BCG using H Balmer decrement. The electron density in the ISM traced by [SII] line ratios in the BCG are ∼ 100 cm^{-3} or lower. Electron densities in the region cospatial with the high FWHM arc are 4 times higher compared to surrounding regions which could indicate a weak shock perhaps driven by radio jets or the peculiar motion of the BCG. The standard nebular emission line diagnostic diagrams classifications are ambiguous, however, they are represented by models of gas ionization with star formation and a small contribution from slow shocks.

• We also computed the VSF of the molecular and ionized gases. The molecular gas VSF is dominated by the size of the filaments and laminar motion with slopes of $\sim$1. The Hα VSF slopes of $\gtrsim$1/2, turbulent velocities of $\sim$120 km s^{-1} and flattening scale of $\sim$7 kpc similar to the size of radio lobes tentatively indicate that radio-mechanical feedback can drive supersonic turbulence in the ionized gas.

• The XSHOOTER spectrum of the south star-forming filament is dominated by strong nebular emission lines and older stars in the galaxy making it unfeasible to determine the velocity of young stars. We did not detect NIR H_2 emission lines tracing warm molecular gas at a level of $\sim 1 \times 10^{-16}$ erg s^{-1} cm^{-2} Å^{-1} in the NIR XSHOOTER spectrum of the S filament.

We presented a detailed analysis of extended radio-jet-triggered star formation. Abell 1795 presents an excellent example of both positive and negative radio-mechanical feedback, where the radio jets are heating the hot atmosphere of the BCG and driving gas flows while triggering star formation in the outflowing gas. Although determining the velocities of young stellar populations in the star-forming filaments is unfeasible in this case, the stars formed in outflowing gas are expected to have radial orbits and they could populate outer regions of galaxies (Ishibashi & Fabian, 2012). Positive feedback is expected to be more common at high redshift when gas densities were higher and AGN feedback was dominant. Some models predict that star formation triggered by positive feedback contributes substantially to star formation rates in distant galaxies (Silk, 2013) and it may be necessary to explain the $M_{\rm BH} - \sigma$ relation observed in galaxies (Silk & Nusser, 2010). This object represents an excellent example of star formation at the interface of radio jet/gas interaction and is helpful in understanding the positive feedback of the radio jets in galaxies in the distant Universe.

Chapter 4

Stimulated feedback by uplift in massive cool-core central galaxies

In previous chapters, we showed how radio mode feedback can drive outflows of molecular gas in BCGs which can potentially suppress star formation, while simultaneously triggering star formation on short timescales. It shows that the nature of radio mode feedback is more complex. However, how the molecular gas flows are powered and the mechanical feedback energy is coupled to the cold gas is not yet clear. Several models have been proposed to address this question and to explain the formation, morphology and kinematics of large amounts of cold gas found in BCGs. In this chapter, I study the stimulated feedback mechanism in detail in a sample of galaxy clusters using X-ray observations.

This chapter contains original research. I analyzed all X-ray data presented in this chapter and wrote the chapter. My supervisor Prof. Brian McNamara provided comments that improved the chapter.

4.1 Introduction

The centres of galaxy clusters host some of the most powerful active galactic nuclei (AGN) in the local Universe. They are dynamic and the galaxies hosting them are some of the most massive elliptical galaxies. Energetic feedback from the AGN is thought to be the key to regulating the growth of the brightest cluster galaxies (BCGs), and perhaps other galaxies hosting AGN. The environment around BCGs is surrounded by hot X-ray-emitting gas. The strong X-ray emission suggests that the gas is cooling radiatively. If cooling is

unimpeded, it should form large amounts of molecular gas. However, the molecular gas masses in BCGs are much lower than what is expected from classical cooling of the ICM, and the observed star formation rates are low. Atomic and molecular outflows powered by radio jets are responsible in whole or part for the lack of significant levels of star formation.

The recent high-resolution Atacama Large Millimeter Array (ALMA) observations of BCGs have revealed that the molecular gas is predominantly observed in filament-like structures trailing behind buoyantly rising radio bubbles. It is either lifted from the centres of galaxy clusters or cooled in situ from the hot gas. Lifting the molecular gas clouds by radio jets is difficult because of the several decades of difference in the density of gas and jet material, a low cross-section of jets and the destruction timescales of molecular clouds in the hot wind may be small compared to their dynamical time. It is difficult to lift $\sim 10^{10}$ $M_{\odot}$ of molecular gas for cavities. The more likely scenario is that the molecular gas condenses out of the hot gas when the ratio of its cooling time to local infall time falls below 1. *Chandra* observations showed that cool-core clusters shine in Hα and CO emission when the cooling time of the hot gas falls below 5×10^8 yr or central entropy falls below 30 KeV cm^2 (Cavagnolo et al., 2008; Pulido et al., 2018). It is argued that runaway cooling happens when $t_{\rm cool}/t_{\rm ff}$ ratio of the hot gas falls below $\sim$ 10 (Voit & Donahue, 2015; Pulido et al., 2018). However, there are some exceptions. Recently, Martz et al. (2020) showed that central atmospheres of Abell 2029, Abell 2151, RBS0540 and RBS0533, dubbed "spoiler clusters", have short central cooling times of less than a few Gyr and low entropies, yet these systems are devoid of nebular emission or molecular gas. The X-ray atmospheres of those BCGs are relaxed and do not show any sign of disturbance or bubbles, suggesting that the cooling time and entropy cutoffs are not the only things promoting the cooling of the gas.

McNamara et al. (2016) proposed a stimulated feedback model where the low entropy gas in central regions is uplifted by cavities to an altitude where its cooling time is comparable to or less than the time it takes to fall back to its initial position. It is this gas that cools and forms the cold gas filaments observed in BCGs of cool-core clusters. This mechanism naturally explains the lack of cold gas in spoiler clusters. The feedback mechanisms in those clusters has failed to blow cavities that lift low entropy gas, facilitating cooling. Although promising, detailed studies are required to assess the viability of this mechanism to explain the observed levels of molecular gas in galaxy clusters.

The uplifted gas can cool through several channels. The most common way is radiative cooling. However, purely radiative cooling appears inefficient below the energies of $\sim$ 1–2 keV. The soft X-ray flux from gas cooling below 1–2 keV is lower than expected in many clusters (Fabian et al., 2002). If the cool X-ray gas mixes with the surrounding cooler gas ($\sim 10^5$ K), it may cool rapidly and radiate in the UV and optical emission. It can then be

reprocessed by cooler gas into infrared emission. Further, if dust is present, it can boost cooling of the gas. The radiation can occur through reradiation of UV or optical emission, or during sputtering of dust. The spatial correlation between soft X-ray and optical Hα filaments suggest this mechanism.

In this chapter, we study the stimulated feedback mechanism in detail in a sample of 24 cool-core galaxy clusters using *Chandra* X-ray observations. Using molecular gas, X-ray and Hα gas data, we study whether bulk gas uplift by cavities is a viable feedback mechanism.

Throughout this chapter, we have assumed a standard ΛCDM cosmology with $\Omega_{\rm m} = 0.3$, $\Omega_\Lambda = 0.7$, and $\rm H_0 = 70$ km s^{-1} Mpc^{-1}.

4.2 Sample selection

Our aim is to study the inner (<30 kpc) regions of galaxy clusters to test the stimulated feedback mechanism. We focus on the cool-core clusters in which multiphase gas has been detected. We selected a sample of 24 cool-core clusters which are observed with *Chandra*, in which their cooling time within central 10 kpc is less than 5×10^9 years. All clusters have more than 80 ks of *Chandra* observations, providing at least one annular bin within central 10 kpc with sufficient photon counts for spectral extraction. Cold molecular gas has been detected in 15 clusters with 3 more having upper limits and 20 clusters have Hα detection. We also included two clusters in which the central cooling time is less than 10^9 years, but they do not have atomic or molecular gas detection. Basic properties of the clusters in the sample are presented in table 4.2.

4.3 Data collection and Reduction

4.3.1 X-ray data

The archival *Chandra* data for clusters was obtained from the Chandra Data Archive (CDA). Data were reduced using CIAO version 4.13 with the CalDB version 4.9.5. Level-1 events were reprocessed using the CHANDRA_REPRO script. The VFAINT mode was turned on when observations were taken in that mode. Events with bad grades were removed and background light curves were extracted from level-2 event files on a complimentary chip to the one that has most of the cluster emission. The light curves were

Table 4.2.

Cluster	Redshift	RA	DEC	Exposure (ks)	Log Hα (erg s^{-1})	M_{mol} ($M_\odot$)	Cavities
A1795	0.063001	13:48:52.52	26:35:36.30	717.2	41.503	$(3.3\pm0.2)\times10^9$	yes
A2052	0.0355	15:16:44.484	+07:01:17.86	645.0	40.768	$(2.7\pm0.4)\times10^8$	yes
A2597	0.0821	23:25:19.72	−12:07:27.62	626.4	41.751	$(3.6\pm0.1)\times10^9$	yes
MS0735+7421	0.216	07:41:44.21	74:14:38.31	476.7	42.113	$<10^9$	yes
A1835	0.2532	14:01:02.08	02:52:42.99	252.7	42.235	$(4.9\pm0.3)\times10^{10}$	yes
A1664	0.128	13:03:42.521	−24:14:42.81	245.5	41.818	$(1.1\pm0.1)\times10^{10}$	yes
MACS1347-11	0.451	13:47:30.58	11:45:09.21	233.8	-	-	no
Hydra-A	0.055	09:18:05.651	−12:05:43.99	215.3	41.153	$(5.4\pm0.2)\times10^9$	yes
ZwCl3146	0.291	10:23:39.609	+04:11:11.68	206.0	42.657	$(5.6\pm0.2)\times10^{10}$	yes
A85	0.0551	00:41:50.48	−09:18:11.82	195.2	40.756	$(4.5\pm2.5)\times10^8$	yes
RXJ1504.1-0248	0.215	15:04:07.519	−02:48:16.65	161.7	42.723	$(1.9\pm0.1)\times10^{10}$	yes
A133	0.0566	01:02:41.59	−21:52:53.65	154.3	39.924	-	yes
PKS0745-191	0.1028	07:47:31.291	−19:17:40.02	151.2	42.243	$(4.9\pm0.3)\times10^9$	yes
IC1262	0.0331	17:33:01.973	+43:45:35.13	144.4	39.038	-	yes
A262	0.017	01:52:46.482	+36:09:06.53	139.4	39.497	$(3.4\pm0.1)\times10^8$	yes
A2626	0.0553	23:36:30.43	21:08:47.23	135.6	39.707	$< 7.6\times10^8$	yes
MACS1423+24	0.543	14:23:47.87	24:04:42.50	134.1	43.010	-	yes
Zw2701	0.215	09:52:49.16	51:53:05.58	122.7	40.737	-	yes
A2199	0.0302	16:28:38.245	+39:33:04.21	119.9	40.132	$< 2.6\times10^8$	yes
Zw7160	0.2578	14:57:15.10	22:20:33.89	108.8	41.514	$(5.8\pm2.5)\times10^{10}$	no
A2029	0.0773	15:10:56.08	05:44:41.05	107.6	<39.643	$< 1.7\times10^9$	no
AS1101	0.058	23:13:58.693	−42:43:38.58	97.7	41.158	$(1.2\pm0.1)\times10^9$	yes
NGC5044	0.009	13:15:23.969	−16:23:08.00	82.7	39.836	$(3.6\pm0.3)\times10^7$	yes
Phoenix	0.596	23:44:43.90	−42:43:12.53	551.5	-	$(2.1\pm0.3)\times10^{10}$	yes

filtered using the LC_CLEAN routine in SHERPA to remove time intervals affected by background flares.

Blank-sky backgrounds were extracted from CalDB for each observation, reprocessed identically to the event files and normalized to a 9.5–12.0 keV count rate in each observation. Both reprocessed event files and blank-sky observations were reprojected to the observation with the longest clean exposure time. Images were created in the 0.5–7 keV energy range for each observation ID (ObsID). Images were summed after subtracting the background. A point spread function (PSF) map of the observation with the longest exposure was created. The summed image along with the PSF map was used to detect point sources using the WAVDETECT algorithm in CIAO Freeman et al. (2002). The point sources were visually inspected, and if necessary, corrected in DS9 and then excluded from further analysis.

Spectral extraction

We extracted spectra in the 0.5–7 keV range from annular regions selected in such a way that each annulus has at least 3000 net counts. This decision was made to ensure that the deprojected profiles have sufficient net counts for successful spectrum fitting. Although there is no hard limit to the minimum number of counts, previous studies have shown that a minimum of 3000 counts per bin lead to sufficient counts in the deprojected spectra for successful fitting. For RXCJ1539, a minimum of 2000 counts were chosen to have a central bin as close to 10 kpc as possible due to shallower observation. The radius of the innermost annulus was set to zero for most of the clusters. Whenever a bright point source was present in the centre of the brightest cluster galaxy (BCG), it was excluded from the innermost annulus. The centre of the BCG was chosen as the centre for all annuli in each cluster following Hogan et al. (2017). In most clusters at least one bin containing $\gtrsim$3000 net counts within central 10 kpc were present.

Exposure maps were created to correct the spectra for the lost area due to chip gaps and point source subtraction. The CIAO tasks MKACISRMF and MKWAFR were used to create weighted individual redistribution matrix files (RMFs) and weighted auxiliary response files (ARFs) for each spectrum. The spectra were binned to ensure 30 counts per channel. For RXCJ1539, they were binned with 15 counts per channel in order to have a sufficient number of points for successful modelling. All spectra were extracted and treated separately for each ObsID. Lastly, the spectra were deprojected using the routine DSDEPROJ[1] described in Sanders & Fabian (2007) and Russell et al. (2008).

[1] https://github.com/jeremysanders/dsdeproj

4.3.2 Molecular and Hα gas data

The majority of clusters in our sample are observed with ALMA. The molecular gas properties in these clusters have been discussed in detail (see for example, Russell et al., 2019; Olivares et al., 2019; Tamhane et al., 2022, and references therein). For clusters observed with ALMA, we used their molecular gas masses and published in Tamhane et al. (2022) and Russell et al. (2019). The molecular gas masses for the remaining clusters were obtained from Pulido et al. (2018) and Edge (2001). The Hα luminosities of these clusters were obtained from Hamer et al. (2016) and Pulido et al. (2018). The extent of the Hα emission was taken from Hamer et al. (2016) and Olivares et al. (2019).

4.4 Results

The extracted spectra and corresponding RMF and ARF files were loaded in XSPEC version 12.10.1f Arnaud (1996) for spectral fitting. For every cluster, the spectra for all ObsIDs were loaded simultaneously for each annulus. We initially calculated projected profiles. The spectra were modelled with the absorbed single temperature (PHABS*APEC) model. The relative abundances were set to the values in Anders & Grevesse (1989) and metallicities were allowed to vary. The hydrogen column density N_H was frozen to the values taken from Kalberla et al. (2005). The APEC model normalization was used to calculate projected electron number densities (n_e) as follows:

$$n_e = D_A(1+z)10^7\sqrt{\frac{N4\pi 1.2}{V}} \tag{4.1}$$

where N is the model normalization, D_A is the angular diameter distance to the source in cm, z is the redshift of the source and V is the volume of the spherical shell bounded by the inner and outer projected radius of the annulus in cm^{-3}. The factor of 1.2 arises from the relative abundances of electron to hydrogen ion number densities, $n_e = 1.2n_H$ (Anders & Grevesse, 1989). Assuming n_e and n_H to be constant in each spherical shell, cooling times were calculated using

$$t_{cool} = \frac{3P}{2n_e n_H \Lambda(Z,T)} = \frac{3PV}{2L_X} \tag{4.2}$$

where P is the pressure calculated as $P = 2n_e k_B T$, $\Lambda(Z,T)$ is the cooling function as a function of metallicity Z and temperature T and L_X is the unabsorbed bolometric X-ray

luminosity obtained by integrating the fitted model between 0.1 to 100 keV by multiplying it by CFLUX model in XSPEC. The hot gas mass in each shell was calculated using $M_{\rm gas} = PV\mu m_{\rm p}/k_{\rm B}T$, assuming that the pressure and density in each shell are constant, where μ is mean molecular gas mass of the ICM and $m_{\rm p}$ is the mass of a proton.

4.4.1 Cavities

X-ray cavities are detected in 21 clusters in this sample. Cavities in many BCGs have been studied in the literature. We adopted cavity shapes from the literature for most of the clusters and visually inspect the clusters for more cavities or to measure their shape where only cavity distance was reported. We measured the shape of the outer cavities in A1795, A1664 and two cavities in AS1101, using the unsharp masking technique on their 0.5–7 keV band *Chandra* X-ray images. Cavity sizes and positions were determined by assuming that the cavity extends to the inner edge of any surrounding bright emission. Cavity volumes were calculated using the geometric mean of oblate and prolate volumes as $V = 4/3\pi(ab)^{3/2}$, where a and b are projected lengths of semi-major and semi-minor axes of cavities, respectively. The gas mass displaced by cavities ($\rm M_{gas,disp}$) was calculated assuming cavities are empty regions devoid of any gas and multiplying the density of the ambient medium at the radius of the cavity by cavity volume. Thus, $M_{\rm gas,disp} = 1.2n_e(R)m_{\rm p}V$, where $n_e(R)$ is the electron density of the ICM at the distance (R) of the cavity, $m_{\rm p}$ is the mass of a proton and V is the cavity volume. Several clusters such as A2597, A1664, and A1795 have more than two cavities indicating multiple AGN outbursts.

Cluster	a (kpc)	b (kpc)	R (kpc)	$M_{gas,disp}$ ($\times 10^8$ $M_\odot$)	t_{age} ($\times 10^7$ yr)	Reference
A85	8.1	5.4	17.1	8.2	2.5	Shin et al. (2016)
A133	9.8	5.2	28.1	6.6	5.1	Bîrzan et al. (2004)
A133	9.8	5.7	32.7	6.7	6.0	Bîrzan et al. (2004)
A262	2.6	2.6	6.2	0.6	1.4	Bîrzan et al. (2004)
A262	3.3	2.6	6.7	0.8	1.5	Bîrzan et al. (2004)
A1664	4.6	4.6	4.6	8.5	0.5	Calzadilla et al. (2019)
A1664	4.6	4.6	6.7	8.2	0.9	Calzadilla et al. (2019)
A1664	10.1	7.5	15.0	32.6	1.9	This work*
A1664	9.8	7.2	23.3	20.1	3.5	This work*
A1795	10.0	10.0	44.0	26.6	6.7	Kokotanekov et al. (2018)
A1795	23.0	7.0	16.0	88.9	1.8	Kokotanekov et al. (2018)
A1795	12.3	8.3	37.6	30.0	5.6	This work*
A1835	15.5	11.6	23.3	237.3	1.8	McNamara et al. (2006)
A1835	13.6	9.7	16.6	171.4	1.2	McNamara et al. (2006)
A2052	6.5	6.0	6.7	7.80	1.1	Bîrzan et al. (2004)
A2052	10.7	7.8	11.2	24.4	1.6	Bîrzan et al. (2004)
A2199	6.5	6.5	18.9	5.47	3.2	Bîrzan et al. (2004)
A2199	6.2	3.5	21.2	1.9	4.4	Bîrzan et al. (2004)
A2597	7.3	6.0	21.7	13.2	3.8	Shin et al. (2016)
A2597	3.1	2.9	9.4	2.1	2.0	Shin et al. (2016)
A2597	8.7	6.6	21.6	20.0	3.5	Shin et al. (2016)
A2597	5.1	3.0	20.6	2.9	4.6	Shin et al. (2016)
A2597	14.0	9.6	17.4	86.4	2.2	Shin et al. (2016)
A2626	19.9	12.4	18.1	76.2	1.8	Shin et al. (2016)
AS1101	4.6	3.5	5.8	2.8	0.9	This work*
AS1101	4.6	3.5	11.2	3.3	2.0	This work*
Hydra-A	16.4	11.2	23.8	72.1	3.0	Shin et al. (2016)
Hydra-A	15.3	9.6	24.8	50.0	3.3	Shin et al. (2016)
IC1262	2.2	1.5	6.5	1.2	1.4	Pandge et al. (2019)
IC1262	4.0	2.0	6.1	1.1	2.3	Pandge et al. (2019)
MACS1423+24	27.1	12.7	36.1	378.2	2.7	Shin et al. (2016)
MACS1423+24	9.4	9.4	15.8	97.3	1.4	Diehl et al. (2008)
MACS1423+24	9.4	9.4	16.7	94.0	1.5	Diehl et al. (2008)
MS0735+7421	109.0	106.0	150.0	7307.4	9.2	Vantyghem et al. (2014)
MS0735+7421	120.0	100.0	186.0	6212.4	11.6	Vantyghem et al. (2014)

NGC5044	3.1	1.7	6.1	0.3	1.3	Gastaldello et al. (2009)
NGC5044	3.1	1.7	6.1	0.3	1.3	Gastaldello et al. (2009)
Phoenix	11.3	8.6	17.3	245.8	1.3	McDonald et al. (2019)
Phoenix	14.6	8.6	17.3	361.0	1.2	McDonald et al. (2019)
PKS0745	9.9	8.8	18.4	71.7	2.0	Shin et al. (2016)
PKS0745	11.6	8.5	9.3	140.3	0.8	Shin et al. (2016)
RXCJ1504	13.6	4.5	11.9	100.6	1.1	Shin et al. (2016)
RXCJ1504	36.6	15.6	23.5	2069.0	1.5	Shin et al. (2016)
Zw2701	43.5	43.5	54.1	1653.9	3.4	Diehl et al. (2008)
Zw2701	36.7	36.7	48.6	1083.0	3.2	Diehl et al. (2008)
ZwCl3146	33.2	33.2	39.8	1829.4	2.6	Diehl et al. (2008)
ZwCl3146	33.0	33.0	59.1	1284.2	4.2	Diehl et al. (2008)

Table 4.3: Properties of cavities detected in clusters in our sample.
*: Only distances for these cavities were reported in the literature. Therefore, we measured their shapes and other properties as described in section 4.4.1.

The ages of cavities were determined by their buoyancy time. Assuming cavities are like bubbles in dense atmospheres rising buoyantly at their terminal velocities, the ages of the cavities are estimated as the time it takes them to reach their observed height from the centre of the BCG while travelling at their terminal velocities. The terminal velocities of a cavity $\nu_t \sim (2gV/SC)^{1/2}$, where V is the volume of the cavity estimated as $S = \pi(ab)$, S is the cross-section of the cavity, and $C = 0.75$ is the drag coefficient. The gravitational accelerations (g) were calculated by interpolating the gravitation acceleration profiles for each cluster taken from Hogan et al. (2017), at the observed distance of cavities. The cavity age is then given by

$$t_{\rm buoy} = R/\nu_t \sim R\sqrt{SC/2gV} \tag{4.3}$$

where R is the projected distance of the cavity from the centre of the BCG. Properties of cavities are provided in table 4.3.

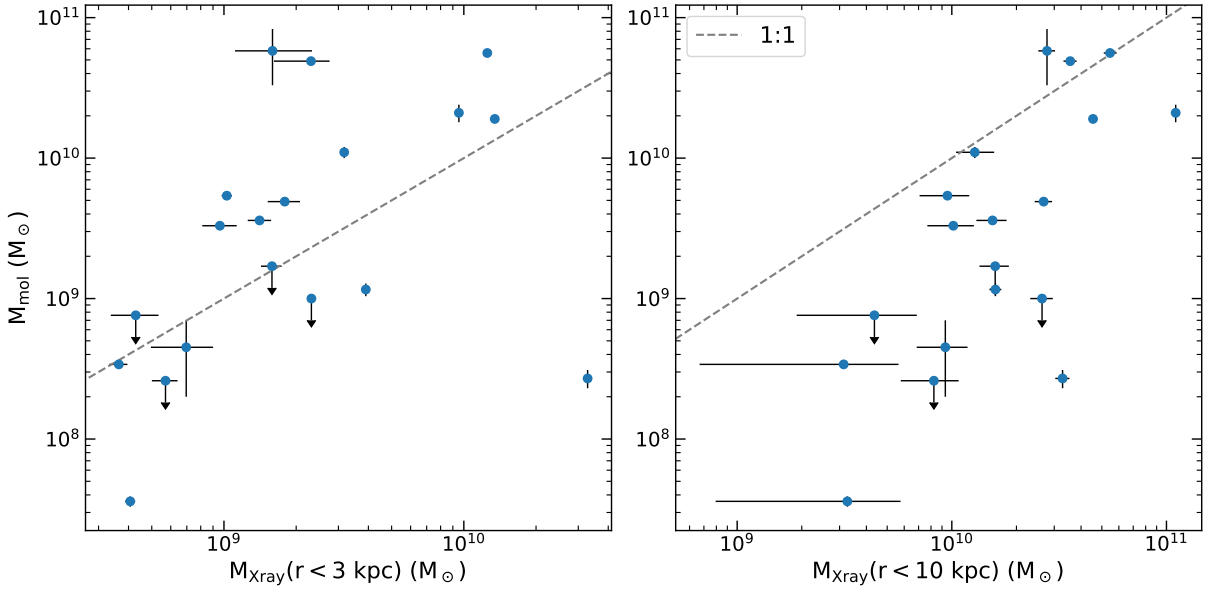

Figure 4.1: The relationship between the mass of the low entropy gas in the inner 3 kpc (left panel) and 10 kpc (right panel) of BCGs and the total molecular gas mass observed in BCGs. The grey dashed line shows a 1:1 relationship. Several BCGs have enough low entropy gas in the inner regions which can be uplifted by cavities to high altitudes.

4.5 Discussion

4.5.1 Is there enough gas in central regions?

The stimulated feedback mechanism proposes that the low entropy gas in central regions of galaxy clusters is raised by cavities to higher altitudes such that it has enough time to cool before it falls back to the centre. If cavities are able to lift gas in bulk in their wakes, there has to be a sufficiently large reservoir of gas to be uplifted. We chose radii of 3 and 10 kpc which is sufficiently small such that the gas enclosed within them has sufficiently low cooling time (10^9 yr). We interpolated (extrapolated) deprojected gas mass profiles to those radii for clusters in which the radius of the smallest spectral extraction annulus was less than (greater than) the required radius to estimate the amount of gas enclosed within that region. We then compared it with the total molecular gas mass in BCGs.

Figure 4.1 shows their relationship. The left and right panels show relationships at 3 and 10 kpc, respectively. The majority of clusters have more molecular gas than the

amount of low entropy gas within 3 kpc. In some clusters, the amount of hot gas within 3 kpc is comparable to or exceeds the detected molecular gas mass. In these clusters, all the gas within a central few kpc would have to be uplifted to cool and form the observed levels of molecular gas mass, which obviously has not happened. Thus, an uplift of gas within such small radii alone is not viable in most clusters. However, most of the BCGs have more than enough hot gas within the inner 10 kpc (see right panel) to cool to the observed levels of the molecular gas mass. In A1835, ZwCl3146 and Zw7160, the molecular gas mass exceeds the amount of hot gas in the inner 10 kpc region. These BCGs could have accumulated cold gas from previous feedback cycles or other channels promoting gas condensation are more efficient or a combination of both. However, the hot gas mass enclosed within 20 kpc exceeds the cold gas in these clusters.

4.5.2 How much gas can cavities lift?

There is a sufficient amount of hot gas in the central regions of the majority of clusters. However, cavities blown by radio jets should be able to lift a sufficient amount of gas in their wake efficiently to match the observed levels of molecular gas. Cavities lift gas behind them as they rise buoyantly within the cluster atmosphere. The amount of gas they can lift is limited by the amount of weight they displace as per Archimedes's' principle, thus, they cannot lift more gas than the amount of gas they displace (McNamara et al., 2016). We compared the mass of hot gas displaced by cavities to the total amount of molecular gas in galaxy clusters. We detected at least 1 or more cavities in 18 clusters in our sample. The details of cavity properties and displaced gas masses are provided in table 4.3 and discussed in section 4.4.1.

In Fig. 4.2, we show the comparison between the total gas mass displaced by all detected cavities in each BCG and the total molecular gas mass. In many clusters, cavities have displaced up to an order of magnitude more hot gas than the observed molecular gas mass. Thus, cavities can lift a sufficient amount of low entropy gas which can cool and form cold molecular gas. The lifted low-entropy gas will cool in situ, leading to condensation in form of filaments, evidence of which is observed in several BCGs (see Russell et al., 2019). In A262, A1664, A1835 and AS1101, there is more molecular gas than the amount of gas cavities have displaced. In some clusters, multiple generations of cavities are detected and their masses are summed. A single episode of AGN activity is generally unable to lift a sufficient amount of gas to high altitudes. In many clusters, two successive generations of cavities can uplift enough gas which can cool to form observed levels of molecular gas.

Both molecular gas and displaced gas masses have large uncertainties. The uncertainty in the displaced gas masses comes from the estimation of cavity volume. In some clusters,

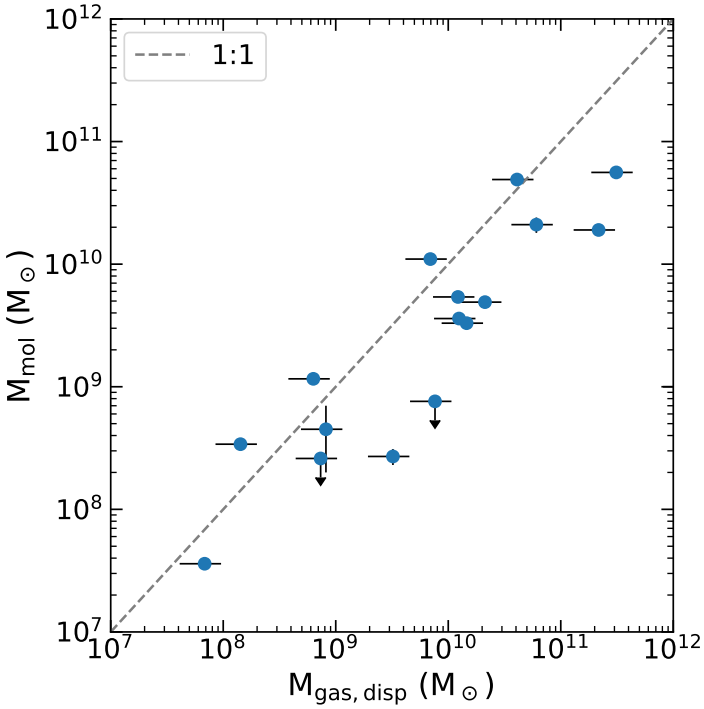

Figure 4.2: The relationship between the total molecular gas mass in BCGs and the total maximum displaced gas mass by cavities. In many clusters, the observed cavities can or have displaced enough hot gas to lift a comparable amount of low entropy gas from the inner regions.

estimating the exact boundary of a cavity is difficult. Some cavities may have collapsed. Also, the projected shape could under or overestimate the true cavity volume. The molecular gas masses can be overestimated if the CO-to-H_2 conversion factor (X_{CO}) is smaller. The typical X_{CO} has an uncertainty of a factor of a few.

Given the uncertainties, we conclude that the displaced gas masses and molecular gas masses are approximately comparable with each other. Larger cavities uplift and cool more gas as shown in table 4.3. It is consistent with the stimulated feedback model. However, multiple generations of cavities are required to cool a sufficient amount of gas in most of the cases, consistent with what some of the previous studies have found (see for eg. Russell et al., 2017b; McNamara et al., 2014).

4.5.3 Cooling of uplifted gas

Next, we study the cooling of uplifted gas. The most common cooling mechanism in the ICM of clusters is radiative cooling through free-free collisions that produce bremsstrahlung emission above 10^7 K and collisionally excited line emission at lower temperatures. However, the gas can also cool non-radiatively through mixing with pre-existing warm and cold gas and through sputtering of dust if the dust is present in the ICM within the cooling radii. The following sections describe how we estimate gas cooling rates.

Radiative cooling rate

The classical radiative cooling rate is simply calculated as the ratio of gas mass to its cooling time in each radius given as $\dot{M}_{\rm Xray} = M_{\rm gas}(r < r_c)/t_{\rm cool}$, where the cooling time $t_{\rm cool}$ is calculated using equation 4.2 and r_c is the cooling radius. Typically, r_c is chosen to be the radius at which the cooling time of the cluster is equal to its age. Some studies adopt $t_{\rm cool}$ values of 7 Gyr (Fabian, 2012) or 3 Gyr (McDonald et al., 2018). As we are interested in the uplift of gas within central 10 kpc, we estimated radiative cooling rates for r_c of 10 kpc.

Non-radiative cooling rate

Many clusters have low X-ray luminosity below 2 keV expected from cooling flow models with purely radiative cooling (Peterson et al., 2001; Tamura et al., 2001a). Fabian et al. (2002) proposed that gas at temperatures less than 1–2 keV may cool through mixing with cooler gas and emit at optical to UV frequencies. We estimate an upper limit for cooling through mixing using Hα luminosities and the following equation from Liu et al. (2019):

$$\dot{M}_{\rm H_\alpha} = 0.99\Big(\frac{L_{\rm H\alpha}}{10^{40}\,{\rm erg\,s^{-1}}}\Big)\Big(\frac{kT}{1\,{\rm keV}}\Big)^{-1}\ {\rm M_\odot\ yr^{-1}}, \tag{4.4}$$

where $L_{\rm H\alpha}$ is Hα luminosity of the gas and kT is 0.7 keV. This cooling rate is an upper limit as it ignores the work done on the cooling gas and assumes that the gas cools instantaneously. Many BCGs have ongoing star formation which also contributes to the observed Hα luminosities. Whether it accounts for all the line emissions is not clear.

Some of the ultraviolet and optical emissions released by the mixing of gases can be absorbed and re-radiated by dust in the IR. Also, if the dust becomes mixed with the hot

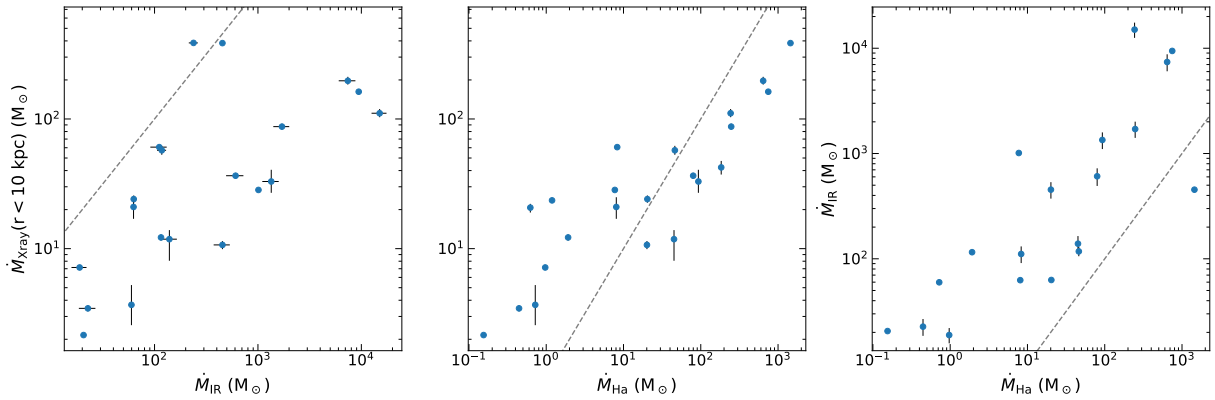

Figure 4.3: Comparison of gas cooling rates. The left and right panels show the relationship between the radiative cooling rate derived from X-ray luminosity with IR and nebular cooling rates, respectively.

gas, its sputtering can further boost gas cooling. The infrared cooling rate is estimated using the following relation:

$$\dot{M}_{\rm IR} = \frac{2}{5}\frac{L\mu m_{\rm p}}{kT}, \tag{4.5}$$

where L is the total IR luminosity, μ is the mean molecular weight $\sim$0.6 and $m_{\rm p}$ is the mass of hydrogen atom, k is the Boltzmann's constant and T is the temperature of the cooling plasma which is taken to be 1 keV. We used the method described in Donahue et al. (2011) to estimate the total IR luminosity as $L_{\rm TIR} = 1.559\,L_{24} + 2.1156\,L_{70}$, where L_{24} and $L_{70} = \nu L_{\nu}$ at 24 μm and 70 μm, respectively. We obtained 24 and 70 μm IRAC fluxes for the cluster in our sample from NED[2]. When 24 μm fluxes were available, but 70 μm IRAC fluxes were missing, we used 70 μm flux from Herschel PACS. We found infrared photometric fluxes (F_{ν}) for 11 clusters in this sample and upper limits for 4 clusters. The fluxes were converted to luminosities using $L_{\nu} = 4\pi D_L^2 F_{\nu}$, where D_L is the luminosity distance.

All cooling rates are reported in table 4.4. In Fig. 4.3, we show the comparison between radiative ($\dot{M}_{\rm Xray}$) and non-radiative gas cooling rates. In most BCGs, where IR luminosities are available, the IR cooling rate ($\dot{M}_{\rm IR}$) far exceeds the radiative cooling rate and the rate of gas cooling through mixing ($\dot{M}_{\rm Ha}$) estimated from nebular luminosities (see left and right panels). However, some of the IR emissions could originate from the central AGN or the reprocessed stellar radiation. How much of it comes from mixing or dust sputtering is

[2] https://ned.ipac.caltech.edu/

BCG	Cooling rate ($\dot{M}$)			$L_{\rm TIR}$
	Radiative (R<10 kpc) ($M_\odot$ yr^{-1})	Optical & UV ($M_\odot$ yr^{-1})	IR ($M_\odot$ yr^{-1})	($\times 10^{43}$ erg s^{-1})
A1795	11^{+2}_{-4}	45	139±25	3.5±0.6
A2052	61^{+3}_{-3}	8	111±20	2.8±0.5
A2597	37^{+2}_{-2}	80	607±115	15.3±2.9
MS0735+7421	42^{+5}_{-5}	184	-	-
A1835	111^{+7}_{-8}	243	15027±2481	377.9±62.4
A1664	33^{+8}_{-6}	93	1344±242	33.8±6.1
MACS1347-11	386^{+11}_{-14}	-	238±23	6.0±0.6
Hydra-A	11^{+1}_{-1}	20	453±80	11.4±2.0
ZwCl3146	197^{+14}_{-13}	642	7400±1358	186.1±34.2
A85	21^{+4}_{-4}	8	62	1.6
RXJ1504.1-0248	162^{+6}_{-6}	747	9428±217	237.1±5.5
A133	24^{+1}_{-1}	1	-	-
PKS0745-191	87^{+5}_{-4}	248	1707±299	42.9±7.5
IC1262	2^{+1}_{-1}	0.2	20	0.5
A262	3^{+1}_{-1}	0.4	22±4	0.6±0.1
A2626	4^{+2}_{-1}	0.7	59	1.5
MACS1423+24	285^{+13}_{-13}	1448	453±15	11.4±0.4
Zw2701	28^{+6}_{-6}	8	1011	25.4
A2199	12^{+1}_{-1}	2	115	2.9
Zw7160	434^{+16}_{-17}	46	117±11	3.0±0.3
A2029	57^{+5}_{-4}	0.6	-	-
AS1101	21^{+1}_{-2}	20	62	1.6
NGC5044	7^{+1}_{-1}	1	18±3	0.5±0.1
Phoenix	553^{+45}_{-44}	-	-	-

Table 4.4: Gas cooling rates calculated for radiative cooling within inner 10 kpc radius region, and non-radiative cooling rates estimated using Hα total IR luminosities as discussed in section 4.5.3.

unclear. However, the exceedingly large IR cooling rates suggest that gas mixing and dust sputtering make up a small fraction of the total IR luminosity. The radiative cooling rates are about 3–4 times larger when $\dot{M}_{\rm H\alpha}$ is less than 10, and the cooling rate through mixing is larger at other times (see the middle panel). However, in all systems, there is a positive trend in all cooling rates.

To estimate the amount of gas that can cool within the lifetimes of cavities, we multiplied the estimated cooling rates by cavity ages and compared the mass of gas expected to have cooled behind cavities with the observed cold gas masses. If the expected cooled gas mass exceeds $M_{\rm disp}$, it is replaced by $M_{\rm disp}$, meaning that all gas uplifted by a cavity has cooled. In Fig. 4.4, we show the relationship between them. When the radiative cooling rate is considered alone, many BCGs have more molecular gas than the expected amount of cooled gas behind cavities suggesting that the observed cavities have not yet cooled enough gas as shown in the left panel. In Some BCGs however, the cavities may have cooled enough gas to match the observed amount of cold gas. When radiative cooling and cooling through mixing are considered together, more gas cools as expected. As a result, more BCGs have comparable to more cooled gas than observed molecular gas mass.

Clearly, many BCGs do not have as much cold gas as they are expected to have if cavities uplifted the maximum amount of gas that they can lift and if the gas cooled at the observed cooling rates. The expected cooled gas masses are upper limits for BCGs when all uplifted gas is expected to have cooled. It is not known whether cavities can efficiently uplift exactly as much gas as they displace. Some analytical studies suggest that a cavity can uplift half the amount of gas it can displace (Pope et al., 2010). Moreover, some cavities are observed at less than 10 kpc distance, therefore, the radiative cooling rate estimated using our simple method is expected to be smaller at smaller radii as the gas mass enclosed is smaller. Nevertheless, many BCGs do not have the expected levels of molecular gas. Either the gas is not cooling efficiently, cavities do not lift enough gas or a combination of both.

4.5.4 How high does gas need to be lifted?

Another important factor to consider is the lifting radius. Cavities should lift the gas to sufficiently high altitudes such that it has enough time to cool before it falls back. Pulido et al. (2018) has showed that most of the cool-core clusters have cold gas detection when $t_{\rm cool}/t_{\rm ff} \sim 10$. Many studies in the literature use free-fall time as a metric for the onset of gas condensation. However, cold gas filaments formed in the uplifted gas would get denser, detach and fall back towards the BCG experiencing the drag forces and ram pressure of

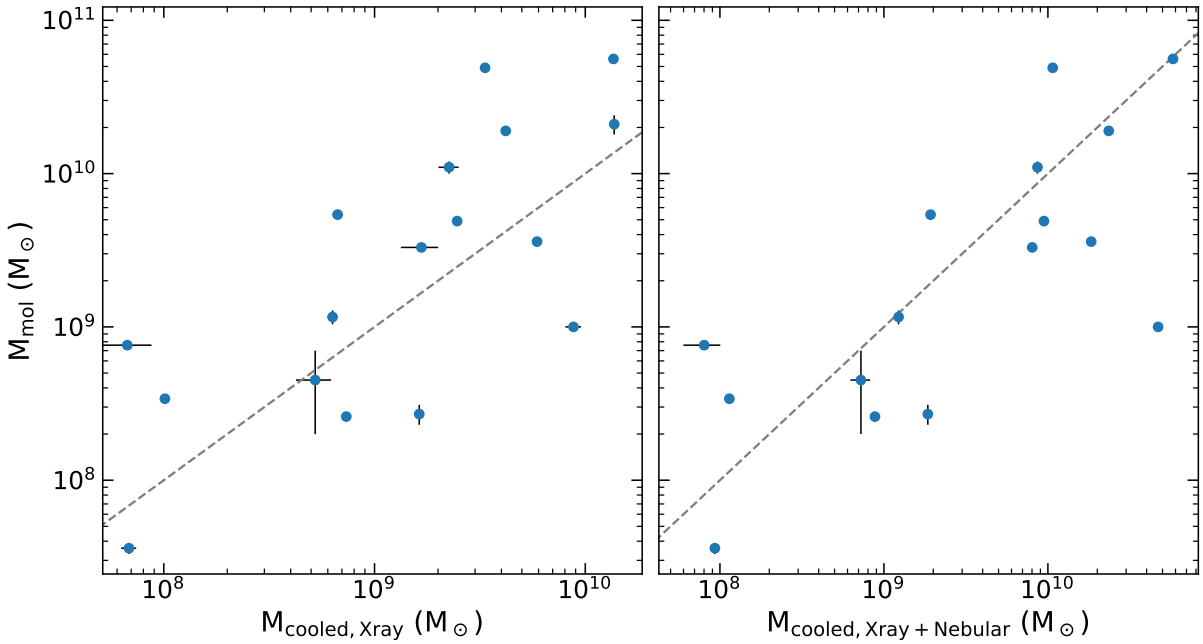

Figure 4.4: The comparison between the amount of uplifted gas expected to have cooled and the observed molecular gas in BCGs. The left panel shows the gas cooled via radiative cooling alone and the right panel shows the gas cooled through radiative cooling and gas mixing.

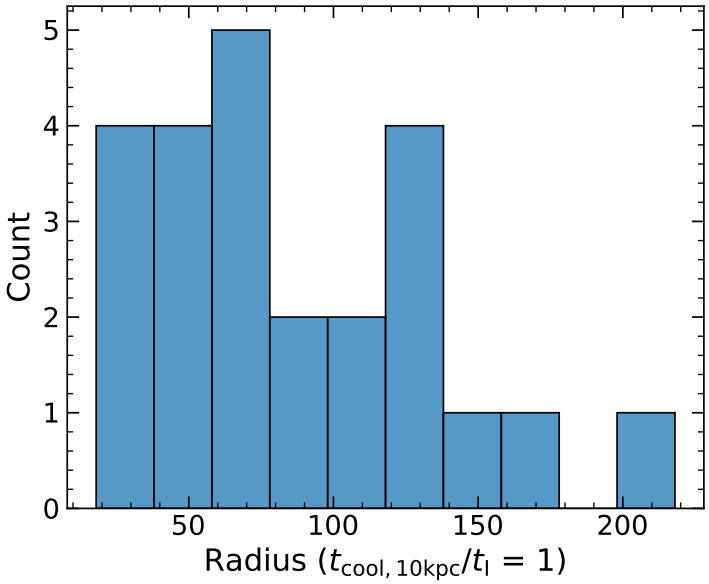

Figure 4.5: Histogram of radii to which gas within central 10 kpc needs to be uplifted for it to cool before it falls back.

the ICM slowing them down. Clouds will eventually reach a terminal velocity and fall back at a longer timescale. Therefore, McNamara et al. (2016) proposed the use of infall time, $t_{\rm I}$, which can be a few times longer than the free-fall time as the quantity to be considered instead of the free-fall time.

To estimate at what altitude the gas needs to be lifted, we assume that the gas uplifted from central regions maintains its cooling time. We estimate the average cooling time in the central 10 kpc region in each. Typically cooling times are less than a Gyr. Assuming that the gas with this cooling time is lifted from central regions, we calculate the radius at which its $t_{\rm cool,10kpc}/2t_{\rm I} \sim 1$. Factor 2 comes from the assumption that the gas takes an equal amount of time to be lifted to an altitude R, the lifting radius, and to fall back at a terminal velocity within its infall time. We use the maximum velocity of the molecular clouds observed in BCGs as the terminal velocity for each cluster, and the average of these velocities as the terminal velocity of the gas in clusters that do not have molecular gas detection. The infall time is then simply calculated as R/v, where v is its terminal velocity. We also calculated the radius at which $t_{\rm cool,10kpc}/2t_{\rm ff} \sim 1$ and 10 for comparison.

The lifting radii for each cluster are summarized in table 4.5 and Fig. 4.5 shows a histogram of radii calculated for the infall time. On average, the $t_{\rm cool,10kpc}/2t_{\rm I} \sim 1$ threshold

Cluster	Radius (kpc)			Hα extent
	$\frac{t_{c,10kpc}}{2t_{ff}} = 1$	$\frac{t_{c,10kpc}}{2t_{ff}} = 10$	$\frac{t_{c,10kpc}}{2t_{I}} = 1$	(kpc)
A1795	407	15	134	54
A2052	178	10	56	6
A2597	128	10	71	23
MS0735+7421	251	12	90	
A1835	149	10	65	45
A1664	114	10	120	61
MACS1347-11	186	10	37	
Hydra-A	336	15	126	20
ZwCl3146	108	10	40	
A85	167	10	65	8
RXCJ1504	122	10	36	
A133	261	11	96	7
PKS0745	128	10	18	34
IC1262	382	24	201	
A262	250	12	123	4
A2626	373	24	171	
MACS1423+24	150	10	45	
Zw2701	503	29	156	
A2199	284	11	98	
Zw7160	223	13	79	
A2029	461	19	111	
AS1101	220	11	72	38
NGC5044	98	10	40	6
Phoenix	114	10	29	

Table 4.5: The table shows the heights to which the central low entropy gas needs to be lifted where thermal instabilities trigger cooling for different $t_{c,10kpc}/2t_{ff}$ and $t_{c,10kpc}/2t_{I}$ criteria (see section 4.5.4 for details). The infall time is defined as $t_{I} = R/v$, where v is the terminal velocity of the gas in km s^{-1}, which is set to the maximum observed velocity of the molecular gas.

is reached at ∼80 kpc. In NGC5044, PKS0745, phoenix, RXCJ1504 and MACS1347-11 the gas only needs to be uplifted to $\lesssim$40 kpc. In the case of PKS0745 and Phoenix, the radii are comparable to the extent of their ionized gas emission and cavity distances. For most clusters, gas needs to be uplifted to higher altitudes in order to cool and fall back. When the free-fall time threshold is considered instead of the infall time, the gas would have to be uplifted to distances of several hundreds of kiloparsecs. It is unlikely as cavities are rarely observed at such large distances. Moreover, the density contrast between the cavity and the ICM would diminish meaning that cavities will be less effective in lifting gas to very large distances. The nebular emission indicating gas cooling is also not observed beyond 40–60 kpc distances in the most extended systems. It further supports the fact that free-fall time is not important for gas cooling.

Simulations of AGN feedback find similar lifting radii. Qiu et al. (2020) simulated outflows driven by AGN feedback and find that cold gas clumps can be lifted to hundreds of kpc. However, they find that the cold gas clumps get destroyed in the ICM beyond a few tens of kpc due to shock heating. In the presence of magnetic fields and dust, the clumps can survive longer and rise to larger distances. We note that the initial launching speeds of cold clouds of several thousand km s^{-1} in their simulations are not observed in BCGs. The observed distance of cold gas from the BCG centre also depends on the stage of the AGN feedback cycle at which the BCG is observed. For example, Li & Bryan (2014) find that extended cold gas is found only during the initial phase of the AGN feedback cycle. At later times all gas is concentrated in central regions. For example, clusters like Phoenix and Perseus may be experiencing a very recent powerful AGN outburst which is driving outflows of gas to large distances, whereas many other clusters are caught at later stages of the AGN feedback cycle.

Nevertheless, the estimated lifting radii are larger than the observed extent of cold gas and cavities in many clusters. McNamara & Nulsen (2012) showed that the cooling time of low entropy gas being lifted adiabatically is mildly sensitive to pressure change. For observed abundances, the radiative cooling time can increase by a factor of 2 to 3 depending on the gas metallicity. Therefore, the average lifting radius can be as high as 160 kpc and several hundred kpc in some clusters making bulk uplift even more difficult. Cavities as well as low-entropy or cold gas are not observed at such large distances in clusters, indicating that stimulated feedback may not work efficiently at all times. It is very likely that a combination of bulk uplift with other cooling channels such as cooling of ambient ICM gas by thermal instabilities triggered by turbulence (Gaspari et al., 2018), gravity waves or shocks (Voit et al., 2017) or cooling through mixing (Fabian et al., 2002) work simultaneously to cool enough the gas to form observed levels of molecular gas in BCGs of cool-core galaxy clusters.

4.6 Summary

We analyzed the X-ray data for 24 cool-core galaxy clusters to study the stimulated feedback mechanism. We studied the gas uplift by X-ray cavities by identifying new cavities and including cavity information previously published for clusters in our sample. Cavities are detected in 21 clusters in our sample. We estimated the gas cooling rates in central regions using radiative and non-radiative cooling channels and compared them with the observed amount of cold has in these systems.

We found that most of the clusters have enough low-entropy gas within the inner 10 kpc region which can cool to form the observed amount of cold molecular gas. Only in some clusters such as A1835, ZwCl3146 and Zw7160 the observed molecular gas mass exceeds the low entropy gas within 10 kpc region, however, they have enough hot gas within 20 kpc.

The maximum amount of gas that can be lifted by all detected cavities in a cluster is comparable to the observed molecular gas mass in majority of clusters. However, a single cavity cannot lift enough gas to match the observed cold gas masses in clusters, which is consistent with results published in the literature.

The X-ray gas cooling rate in inner region correlates with non-radiative gas cooling rates. The radiative cooling alone may be insufficient to cool enough gas. Including non-radiative cooling boosts gas cooling rates and and promote more cooling of gas. Expected cooled gas mass as exceeds cold gas mass suggesting that either cavities do not lift large gas masses or that the gas does not cool efficiently as it rises.

The cooling radii for gas to cool within its infall time are on average $\sim$80 kpc, larger than the observed extent of the detected nebular emission in clusters except in a few cases such as Phoenix and PKS0745. The radii are two times larger if the effect of change in pressure on cooling time of the gas is considered.

We find that bulk uplift of gas by cavities alone is insufficient to lift and cool enough gas in many galaxy clusters. Uplift is still an important for gas cooling. As explained in McNamara et al. (2016) and Martz et al. (2020), “spoiler clusters" like A2029, MACS1347 have short central cooling times and low gas entropies as other cool-core clusters, but they lack detectable levels of cold gas. They have relaxed atmospheres and do now show signs of cavities. A2029 has a central radio source with active jets. But it seems to have failed to uplift low entropy gas. Perhaps the radio activity is recent and it hasn't had enough time to blow cavities. Nevertheless, uplift of low entropy gas is an integral part of other gas cooling models such as the precipitation model (Voit et al., 2017) and the chaotic cold accretion model (Gaspari et al., 2018).

Chapter 5

Conclusion

In this thesis, I studied the impact of radio-mechanical feedback on gas and star formation in inner regions of central cluster galaxies. Particularly, the role of radio-mechanical feedback in expelling cold gas, the origin of cold gas and the nature of radio-jet-triggered star formation. ALMA data was used to study the molecular gas morphology and kinematics, HST data was used to study the recent star formation in Abell 1795 and *Chandra* data to study the cooling of hot X-ray emitting gas behind cavities in cool-core galaxy clusters. By understanding the role of radio-mechanical feedback in expelling the gas from galaxies, forming cold gas and triggering star formation, we learn about AGN feedback cycles which regulate the growth of galaxies.

We compared the properties of molecular flows in BCGs, which are primarily driven by radio-mechanical feedback, with molecular outflows observed in nearby AGN and starburst galaxies to understand the relative impact of different outflow-driving mechanisms. The molecular flows in BCGs are several orders of magnitude larger and heavier compared to flows driven by AGN winds and starbursts. They are, however, slower compared to flows driven by quasar nuclei, but have larger momenta. About half of the total molecular gas lies in outflows in BCGs compared to only 10 per cent or less gas lying in outflows in other AGN hosting and starburst galaxies. The driving powers of both quasar winds and mechanical powers of cavities are comparable to each other and both exceed the kinetic powers of molecular flows by factors of 10–100. To assess the relative efficacies of different feedback mechanisms, we introduced a parameter called the lifting factor which is a product of the mass and size of molecular outflows divided by the driving power. It is considerably larger in BCGs compared to other galaxies showing that radio-mechanical feedback is vastly more capable of lifting large amounts of gas to higher altitudes. The star formation rate per gram of molecular gas in BCGs is 5–10 times lower than in the most massive galaxies with

AGN which indicates that star formation is suppressed. Perhaps because the gas in BCGs rarely forms disks or other stable structures. The observed speeds of molecular gas flows are below their escape speeds which means that the gas will eventually fall back towards the centre.

When the radio jets actively interact with the gas in molecular flows, they can trigger star formation by compressing the gas leading to positive feedback. In chapter 3, we studied radio jet-triggered star formation in the Abell 1795 cluster which is a very well-studied and well-resolved cluster with a wealth of multiwavelength data. I analyzed the VLT XSHOOTER and MUSE data, and ALMA data and combined them with *HST* FUV images to study the interaction between the radio jets and the ISM gas and star formation. The total FUV star formation rate of 9 $M_\odot$ yr^{-1} and $\sim 3 \times 10^8$ $M_\odot$ of molecular gas imply a gas depletion time of 1 Gyr indicating a low star formation efficiency, however, it is location dependent. The stream of stars in the south filament appears spatially offset from the south molecular gas filament. The stars have decoupled from the molecular gas and are moving under the influence of gravity. However, due to the lack of strong absorption features in the spectrum, we were unable to determine their velocities. The nebular emission line diagnostic diagrams suggest that the ISM gas is ionized by a mix of star formation and weak shocks. The velocity structure function of the warm ionized gas may suggest that the radio jets may be able to produce supersonic turbulence in the surrounding medium.

I also discovered a shock-like feature to the north of the central radio source in the MUSE Hα velocity FWHM map. It is also visible in the electron density map, where the densities are elevated in the shocked region. It could be produced by the motion of the BCG through the cluster atmosphere or the radio jets. Although the possibility that it is an artefact of large seeing during MUSE observations cannot be completely ruled out.

The disturbed, filamentary nature of molecular gas in BCGs, their close association with X-ray cavities, low line of sight velocities and the spatial correlation between hot, warm and cold filaments all point towards the in-situ formation of molecular gas behind buoyantly rising X-ray cavities. In chapter 4, I analyzed *Chandra* X-ray data of 24 cool-core clusters to study how much gas can cavities lift and cool behind their wakes. All clusters in our sample have several orders of magnitude more hot gas than total cold gas in their BCGs within the inner 20 kpc radius. In the majority of clusters, multiple generations of cavities can uplift more hot gas than the observed amount of cold gas. However, the amount of uplifted gas expected to cool at its radiative cooling rate within the lifetimes of observed cavities is less than the total molecular gas in more than half of the clusters. Including non-radiative cooling increases the total cooling rate and the amount of cooled gas, but not to the level required to account for all the cold gas in about a third of the clusters. Also, the gas has to be lifted to very altitudes, to distances larger than the extent

of most observed cavities and nebular emission, before it can cool and fall back. Therefore, either the uplift of cold gas by cavities is insufficient to cool enough hot gas in some galaxy clusters or cooling needs to be more efficient.

In this thesis, I explored the impact radio jets and the cavities they inflate might have on their ambient gas as they operate through negative and positive feedback. Only a small fraction of AGN in the nearby Universe are radio active. Fluetsch et al. (2019) did not observe a correlation between radio power and flow power in nearby galaxies in their sample and concluded that radio mechanical feedback is ineffective in driving cold gas outflows in those galaxies. Our analysis of molecular flows in BCGs powered by radio-mechanical feedback showed that when active, radio-mechanical feedback can be vastly more powerful at driving cold gas outflows than other feedback mechanisms. Even in galaxies where all the feedback mechanisms are acting simultaneously, radio-mechanical feedback is more important, as seen in the Phoenix BCG.

In addition to the negative feedback of radio jets, they can also trigger star formation in the host galaxy. Several examples of radio-jet triggered star formation in the gas in the host galaxy are known. However, examples of radio-jet triggered star formation in an outflowing gas are relatively rare. Our analysis of Abell 1795 showed that the star formation induced by radio jets on a timescale of a few million years follows the KS relationship. This is in agreement with analytical arguments and simulations of pressure-regulated radio-jet triggered star formation (Silk, 2013; Bieri et al., 2016). However, this phase may be short-lived and the star formation may be quenched on longer timescales.

Although radio-mechanical feedback in the present day Universe primarily acts to heat the ICM and atmospheres of massive galaxies, it can effectively expel gas out of galaxies and suppress star formation while promoting star formation on a short timescale. The radio-mechanical feedback is expected to expel the gas from young galaxies during galaxy formation (Bower et al., 2008). Most massive galaxies are thought to have gone through a phase of high AGN activity with powerful quasars and radio jets at some point during their evolution. Some studies have found the radio mechanical feedback as the most favourable mechanism for driving gas outflows in high-redshift galaxies (see for example, Nesvadba et al., 2017). However, these studies are based on indirect evidence and energetic arguments and lack a direct association between outflowing gas and radio jets. High-resolution radio images and spatially resolved kinematic maps of the outflow are required to spatially map and compare the radio emission and the outflow.

The galaxies included in our analyses are some of the most massive and relatively nearby (except for Phoenix) central cluster galaxies. Because of their proximity, dense atmospheres and deep multiwavelength coverage, they provide the most complete view of

radio-mechanical feedback in action where heating of circumgalactic gas, galactic outflows as well as radio-jet triggered star formation can be observed and studied in detail. AGN feedback is important for the formation and evolution of galaxies during the galaxy formation epoch. Observations of radio-mechanical feedback at high redshifts are less informative due to the dearth of deep, multi-wavelength, high spatial resolution data compared to its effects observed in BCGs residing in cooling flow clusters. Therefore, the knowledge of the radio-mechanical feedback in cooling flow clusters can be used to understand how the radio-mechanical feedback has been operating during the epoch of galaxy formation and growth.

5.1 Future Work

In this thesis, molecular gas flows are analyzed only for a handful of systems. To date, molecular gas flows have been resolved in roughly 20 BCGs which comprise some of the most massive and gas-rich galaxies. Whether molecular gas filaments are common in elliptical galaxies as they are in BCGs is a critical question in galaxy evolution. The next step is to increase the sample of resolved molecular flows in galaxies to include radio-mechanical feedback driven flows in some of the lower-mass galaxies. Combining these observations with measurements of star formation rates, AGN cavity powers and other parameters would confirm whether the trends observed between molecular gas flows, star formation and driving power in the current sample are universal. Any deviation with mass may imply that radio-mechanical feedback operates differently in lower-mass systems.

Future work will also expand the sample of AGN feedback driven outflows, particularly by the radio-mechanical feedback, in the high redshift Universe. One of the ways to achieve this goal is to find galaxy scale outflows in high redshift galaxies in deep optical spectroscopic and imaging surveys such as the Sloan Digital Sky Survey (SDSS). The presence of broad gas emission lines in the spectra of galaxies could indicate gas outflow. The BPT analysis of available nebular emission lines can be used to identify the presence of an AGN. Several studies have employed. Interesting candidates can then be followed up with high spatial and spectral resolution observations at infrared and radio wavelengths to detect the presence of radio jets, molecular gas and star formation. For example, the James Webb Space Telescope (JWST) observations can detect redshifted optical nebular emission lines and the distribution and kinematics of gas in and around galaxies, and ALMA observations of higher CO transitions can trace dense and cold molecular gas. These measurements would not only be useful in studying the role of radio-mechanical feedback in the early Universe and its relative importance compared to other feedback

mechanisms but also to study its evolution with time.

Another future research avenue is to study the physical conditions of the filamentary molecular gas in BCGs. While a significant amount of molecular gas is present in the filaments, it is not forming as many stars as in other nearby galaxies suggesting that the physical conditions in filaments may be different. One of the ways to address this problem is to observe several CO emission lines in individual systems. Observing 4 or more CO emission lines will allow a complete excitation analysis of cold gas. This will allow the estimation of temperature, density and column density of molecular gas without having to assume local thermodynamic equilibrium in the gas, which is a common assumption in deriving the mass of molecular gas from a single CO emission line removing a significant uncertainty in mass as well. Moreover, if this analysis is spatially resolved, variations in the physical conditions of the gas can be studied. Alternatively, observing warm molecular gas in the NIR would allow estimating the variation in the mass ratio of the warm-to-cold molecular gas. It can probe heating processes in the gas including young stars, jet collisions and the dissipation of mechanical bubble energy.

References

Aalto, S., Garcia-Burillo, S., Muller, S., et al. 2012, A&A, 537, A44

Agertz, O., Lake, G., Teyssier, R., et al. 2009, MNRAS, 392, 294

Alatalo, K., Blitz, L., Young, L. M., et al. 2011, ApJ, 735, 88

Anders, E., & Grevesse, N. 1989, , 53, 197

Appleton, P. N., Guillard, P., Boulanger, F., et al. 2013, ApJ, 777, 66

Arnaud, K. A. 1996, in Astronomical Society of the Pacific Conference Series, Vol. 101, Astronomical Data Analysis Software and Systems V, ed. G. H. Jacoby & J. Barnes, 17

Babyk, I., McNamara, B., Tamhane, P., et al. 2021, arXiv e-prints, arXiv:2110.15410

Babyk, I. V., McNamara, B. R., Tamhane, P. D., et al. 2019, ApJ, 887, 149

Baldwin, J. A., Phillips, M. M., & Terlevich, R. 1981, PASP, 93, 5

Balogh, M. L., Pearce, F. R., Bower, R. G., & Kay, S. T. 2001, MNRAS, 326, 1228

Bambic, C. J., Pinto, C., Fabian, A. C., Sanders, J., & Reynolds, C. S. 2018, MNRAS, 478, L44

Banerjee, N., & Sharma, P. 2014, MNRAS, 443, 687

Baron, D., & Netzer, H. 2019, MNRAS, 486, 4290

Baugh, C. M. 2006, Reports on Progress in Physics, 69, 3101

Beckmann, R. S., Devriendt, J., Slyz, A., et al. 2017, MNRAS, 472, 949

Best, P. N., Kauffmann, G., Heckman, T. M., et al. 2005, MNRAS, 362, 25

Best, P. N., Lehnert, M. D., Miley, G. K., & Röttgering, H. J. A. 2003, MNRAS, 343, 1

Bieri, R., Dubois, Y., Silk, J., Mamon, G. A., & Gaibler, V. 2016, MNRAS, 455, 4166

Binney, J., & Tabor, G. 1995, MNRAS, 276, 663

Bird, J., Martini, P., & Kaiser, C. 2008, ApJ, 676, 147

Bîrzan, L., McNamara, B. R., Nulsen, P. E. J., Carilli, C. L., & Wise, M. W. 2008, ApJ, 686, 859

Bîrzan, L., Rafferty, D. A., McNamara, B. R., Wise, M. W., & Nulsen, P. E. J. 2004, ApJ, 607, 800

Bîrzan, L., Rafferty, D. A., Nulsen, P. E. J., et al. 2012, MNRAS, 427, 3468

Boehringer, H., & Morfill, G. E. 1988, ApJ, 330, 609

Boehringer, H., Voges, W., Fabian, A. C., Edge, A. C., & Neumann, D. M. 1993, MNRAS, 264, L25

Boizelle, B. D., Barth, A. J., Darling, J., et al. 2017, ApJ, 845, 170

Bolatto, A. D., Wolfire, M., & Leroy, A. K. 2013, ARA&A, 51, 207

Bower, R. G., Benson, A. J., Malbon, R., et al. 2006, MNRAS, 370, 645

Bower, R. G., McCarthy, I. G., & Benson, A. J. 2008, MNRAS, 390, 1399

Bregman, J. N. 2007, ARA&A, 45, 221

Brienza, M., Shimwell, T. W., de Gasperin, F., et al. 2021, Nature Astronomy, arXiv:2110.09189

Brightman, M., Baloković, M., Ballantyne, D. R., et al. 2017, ApJ, 844, 10

Brook, C. B., Governato, F., Roškar, R., et al. 2011, MNRAS, 415, 1051

Calzadilla, M. S., Russell, H. R., McDonald, M. A., et al. 2019, ApJ, 875, 65

Canizares, C. R., Clark, G. W., Jernigan, J. G., & Markert, T. H. 1982, ApJ, 262, 33

Canizares, C. R., Markert, T. H., & Donahue, M. E. 1988, in NATO Advanced Study Institute (ASI) Series C, Vol. 229, Cooling Flows in Clusters and Galaxies, ed. A. C. Fabian, 63

Canning, R. E. A., Ryon, J. E., Gallagher, J. S., et al. 2014, MNRAS, 444, 336

Cano-Díaz, M., Maiolino, R., Marconi, A., et al. 2012, A&A, 537, L8

Cappellari, M. 2017, MNRAS, 466, 798

Cappellari, M., & Copin, Y. 2003, MNRAS, 342, 345

Cardelli, J. A., Clayton, G. C., & Mathis, J. S. 1989, ApJ, 345, 245

Carilli, C. L., Perley, R. A., & Harris, D. E. 1994, MNRAS, 270, 173

Carnall, A. C. 2017, arXiv e-prints, arXiv:1705.05165

Carniani, S., Marconi, A., Maiolino, R., et al. 2016, A&A, 591, A28

Cavagnolo, K. W., Donahue, M., Voit, G. M., & Sun, M. 2008, ApJL, 683, L107

Cavagnolo, K. W., McNamara, B. R., Nulsen, P. E. J., et al. 2010, ApJ, 720, 1066

Ceverino, D., & Klypin, A. 2009, ApJ, 695, 292

Churazov, E., Forman, W., Jones, C., & Böhringer, H. 2000, A&A, 356, 788

Churazov, E., Ruszkowski, M., & Schekochihin, A. 2013, MNRAS, 436, 526

Churazov, E., Sazonov, S., Sunyaev, R., et al. 2005, MNRAS, 363, L91

Cicone, C., Feruglio, C., Maiolino, R., et al. 2012, A&A, 543, A99

Cicone, C., Maiolino, R., Sturm, E., et al. 2014, A&A, 562, A21

Cole, S., Aragon-Salamanca, A., Frenk, C. S., Navarro, J. F., & Zepf, S. E. 1994, MNRAS, 271, 781

Combes, F., García-Burillo, S., Casasola, V., et al. 2013, A&A, 558, A124

Conroy, C. 2013, ARA&A, 51, 393

Corwin, Harold G., J., Buta, R. J., & de Vaucouleurs, G. 1994, AJ, 108, 2128

Cowie, L. L., & Binney, J. 1977, ApJ, 215, 723

Crawford, C. S., Allen, S. W., Ebeling, H., Edge, A. C., & Fabian, A. C. 1999, MNRAS, 306, 857

Crawford, C. S., Sanders, J. S., & Fabian, A. C. 2005, MNRAS, 361, 17

Cresci, G., Marconi, A., Zibetti, S., et al. 2015, A&A, 582, A63

Crockett, R. M., Shabala, S. S., Kaviraj, S., et al. 2012, MNRAS, 421, 1603

Croston, J. H., Ineson, J., & Hardcastle, M. J. 2018, MNRAS, 476, 1614

Croton, D. J., & Farrar, G. R. 2008, MNRAS, 386, 2285

Croton, D. J., Springel, V., White, S. D. M., et al. 2006, MNRAS, 365, 11

Davé, R., Finlator, K., & Oppenheimer, B. D. 2012, MNRAS, 421, 98

Davé, R., Cen, R., Ostriker, J. P., et al. 2001, ApJ, 552, 473

David, L. P., Lim, J., Forman, W., et al. 2014, ApJ, 792, 94

Davies, R., Förster Schreiber, N. M., Cresci, G., et al. 2011, ApJ, 741, 69

Davies, R. I., Müller Sánchez, F., Genzel, R., et al. 2007, ApJ, 671, 1388

Davis, F., Kaviraj, S., Hardcastle, M. J., et al. 2022, MNRAS, arXiv:2201.09903

Dekel, A., & Silk, J. 1986, ApJ, 303, 39

Diehl, S., Li, H., Fryer, C. L., & Rafferty, D. 2008, ApJ, 687, 173

Diesing, R., & Caprioli, D. 2018, , 121, 091101

Domínguez, A., Siana, B., Henry, A. L., et al. 2013, ApJ, 763, 145

Donahue, M., de Messières, G. E., O'Connell, R. W., et al. 2011, ApJ, 732, 40

Donahue, M., & Voit, G. M. 2022, , 973, 1

Donahue, M., Connor, T., Fogarty, K., et al. 2015, ApJ, 805, 177

Downes, D., & Solomon, P. M. 1998, ApJ, 507, 615

Downes, D., Solomon, P. M., & Radford, S. J. E. 1993, ApJL, 414, L13

Duan, X., & Guo, F. 2018, ApJ, 861, 106

Dubois, Y., & Teyssier, R. 2008, A&A, 477, 79

Duggal, C., O'Dea, C., Baum, S., et al. 2021, Astronomische Nachrichten, 342, 1087

Edge, A. C. 2001, MNRAS, 328, 762

Edge, A. C., Wilman, R. J., Johnstone, R. M., et al. 2002, MNRAS, 337, 49

El-Badry, K., Ostriker, E. C., Kim, C.-G., Quataert, E., & Weisz, D. R. 2019, MNRAS, 490, 1961

Emonts, B. H. C., Norris, R. P., Feain, I., et al. 2014, MNRAS, 438, 2898

Fabian, A. C. 1994, ARA&A, 32, 277

—. 1999, MNRAS, 308, L39

—. 2012, ARA&A, 50, 455

Fabian, A. C., Allen, S. W., Crawford, C. S., et al. 2002, MNRAS, 332, L50

Fabian, A. C., & Nulsen, P. E. J. 1977, MNRAS, 180, 479

Fabian, A. C., Reynolds, C. S., Taylor, G. B., & Dunn, R. J. H. 2005, MNRAS, 363, 891

Fabian, A. C., Sanders, J. S., Ettori, S., et al. 2001, MNRAS, 321, L33

Fabian, A. C., Sanders, J. S., Williams, R. J. R., et al. 2011, MNRAS, 417, 172

Faucher-Giguère, C.-A., & Quataert, E. 2012, MNRAS, 425, 605

Federrath, C. 2013, MNRAS, 436, 1245

Ferland, G. J., Fabian, A. C., Hatch, N. A., et al. 2009, MNRAS, 392, 1475

Feruglio, C., Maiolino, R., Piconcelli, E., et al. 2010, A&A, 518, L155

Feruglio, C., Fiore, F., Carniani, S., et al. 2015, A&A, 583, A99

Fiore, F., Feruglio, C., Shankar, F., et al. 2017, A&A, 601, A143

Fluetsch, A., Maiolino, R., Carniani, S., et al. 2019, MNRAS, 483, 4586

Forman, W., Jones, C., Churazov, E., et al. 2007, ApJ, 665, 1057

Freeman, P. E., Kashyap, V., Rosner, R., & Lamb, D. Q. 2002, ApJS, 138, 185

Freudling, W., Romaniello, M., Bramich, D. M., et al. 2013, A&A, 559, A96

Fumagalli, M., Fossati, M., Hau, G. K. T., et al. 2014, MNRAS, 445, 4335

Gaibler, V., Khochfar, S., Krause, M., & Silk, J. 2012, MNRAS, 425, 438

Gallagher, R., Maiolino, R., Belfiore, F., et al. 2019, MNRAS, 485, 3409

Gaspari, M., Temi, P., & Brighenti, F. 2017, MNRAS, 466, 677

Gaspari, M., McDonald, M., Hamer, S. L., et al. 2018, ApJ, 854, 167

Gastaldello, F., Buote, D. A., Temi, P., et al. 2009, ApJ, 693, 43

Gentry, E. S., Krumholz, M. R., Dekel, A., & Madau, P. 2017, MNRAS, 465, 2471

Gitti, M., Nulsen, P. E. J., David, L. P., McNamara, B. R., & Wise, M. W. 2011, ApJ, 732, 13

González Delgado, R. M., Cerviño, M., Martins, L. P., Leitherer, C., & Hauschildt, P. H. 2005, MNRAS, 357, 945

Governato, F., Brook, C., Mayer, L., et al. 2010, Nature, 463, 203

Graham, A. W., Erwin, P., Caon, N., & Trujillo, I. 2001, ApJL, 563, L11

Graham, A. W., & Scott, N. 2013, ApJ, 764, 151

Gültekin, K., Richstone, D. O., Gebhardt, K., et al. 2009, ApJ, 698, 198

Guo, F., Duan, X., & Yuan, Y.-F. 2018, MNRAS, 473, 1332

Haehnelt, M. G., Natarajan, P., & Rees, M. J. 1998, MNRAS, 300, 817

Hamer, S. L., Edge, A. C., Swinbank, A. M., et al. 2016, MNRAS, 460, 1758

Häring, N., & Rix, H.-W. 2004, ApJL, 604, L89

Heckman, T. M. 1981, ApJL, 250, L59

Heckman, T. M., & Best, P. N. 2014, ARA&A, 52, 589

Heyer, M., & Dame, T. M. 2015, ARA&A, 53, 583

Hicks, A. K., & Mushotzky, R. 2005, ApJL, 635, L9

Hitomi Collaboration, Aharonian, F., Akamatsu, H., et al. 2016, Nature, 535, 117

Hlavacek-Larrondo, J., McDonald, M., Benson, B. A., et al. 2015, ApJ, 805, 35

Hogan, M. T., McNamara, B. R., Pulido, F., et al. 2017, ApJ, 837, 51

Hu, H., Qiu, Y., Gendron-Marsolais, M.-L., et al. 2022a, ApJL, 929, L30

Hu, Y., Federrath, C., Xu, S., & Mathew, S. S. 2022b, MNRAS, 513, 2100

Hudson, D. S., Mittal, R., Reiprich, T. H., et al. 2010, A&A, 513, A37

Ishibashi, W., & Fabian, A. C. 2012, MNRAS, 427, 2998

—. 2014, MNRAS, 441, 1474

Ishibashi, W., Fabian, A. C., & Maiolino, R. 2018, MNRAS, 476, 512

Jahnke, K., & Macciò, A. V. 2011, ApJ, 734, 92

Jarvis, M. E., Harrison, C. M., Thomson, A. P., et al. 2019, MNRAS, 485, 2710

Johnstone, R. M., Canning, R. E. A., Fabian, A. C., et al. 2012, MNRAS, 425, 1421

Johnstone, R. M., Fabian, A. C., & Nulsen, P. E. J. 1987, MNRAS, 224, 75

Joung, M. K. R., & Mac Low, M.-M. 2006, ApJ, 653, 1266

Joung, M. R., Mac Low, M.-M., & Bryan, G. L. 2009, ApJ, 704, 137

Kaastra, J. S., Ferrigno, C., Tamura, T., et al. 2001, A&A, 365, L99

Kalberla, P. M. W., Burton, W. B., Hartmann, D., et al. 2005, A&A, 440, 775

Kannan, R., Stinson, G. S., Macciò, A. V., et al. 2014, MNRAS, 437, 3529

Kauffmann, G., & Haehnelt, M. 2000a, MNRAS, 311, 576

—. 2000b, MNRAS, 311, 576

Kauffmann, G., Heckman, T. M., Tremonti, C., et al. 2003, MNRAS, 346, 1055

Kellermann, K. I., Condon, J. J., Kimball, A. E., Perley, R. A., & Ivezić, Ž. 2016, ApJ, 831, 168

Kennicutt, Robert C., J. 1998, ApJ, 498, 541

Kennicutt, R. C., & Evans, N. J. 2012, ARA&A, 50, 531

Kewley, L. J., Dopita, M. A., Sutherland, R. S., Heisler, C. A., & Trevena, J. 2001, ApJ, 556, 121

Kim, J., Balsara, D., & Mac Low, M.-M. 2001, Journal of Korean Astronomical Society, 34, 333

Kimm, T., Cen, R., Devriendt, J., Dubois, Y., & Slyz, A. 2015, MNRAS, 451, 2900

King, A. 2003, ApJL, 596, L27

King, A., & Pounds, K. 2015, ARA&A, 53, 115

Kirkpatrick, C. C., & McNamara, B. R. 2015, MNRAS, 452, 4361

Kirkpatrick, C. C., McNamara, B. R., & Cavagnolo, K. W. 2011, ApJL, 731, L23

Klessen, R. S., Heitsch, F., & Mac Low, M.-M. 2000, ApJ, 535, 887

Kokotanekov, G., Wise, M. W., de Vries, M., & Intema, H. T. 2018, A&A, 618, A152

Koratkar, A., & Blaes, O. 1999, PASP, 111, 1

Kormendy, J., Bender, R., & Cornell, M. E. 2011, Nature, 469, 374

Kormendy, J., & Richstone, D. 1995, ARA&A, 33, 581

Krumholz, M. R., & McKee, C. F. 2005, ApJ, 630, 250

Lacy, M., Croft, S., Fragile, C., Wood, S., & Nyland, K. 2017, ApJ, 838, 146

Leitherer, C., Schaerer, D., Goldader, J. D., et al. 1999, ApJS, 123, 3

Li, Y., & Bryan, G. L. 2014, ApJ, 789, 153

Li, Y., Bryan, G. L., Ruszkowski, M., et al. 2015, ApJ, 811, 73

Li, Y., Ruszkowski, M., & Tremblay, G. 2018, ApJ, 854, 91

Li, Y., Gendron-Marsolais, M.-L., Zhuravleva, I., et al. 2020, ApJL, 889, L1

Lim, J., Ao, Y., & Dinh-V-Trung. 2008, ApJ, 672, 252

Lipari, S., Sanchez, S. F., Bergmann, M., et al. 2009, MNRAS, 392, 1295

Liu, H., Pinto, C., Fabian, A. C., Russell, H. R., & Sanders, J. S. 2019, MNRAS, 485, 1757

Longmore, S. N., Kruijssen, J. M. D., Bastian, N., et al. 2014, in Protostars and Planets VI, ed. H. Beuther, R. S. Klessen, C. P. Dullemond, & T. Henning, 291

Loubser, S. I., Hoekstra, H., Babul, A., & O'Sullivan, E. 2018, MNRAS, 477, 335

Lusso, E., Comastri, A., Simmons, B. D., et al. 2012, MNRAS, 425, 623

Ma, C. J., McNamara, B. R., & Nulsen, P. E. J. 2013, ApJ, 763, 63

Mac Low, M.-M., & Klessen, R. S. 2004, Reviews of Modern Physics, 76, 125

Magorrian, J., Tremaine, S., Richstone, D., et al. 1998, AJ, 115, 2285

Mahony, E. K., Oonk, J. B. R., Morganti, R., et al. 2016, MNRAS, 455, 2453

Main, R. A., McNamara, B. R., Nulsen, P. E. J., Russell, H. R., & Vantyghem, A. N. 2017, MNRAS, 464, 4360

Maiolino, R., Gallerani, S., Neri, R., et al. 2012, MNRAS, 425, L66

Maiolino, R., Russell, H. R., Fabian, A. C., et al. 2017, Nature, 544, 202

Manzano-King, C. M., Canalizo, G., & Sales, L. V. 2019, ApJ, 884, 54

Martin, C. L. 1999, ApJ, 513, 156

Martínez-González, S., Wünsch, R., Silich, S., et al. 2019, ApJ, 887, 198

Martini, P., & Schneider, D. P. 2003, ApJL, 597, L109

Martz, C. G., McNamara, B. R., Nulsen, P. E. J., et al. 2020, ApJ, 897, 57

McCourt, M., Sharma, P., Quataert, E., & Parrish, I. J. 2012, MNRAS, 419, 3319

McDonald, M., Gaspari, M., McNamara, B. R., & Tremblay, G. R. 2018, ApJ, 858, 45

McDonald, M., Roediger, J., Veilleux, S., & Ehlert, S. 2014, ApJL, 791, L30

McDonald, M., Veilleux, S., & Rupke, D. S. N. 2012a, ApJ, 746, 153

McDonald, M., Veilleux, S., Rupke, D. S. N., & Mushotzky, R. 2010, ApJ, 721, 1262

McDonald, M., Bayliss, M., Benson, B. A., et al. 2012b, Nature, 488, 349

McDonald, M., McNamara, B. R., van Weeren, R. J., et al. 2015, ApJ, 811, 111

McDonald, M., McNamara, B. R., Voit, G. M., et al. 2019, ApJ, 885, 63

McIntosh, D. H., Bell, E. F., Rix, H.-W., et al. 2005, ApJ, 632, 191

McKee, C. F., & Ostriker, E. C. 2007, ARA&A, 45, 565

McMullin, J. P., Waters, B., Schiebel, D., Young, W., & Golap, K. 2007, in Astronomical Society of the Pacific Conference Series, Vol. 376, Astronomical Data Analysis Software and Systems XVI, ed. R. A. Shaw, F. Hill, & D. J. Bell, 127

McNamara, B. R., & Nulsen, P. E. J. 2007, ARA&A, 45, 117

—. 2012, New Journal of Physics, 14, 055023

McNamara, B. R., & O'Connell, R. W. 1989, AJ, 98, 2018

—. 1993, AJ, 105, 417

McNamara, B. R., Russell, H. R., Nulsen, P. E. J., et al. 2016, ApJ, 830, 79

McNamara, B. R., Wise, M., Sarazin, C. L., Jannuzi, B. T., & Elston, R. 1996a, ApJL, 466, L9

—. 1996b, ApJL, 466, L9

McNamara, B. R., Wise, M., Nulsen, P. E. J., et al. 2000, ApJL, 534, L135

McNamara, B. R., Rafferty, D. A., Bîrzan, L., et al. 2006, ApJ, 648, 164

McNamara, B. R., Russell, H. R., Nulsen, P. E. J., et al. 2014, ApJ, 785, 44

Meece, G. R., Voit, G. M., & O'Shea, B. W. 2017, ApJ, 841, 133

Mezcua, M., Suh, H., & Civano, F. 2019, MNRAS, 488, 685

Modigliani, A., Goldoni, P., Royer, F., et al. 2010, in Society of Photo-Optical Instrumentation Engineers (SPIE) Conference Series, Vol. 7737, Observatory Operations: Strategies, Processes, and Systems III, ed. D. R. Silva, A. B. Peck, & B. T. Soifer, 773728

Mohapatra, R., Jetti, M., Sharma, P., & Federrath, C. 2022, MNRAS, 510, 2327

Moore, B. 1994, Nature, 370, 629

Morganti, R., Fogasy, J., Paragi, Z., Oosterloo, T., & Orienti, M. 2013, Science, 341, 1082

Morganti, R., Oosterloo, T., Oonk, J. B. R., Frieswijk, W., & Tadhunter, C. 2015, A&A, 580, A1

Morganti, R., Oosterloo, T., Tadhunter, C., Bernhard, E. P., & Oonk, J. B. R. 2021, arXiv e-prints, arXiv:2109.13516

Morganti, R., Tadhunter, C. N., & Oosterloo, T. A. 2005, A&A, 444, L9

Morris, R. G., & Fabian, A. C. 2003, MNRAS, 338, 824

Moster, B. P., Somerville, R. S., Maulbetsch, C., et al. 2010, ApJ, 710, 903

Mukherjee, D., Bicknell, G. V., Wagner, A. e. Y., Sutherland, R. S., & Silk, J. 2018, MNRAS, 479, 5544

Mulcahey, C. R., Leslie, S. K., Jackson, T. M., et al. 2022, A&A, 665, A144

Murray, N., Quataert, E., & Thompson, T. A. 2005, ApJ, 618, 569

Navarro, J. F., Frenk, C. S., & White, S. D. M. 1997, ApJ, 490, 493

Nesvadba, N. P. H., Bicknell, G. V., Mukherjee, D., & Wagner, A. Y. 2020, A&A, 639, L13

Nesvadba, N. P. H., Drouart, G., De Breuck, C., et al. 2017, A&A, 600, A121

Nesvadba, N. P. H., Lehnert, M. D., Eisenhauer, F., et al. 2006, ApJ, 650, 693

Nesvadba, N. P. H., Wagner, A. Y., Mukherjee, D., et al. 2021, A&A, 654, A8

Nobels, F. S. J., Schaye, J., Schaller, M., Bahé, Y. M., & Chaikin, E. 2022, MNRAS, 515, 4838

Norberg, P., Cole, S., Baugh, C. M., et al. 2002, MNRAS, 336, 907

Novikov, I. D., & Thorne, K. S. 1973, in Black Holes (Les Astres Occlus), 343–450

Nulsen, P. E. J. 1986, MNRAS, 221, 377

Nulsen, P. E. J., David, L. P., McNamara, B. R., et al. 2002, ApJ, 568, 163

O'Dea, C. P., Baum, S. A., Privon, G., et al. 2008, ApJ, 681, 1035

Olivares, V., Salome, P., Combes, F., et al. 2019, A&A, 631, A22

Oppenheimer, B. D., & Davé, R. 2006, MNRAS, 373, 1265

Osterbrock, D. E. 1989, Astrophysics of gaseous nebulae and active galactic nuclei

Osterbrock, D. E., & Ferland, G. J. 2006, Astrophysics of gaseous nebulae and active galactic nuclei

O'Sullivan, E., Combes, F., Babul, A., et al. 2021, MNRAS, 508, 3796

Pandge, M. B., Sonkamble, S. S., Parekh, V., et al. 2019, ApJ, 870, 62

Peng, C. Y. 2007, ApJ, 671, 1098

Peterson, J. R., Paerels, F. B. S., Kaastra, J. S., et al. 2001, A&A, 365, L104

Pizzolato, F., & Soker, N. 2005, ApJ, 632, 821

Planck Collaboration, Aghanim, N., Akrami, Y., et al. 2020, A&A, 641, A6

Polles, F. L., Salomé, P., Guillard, P., et al. 2021, A&A, 651, A13

Pope, E. C. D., Babul, A., Pavlovski, G., Bower, R. G., & Dotter, A. 2010, MNRAS, 406, 2023

Powell, L. C., Slyz, A., & Devriendt, J. 2011, MNRAS, 414, 3671

Prasad, D., Sharma, P., & Babul, A. 2018, ApJ, 863, 62

Prasad, D., Sharma, P., Babul, A., Voit, G. M., & O'Shea, B. W. 2020, MNRAS, 495, 594

Proxauf, B., Öttl, S., & Kimeswenger, S. 2014, A&A, 561, A10

Pulido, F. A., McNamara, B. R., Edge, A. C., et al. 2018, ApJ, 853, 177

Qiu, Y., Bogdanović, T., Li, Y., McDonald, M., & McNamara, B. R. 2020, Nature Astronomy, 4, 900

Qiu, Y., Hu, H., Inayoshi, K., et al. 2021, ApJL, 917, L7

Rafferty, D. A., McNamara, B. R., Nulsen, P. E. J., & Wise, M. W. 2006, ApJ, 652, 216

Randall, S. W., Forman, W. R., Giacintucci, S., et al. 2011, ApJ, 726, 86

Revaz, Y., Combes, F., & Salomé, P. 2008, A&A, 477, L33

Rodríguez del Pino, B., Arribas, S., Piqueras López, J., Villar-Martín, M., & Colina, L. 2019, MNRAS, 486, 344

Rose, T., Edge, A. C., Combes, F., et al. 2019a, MNRAS, 489, 349

—. 2019b, MNRAS, 485, 229

Ruffa, I., Prandoni, I., Davis, T. A., et al. 2022, MNRAS, 510, 4485

Ruffa, I., Prandoni, I., Laing, R. A., et al. 2019, MNRAS, 484, 4239

Rupke, D. 2018, Galaxies, 6, 138

Rupke, D. S. N., Gültekin, K., & Veilleux, S. 2017, ApJ, 850, 40

Russell, H. R., McNamara, B. R., Edge, A. C., et al. 2013, MNRAS, 432, 530

Russell, H. R., Sanders, J. S., & Fabian, A. C. 2008, MNRAS, 390, 1207

Russell, H. R., McNamara, B. R., Edge, A. C., et al. 2014, ApJ, 784, 78

Russell, H. R., McNamara, B. R., Fabian, A. C., et al. 2016, MNRAS, 458, 3134

Russell, H. R., McDonald, M., McNamara, B. R., et al. 2017a, ApJ, 836, 130

Russell, H. R., McNamara, B. R., Fabian, A. C., et al. 2017b, MNRAS, 472, 4024

—. 2019, arXiv e-prints, arXiv:1902.09227

Ruszkowski, M., Brüggen, M., & Begelman, M. C. 2004, ApJ, 611, 158

Salem, M., Bryan, G. L., & Corlies, L. 2016, MNRAS, 456, 582

Salomé, P., & Combes, F. 2003, A&A, 412, 657

—. 2004, A&A, 415, L1

Salomé, P., Combes, F., Revaz, Y., et al. 2011, A&A, 531, A85

Salomé, P., Combes, F., Edge, A. C., et al. 2006, A&A, 454, 437

Salomé, Q., Salomé, P., & Combes, F. 2015, A&A, 574, A34

Salomé, Q., Salomé, P., Combes, F., Hamer, S., & Heywood, I. 2016, A&A, 586, A45

Salomé, Q., Salomé, P., Miville-Deschênes, M. A., Combes, F., & Hamer, S. 2017, A&A, 608, A98

Salpeter, E. E. 1955, ApJ, 121, 161

Sanders, J. S., & Fabian, A. C. 2007, MNRAS, 381, 1381

Santoro, F., Oonk, J. B. R., Morganti, R., Oosterloo, T. A., & Tadhunter, C. 2016, A&A, 590, A37

Sarazin, C. L. 1988, X-ray emission from clusters of galaxies

Scannapieco, C., Tissera, P. B., White, S. D. M., & Springel, V. 2008, MNRAS, 389, 1137

Scannapieco, C., Wadepuhl, M., Parry, O. H., et al. 2012, MNRAS, 423, 1726

Scannapieco, E., & Oh, S. P. 2004, ApJ, 608, 62

Schawinski, K., Koss, M., Berney, S., & Sartori, L. F. 2015, MNRAS, 451, 2517

Schawinski, K., Thomas, D., Sarzi, M., et al. 2007, MNRAS, 382, 1415

Schawinski, K., Khochfar, S., Kaviraj, S., et al. 2006, Nature, 442, 888

Schechter, P. 1976, ApJ, 203, 297

Schlafly, E. F., & Finkbeiner, D. P. 2011, ApJ, 737, 103

Schmidt, M. 1963, Nature, 197, 1040

Schneider, E. E., Ostriker, E. C., Robertson, B. E., & Thompson, T. A. 2020, ApJ, 895, 43

Sharma, P., Roy, A., Nath, B. B., & Shchekinov, Y. 2014, MNRAS, 443, 3463

Shin, J., Woo, J.-H., & Mulchaey, J. S. 2016, ApJS, 227, 31

Sijacki, D., Pfrommer, C., Springel, V., & Enßlin, T. A. 2008, MNRAS, 387, 1403

Silk, J. 2013, ApJ, 772, 112

Silk, J., & Mamon, G. A. 2012, Research in Astronomy and Astrophysics, 12, 917

Silk, J., & Nusser, A. 2010, ApJ, 725, 556

Silk, J., & Rees, M. J. 1998, A&A, 331, L1

Simionescu, A., Werner, N., Finoguenov, A., Böhringer, H., & Brüggen, M. 2008, A&A, 482, 97

Sądowski, A., Lasota, J.-P., Abramowicz, M. A., & Narayan, R. 2016, MNRAS, 456, 3915

Sądowski, A., & Narayan, R. 2015, MNRAS, 453, 3213

Sądowski, A., Narayan, R., McKinney, J. C., & Tchekhovskoy, A. 2014, MNRAS, 439, 503

Sądowski, A., Narayan, R., Penna, R., & Zhu, Y. 2013, MNRAS, 436, 3856

Sobacchi, E., & Sormani, M. C. 2019, MNRAS, 486, 205

Solomon, P. M., Downes, D., Radford, S. J. E., & Barrett, J. W. 1997, ApJ, 478, 144

Solomon, P. M., Rivolo, A. R., Barrett, J., & Yahil, A. 1987, ApJ, 319, 730

Solomon, P. M., & Vanden Bout, P. A. 2005, ARA&A, 43, 677

Sparks, W. B., Pringle, J. E., Carswell, R. F., et al. 2012, ApJL, 750, L5

Tacconi, L. J., Genzel, R., & Sternberg, A. 2020, ARA&A, 58, 157

Tadhunter, C. 2016, A&AR, 24, 10

Tamburro, D., Rix, H. W., Leroy, A. K., et al. 2009, AJ, 137, 4424

Tamhane, P. D., McNamara, B. R., Russell, H. R., et al. 2022, arXiv e-prints, arXiv:2207.14326

Tamura, T., Bleeker, J. A. M., Kaastra, J. S., Ferrigno, C., & Molendi, S. 2001a, A&A, 379, 107

Tamura, T., Kaastra, J. S., Peterson, J. R., et al. 2001b, A&A, 365, L87

Tombesi, F., Meléndez, M., Veilleux, S., et al. 2015, Nature, 519, 436

Tremblay, G. R., Oonk, J. B. R., Combes, F., et al. 2016, Nature, 534, 218

Tremblay, G. R., Combes, F., Oonk, J. B. R., et al. 2018, ApJ, 865, 13

van Breugel, W., Filippenko, A. V., Heckman, T., & Miley, G. 1985a, ApJ, 293, 83

—. 1985b, ApJ, 293, 83

van Breugel, W., Heckman, T., & Miley, G. 1984a, ApJ, 276, 79

—. 1984b, ApJ, 276, 79

van Dokkum, P. G., Whitaker, K. E., Brammer, G., et al. 2010, ApJ, 709, 1018

Vantyghem, A. N., McNamara, B. R., Russell, H. R., et al. 2014, MNRAS, 442, 3192

—. 2016, ApJ, 832, 148

Vantyghem, A. N., McNamara, B. R., Edge, A. C., et al. 2017, ApJ, 848, 101

Vantyghem, A. N., McNamara, B. R., Russell, H. R., et al. 2018, ApJ, 863, 193

Veilleux, S., Cecil, G., & Bland-Hawthorn, J. 2005, ARA&A, 43, 769

Veilleux, S., Maiolino, R., Bolatto, A. D., & Aalto, S. 2020, A&AR, 28, 2

Veilleux, S., Meléndez, M., Sturm, E., et al. 2013, ApJ, 776, 27

Vernet, J., Dekker, H., D'Odorico, S., et al. 2011, A&A, 536, A105

Vogelsberger, M., McKinnon, R., O'Neil, S., et al. 2019, MNRAS, 487, 4870

Voit, G. M., & Donahue, M. 2015, ApJL, 799, L1

Voit, G. M., Meece, G., Li, Y., et al. 2017, ApJ, 845, 80

Voit, G. M., Bryan, G. L., Prasad, D., et al. 2020, ApJ, 899, 70

Wagner, A. Y., Bicknell, G. V., & Umemura, M. 2012, ApJ, 757, 136

Webster, B., Croston, J. H., Harwood, J. J., et al. 2021a, MNRAS, 508, 5972

Webster, B., Croston, J. H., Mingo, B., et al. 2021b, MNRAS, 500, 4921

Weilbacher, P. M., Palsa, R., Streicher, O., et al. 2020, A&A, 641, A28

White, S. D. M., & Frenk, C. S. 1991, ApJ, 379, 52

Willott, C. J., Rawlings, S., Blundell, K. M., & Lacy, M. 1999, MNRAS, 309, 1017

Yang, X., Mo, H. J., & van den Bosch, F. C. 2003, MNRAS, 339, 1057

Yu, S., Bullock, J. S., Wetzel, A., et al. 2020, MNRAS, 494, 1539

Yuan, F., & Narayan, R. 2014, ARA&A, 52, 529

Zabludoff, A. I., Huchra, J. P., & Geller, M. J. 1990, ApJS, 74, 1

Zhang, C., Zhuravleva, I., Gendron-Marsolais, M.-L., et al. 2022, arXiv e-prints, arXiv:2203.04259

Zhuravleva, I., Churazov, E., Schekochihin, A. A., et al. 2014, Nature, 515, 85

Zinn, P. C., Middelberg, E., Norris, R. P., & Dettmar, R. J. 2013, ApJ, 774, 66

Zovaro, H. R. M., Nesvadba, N. P. H., Sharp, R., et al. 2019, MNRAS, 489, 4944

Zubovas, K., & King, A. 2012, ApJL, 745, L34

Zubovas, K., & King, A. R. 2014, MNRAS, 439, 400

Zubovas, K., Nayakshin, S., King, A., & Wilkinson, M. 2013, MNRAS, 433, 3079

APPENDICES

Appendix A

Details of individual BCGs in the sample

A.1 Description of targets

The molecular gas distribution in BCGs is often clumpy and asymmetric. Filaments exist in most systems with narrow velocity widths and smooth gradients. Filaments are often found behind rising X-ray cavities or encasing the cavities. The fraction of molecular gas in filaments ranges from greater than 70 per cent to greater than 30 per cent. Most systems exhibit multiple velocity components in the molecular gas spectra. The spatial extent of the filaments determines the size of the flow. In the following subsections, we briefly describe molecular gas morphology and kinematics in each target in our sample.

A.1.1 2A0335+096

The molecular gas distribution in 2A0335+096 has a filamentary structure with the filament extending SE to NW of the BCG. There is a large reservoir of molecular gas south of the BCG at a velocity of -240 km s^{-1}. The north filament appears discontinuous and extends ~ 3 arcseconds (2 kpc) and has an average velocity of 200 km s^{-1}. The PV diagram along the BCG does not show a sign of a rotating disk (Vantyghem et al., 2016, see Fig. 11). We consider both the N filament and the southern molecular gas as a flow in this BCG.

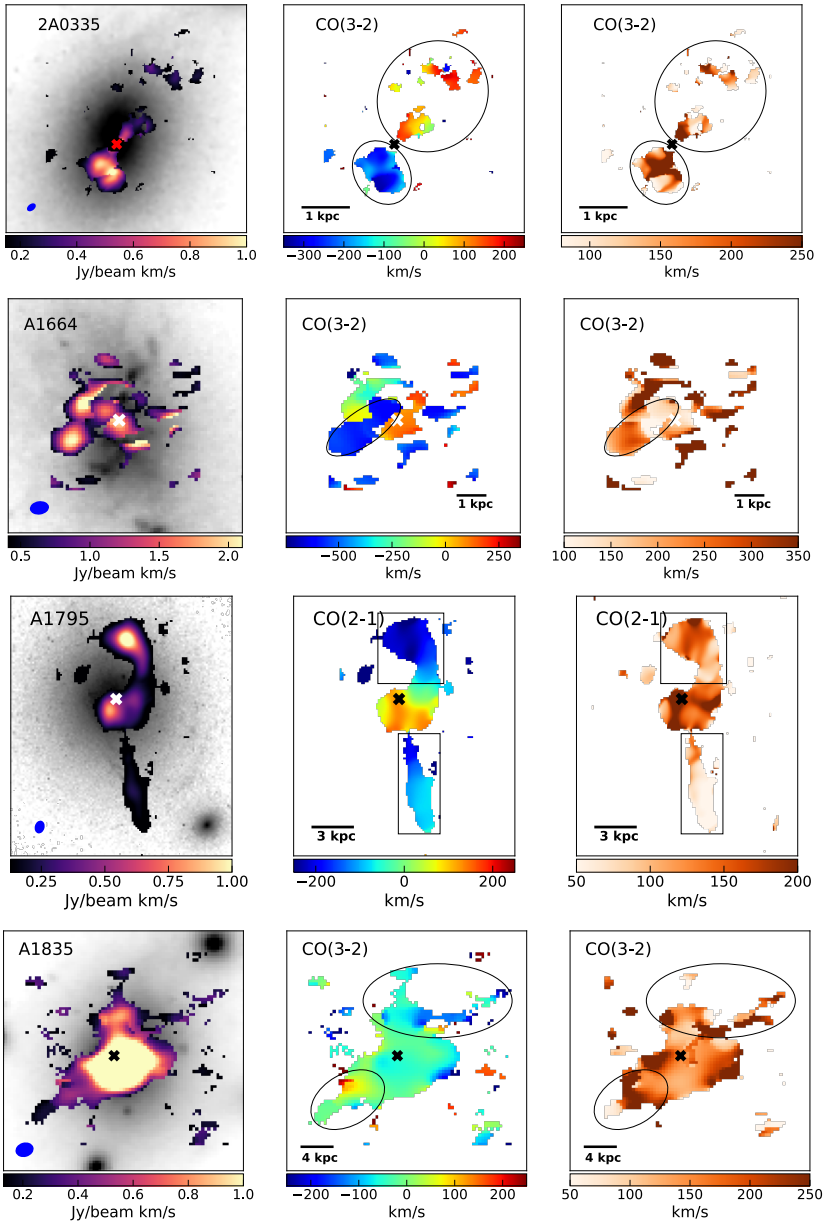
2A0335
CO(3-2)
CO(3-2)
1 kpc
1 kpc
0.2 0.4 0.6 0.8 1.0
Jy/beam km/s
−300 −200 −100 0 100 200
km/s
100 150 200 250
km/s
A1664
CO(3-2)
CO(3-2)
1 kpc
1 kpc
0.5 1.0 1.5 2.0
Jy/beam km/s
−500 −250 0 250
km/s
100 150 200 250 300 350
km/s
A1795
CO(2-1)
CO(2-1)
3 kpc
3 kpc
0.25 0.50 0.75 1.00
Jy/beam km/s
−200 0 200
km/s
50 100 150 200
km/s
A1835
CO(3-2)
CO(3-2)
4 kpc
4 kpc
0.2 0.4 0.6 0.8 1.0
Jy/beam km/s
−200 −100 0 100 200
km/s
50 100 150 200 250
km/s

Figure A.1 *(previous page)*: ALMA CO integrated intensity map overlaid on HST images (left column), velocity centroid maps (middle column), and FWHM maps (right column) for all BCGs in our sample are shown. For RXCJ1539, DSS red band image is shown. The beam size is indicated as a grey ellipse. The crosses indicate the location of the AGN in each BCG. The emission region enclosed by black ellipses or polygons in the right panels of each row indicates the region we consider as a flow in each BCG.

A.1.2 Abell 1664

In Abell 1664, the molecular gas is distributed in a high velocity filament E of the BCG center, a blob to the north of the BCG and another blob coincident with the AGN. The E filament extends up to ∼6.37 kpc from the BCG center, whereas the north blob is ∼5.8 kpc away from the BCG in projection. The high velocity filament has a velocity of 590 km s^{-1}, whereas the blob co-incident with the AGN could be part of a molecular gas disk. We consider the high velocity filament as the flow as shown by elliptical region in Fig A.1. Russell et al. (2014, Fig. 4 and 5) show PV diagram along the flow filament and across the BCG. There is a possibility of molecular gas disk across the BCG, the flow filament has a different velocity structure than the central gas reservoir and is not part of the potential molecular gas disk.

A.1.3 Abell 1795

The molecular gas in A1795 is distributed in two filaments extending to the north and southwest of the BCG centre, and in a central region around the BCG's nucleus. The north filament is curled up around a radio jet (see Russell et al. (2017b)) with a projected length of 4.2 arcsec (5.1 kpc) and the SW filament is more extended at a projected length of 6 arcsec (7.3 kpc). Both filaments have a distinct velocity structure compared to the central clump, which has a velocity centroid of ∼1 km s^{-1} with respect to systemic velocity. The SW filament has a shallower velocity gradient with velocity centroid lying between −80 to −180 km s^{-1} from the tail-end to the base, respectively. In the N filament, the velocity gradient increases from −270 km s^{-1} near the edge to 0 km s^{-1} at the base. The two filaments are considered as flows in our analysis. The PV diagrams presented in Russell et al. (2017b) show no evidence of a rotating disk. We consider the N and the S filament as flows in our analysis.

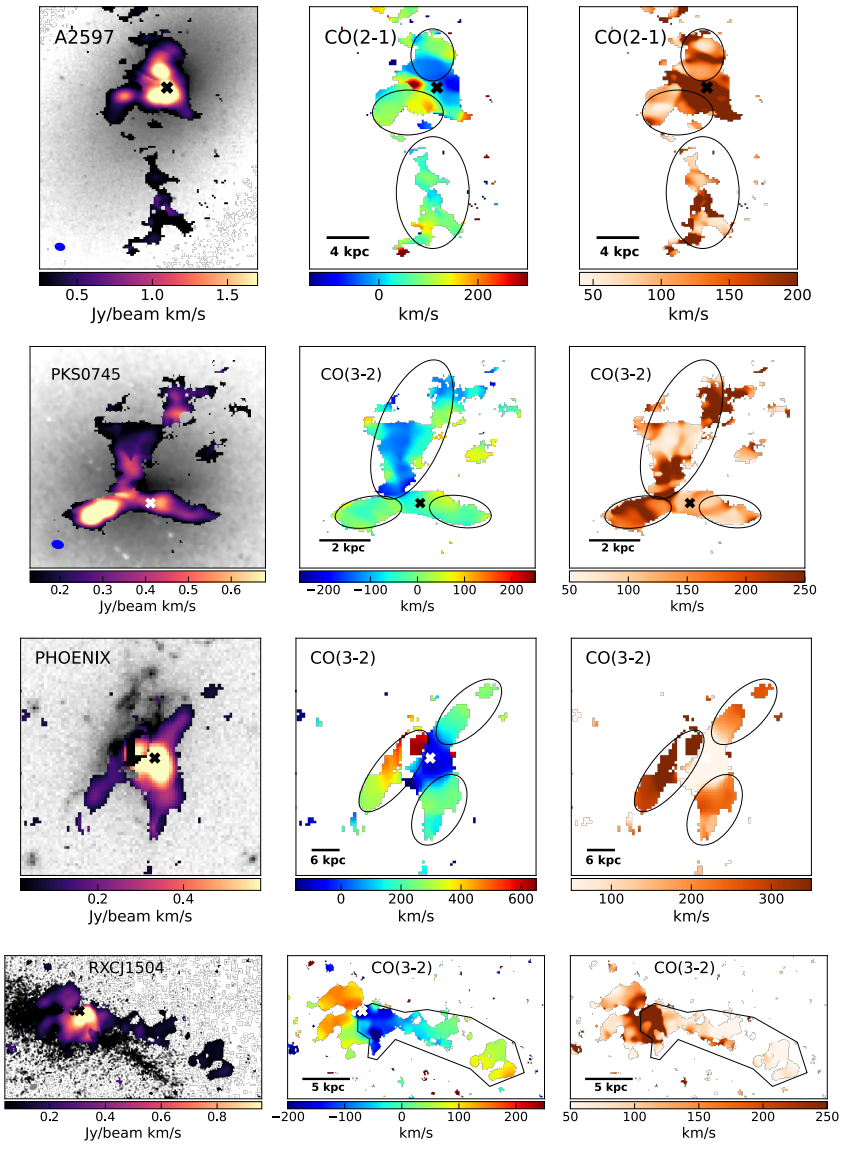

Figure A1 (Continued)

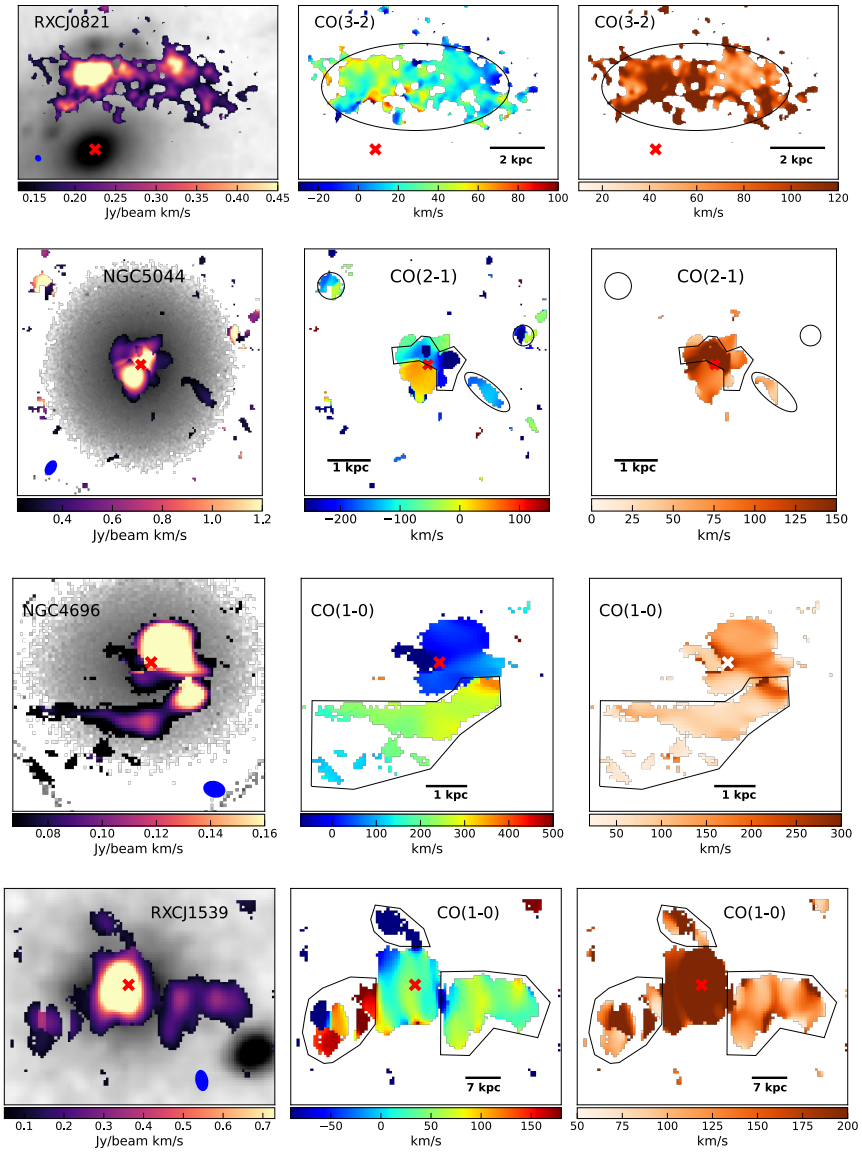

Figure A1 (Continued)

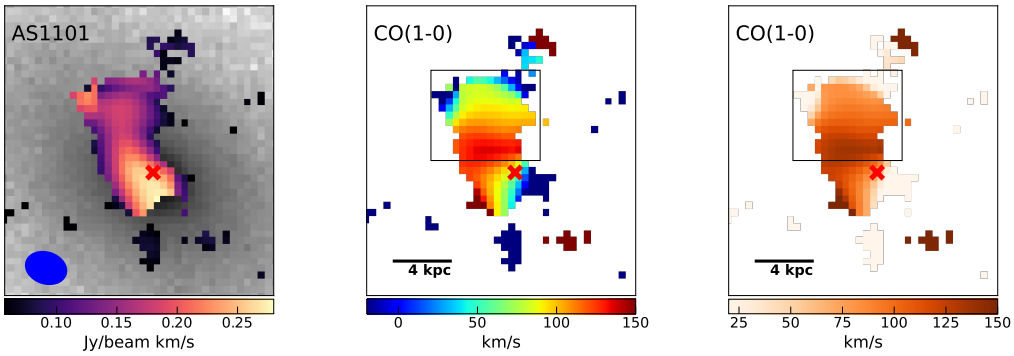

Figure A1 (Continued)

A.1.4 Abell 1835

The molecular gas in Abell 1835 is mostly located within 3 kpc of the BCG centre and peaks within a few tens of km s^{-1} of the galaxy's systemic velocity. However, there are filaments extending ∼12 kpc towards N and SE of the nucleus behind X-ray cavities. The N filament has a narrow component with a velocity centre close to the systemic velocity and a broad component with a velocity centre at −230 km s^{-1}. The SE filament has an average velocity shift of 40 km s^{-1} and another faint ∼200 km s^{-1} component. The PV along the BCG does not show a clear sign of a molecular gas disk (see Fig. A2), although most of the molecular gas in the centre is unresolved. The filaments appear to be part of a bipolar outflow. These regions we consider as flows are shown in Fig. A.1.

A.1.5 Abell 2597

In Abell 2597, most of the molecular gas is distributed in bright filaments draped around radio bubbles close to the nucleus and in a fainter, elongated filament extending ∼15 kpc south of the BCG. The brighter filaments are ∼6.3 kpc long and contain ∼50 per cent of molecular gas. Abell 2597 has a complex velocity structure. Filaments have a shallow constant velocity gradient between velocities 60 to 40 km s^{-1}. In the innermost 2 kpc, the gradient changes from −120 km s^{-1} to 120 km s^{-1}. The system also has absorption features at 240, 275, and 335 km s^{-1} (Tremblay et al., 2016), which indicates that the gas is moving at fast speeds close to the nucleus. The regions considered as flows are shown in Fig. A.1. See Tremblay et al. (2018) for PV diagrams of the filaments and the central gas structure.

A.1.6 PKS0745+091

The molecular gas in PKS0745+091 is distributed in three filaments extending north, southwest (SW), and southeast (SE) directions, respectively. The northern filament is most extended at 5.73 kpc followed by SW and SE filaments at projected lengths of 3.6 and 2.7 kpc, respectively. The north and SW filaments appear to be trailing behind an X-ray cavity. The PV diagrams reveal a a velocity gradient from -150 to 50 km s^{-1} (see Fig. 8, Russell et al., 2016). We consider these filaments as flows in this BCG and are shown in Fig. A.1.

A.1.7 Phoenix

Phoenix is one of the most luminous galaxy clusters. The BCG in the Phoenix cluster is massive and has an ongoing star formation at a rate of 610 M$_\odot$ year^{-1}. It contains a large amount of molecular gas. The molecular gas in Phoenix is distributed around the centre and in three filaments extending 20-24 kpc to N, SE, and S of the BCG centre. Filaments show a smooth velocity gradient with narrow FWHM (<250 km s^{-1}), indicating ordered flow motion (also see Fig. 5, Russell et al., 2017a). The velocity centroids vary in the range between 280 km s^{-1} to 0 km s^{-1} in NW filament and $\sim$250 km s^{-1} to $\sim$570 km s^{-1} in the SE filament and 250 to 50 km s^{-1} in the S filament. These filaments shown in Fig. A.1 are considered flows in this BCG.

A.1.8 RXCJ1504

RXCJ 1504 has a central clump and a disturbed, clumpy filament extending radially outward to the W the BCG centre. The projected size of the filament is 18 kpc from the BCG centre, and it contains roughly 30 per cent of the total molecular gas in the system. It has a smooth velocity gradient with velocities between 90 km s^{-1} near the tail to -210 km s^{-1} at the base with an FWHM less than 100 km s^{-1} throughout most of the filament. We consider this filament as a flow in this BCG which is shown as a region enclosed by a polygon in Fig. A.1.

A.1.9 RXCJ0821+0752

The molecular gas in RXCJ0821+0752 is distributed in two major clumps. The first clump, which is $\sim$ 3 kpc north of the BCG centre, contains the majority ($\sim$60%) of molecular gas.

It has a velocity centroid of 24 km s^{-1} compared to the systemic velocity. The secondary clump is located 3 kpc west of the first clump and has a velocity centroid of ∼20 km s^{-1}. The entire molecular gas distribution is offset from the BCG. The position velocity diagram doesn't show any sign of rotation (see Fig. A2). The region considered as a flow is shown in Fig. A.1.

A.1.10 NGC 5044

Most of the molecular gas in NGC 5044 is distributed around the central galaxy, and some of it is detected as individual clouds of molecular gas NE, NW and E of the BCG. There is a very high-velocity cloud blueshifted to velocities of ~ -500 km s^{-1} close to the nucleus. The PV diagram across the BCG doesn't show any sign of a rotating disk. We consider the blueshifted components and the clouds of molecular gas as parts of flow in this galaxy. They are shown in Fig. A.1.

A.1.11 NGC 4696

The molecular gas in NGC 4696 is distributed in a large clump roughly cospatial with the BCG nucleus and in a ∼4 kpc long curved filament S of the BCG. The central gas reservoir has velocities within 50 km s^{-1} of the BCGs systemic velocity, whereas the filament has a velocity gradient from 120 km s^{-1} in the outer parts to ∼350 km s^{-1} in the inner part. The PV diagrams do not show any sign of a rotating disk. This extended filament is considered a flow in NGC 4696.

A.1.12 RXCJ1539

RXCJ1539 has two large filaments to the E and W of the BCG and a central clump of molecular gas co-spatial with the BCG. The E and W filaments extend out to 24 and 27 kpc, respectively. Another small spur of molecular gas is detected to the N of the BCG extending out to 18 kpc. The W filament has a roughly constant velocity of ∼50 km s^{-1}. The E filament is mostly redshifted to velocities of up to 200 km s^{-1}, but also contains a blueshifted component at a velocity of -210 km s^{-1}. The N filament, however, is entirely blueshifted to velocities of up to -285 km s^{-1}. The inner 7 kpc radius region around the nucleus has velocities lying between ∼0 to 50 km s^{-1}. It is no unambiguous evidence of smooth gradient or ordered motion indicating a rotating disk in the PV diagrams shown

in Fig. A2, as the central reservoir is unresolved. The three regions we consider as a flow in this BCG are shown in Fig. A.1.

A.1.13 AS1101

The molecular gas in AS1101 appears as a single extended filament to the N of the BCG. The filament has a smooth velocity gradient from 140 km s−1 close to the BCG to 40 km s^{-1} in the outer parts. It is extended out up to 8.23 kpc N of the BCG. Some blueshifted emission is detected to the W of the BCG at velocities of −130 km s^{-1}. The PV diagrams show a smooth velocity gradient across the filament. The filament is indistinguishable from the circumnuclear gas in this data. The region we consider as a flow is shown in Fig. A.1.

A.2 Flow properties with adjusted velocities for Fluetsch galaxies

In Fig. 2.1, we showed that applying the Fluetsch method to BCGs overestimates flow velocities by a factor of two. Assuming that a similar systematic difference in velocities applies to galaxies in the Fluetsch sample, we divide their outflow velocities by two to estimate new velocities. It results in a reduction of molecular outflow rates by half, kinetic energies of outflows by a factor of 8 and momenta by a factor of 4. Figure A5 shows all the relevant figures where outflow properties for galaxies in the Fluetsch sample are calculated using new velocities. It does not affect correlation coefficients for Fluetsch outflows. The average flow velocities of BCGs lie only 30% below average flow velocity in AGN hosting galaxies and $\sim 20\%$ faster than flow velocities in starburst galaxies. The flow momenta for AGN, composite and starburst galaxies are 3.3×10^{49}, 5.2×10^{48} and 8.6×10^{48} g cm s^{-1}, respectively. They are 10–15 times smaller than flow momenta in BCGs. The loading factors do not change significantly. More galaxies lie within theoretical maximum limits for energy and momentum conserving flows. At the same time, the ratio of kinetic power of the flow to the power of the driving mechanism falls below 0.05% for some galaxies, indicating a weak coupling. The lifting factor remains unaffected, as it does not depend on the flow velocity. Thus, qualitatively, these results are consistent with the results presented in the sections above.

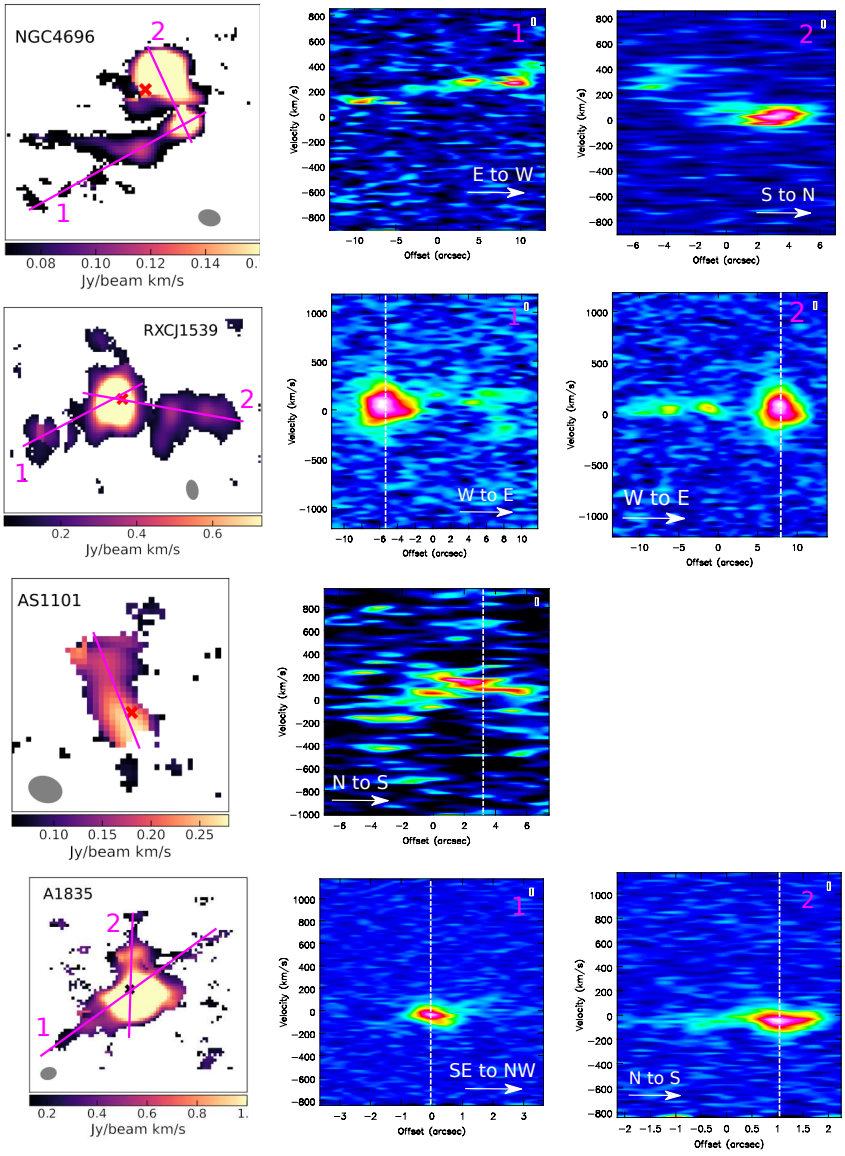
NGC4696
2
1
0.08 0.10 0.12 0.14 0.
Jy/beam km/s
1
E to W
Velocity (km/s)
Offset (arcsec)
2
S to N
RXCJ1539
2
1
0.2 0.4 0.6
Jy/beam km/s
1
W to E
2
W to E
AS1101
0.10 0.15 0.20 0.25
Jy/beam km/s
N to S
A1835
2
1
0.2 0.4 0.6 0.8 1.
Jy/beam km/s
1
SE to NW
2
N to S

Figure A2 *(previous page)*: The position-velocity diagrams of BCGs in our sample. The left panel shows an integrated intensity image where the magenta lines indicate the axis used to make PV diagrams. The right panels show the PV diagrams corresponding to the labels shown in the left panel when PV diagrams along multiple axes are shown. The dashed vertical lines show the position of the BCG centre. In all images, the east is to the left and the north is up. The position velocity diagrams do not show any sign of symmetric ordered motion about the nucleus in filaments in any of the BCGs.

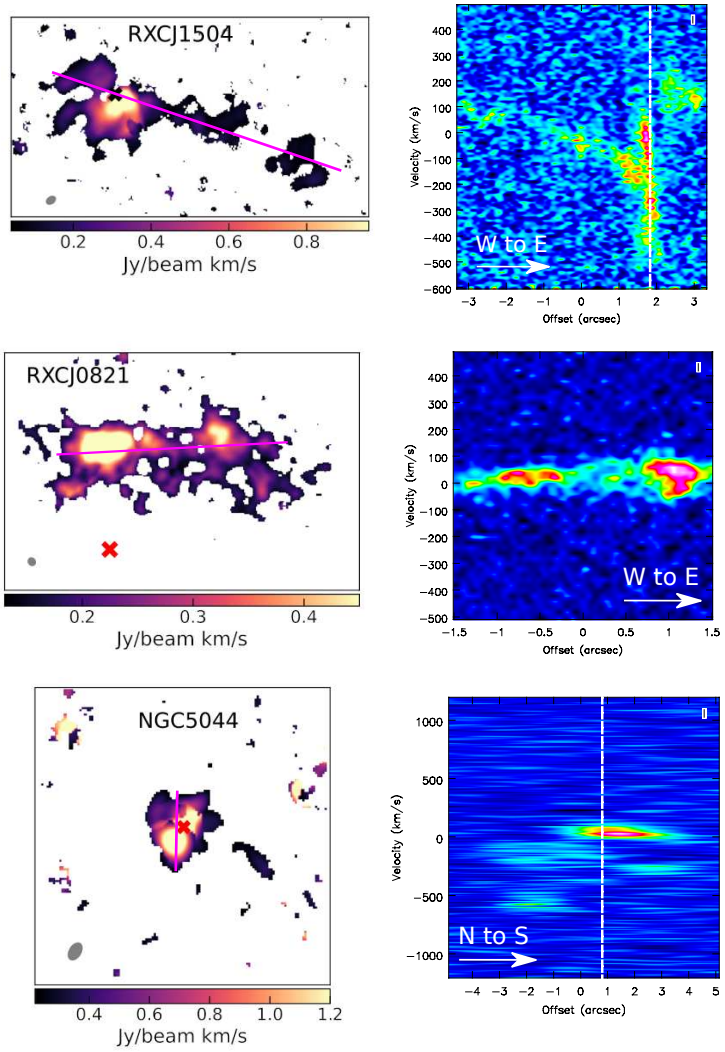

Figure A2 (Continued)

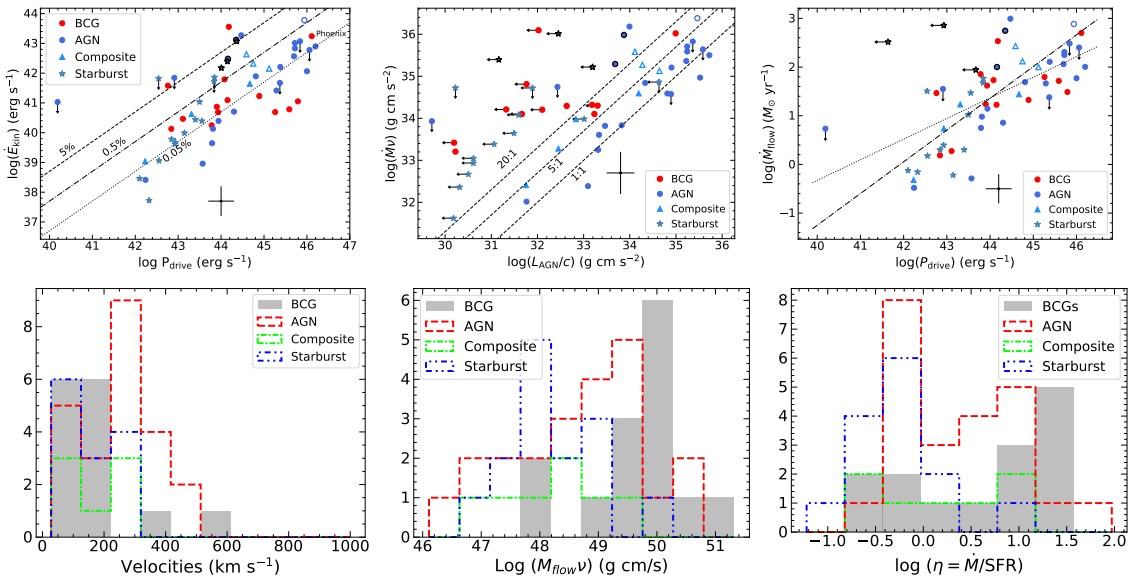

Figure A5: We show figures 2.9, 2.6, 2.8, 2.2, 2.7, 2.11 from top left to bottom right panels, respectively, with the molecular flow rate, momentum, kinetic energy of the flow calculated with adjusted flow velocities for fluetsch galaxies as described in Appendix A.2.

Appendix B

Additional Figures in chapter 3

In this appendix, we present supporting figures for chapter 3. The first figure (Fig. A1) shows the Hα emission line complex in different regions of the slit shown in the left panel of Fig. 3.1, with the results of multicomponent gaussian fit to the line profiles. The details of how the profiles were fit are described in section 3.4.3.

The second figure shows the different regions used to calculate the VSF in Abell 1795 for the molecular gas velocity field (left panel) and the Hα gas velocity field (right panel). The resulting VSF are shown in Fig. 3.13.

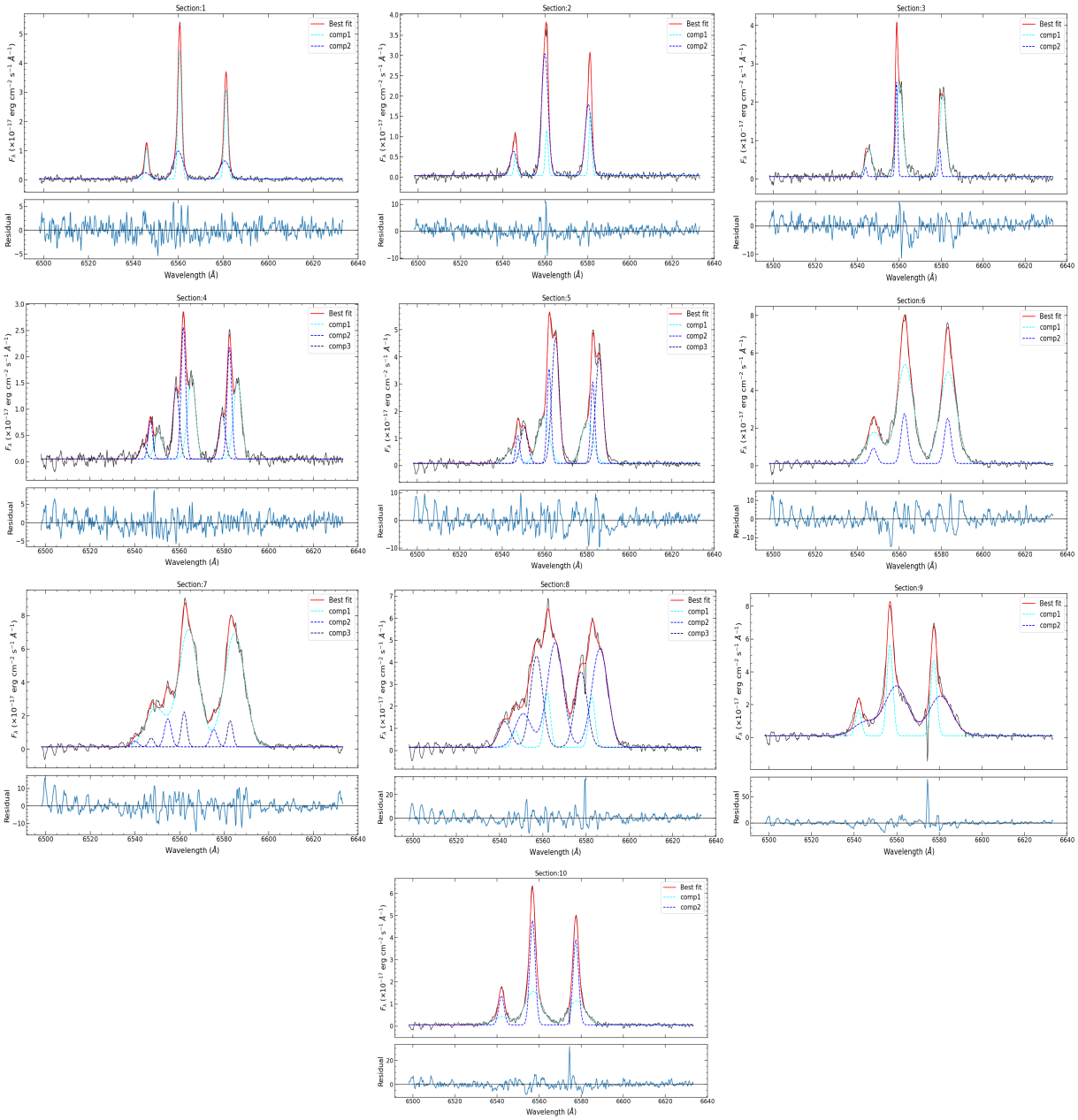

Figure A1: Hα-[NII] complex emission line fits to the regions along the slits as described in section 3.4.3. The red curve is the summed emission line profile and the blue curves show individual Gaussian components required for the fit. The residuals are shown in the bottom panel of each fit.

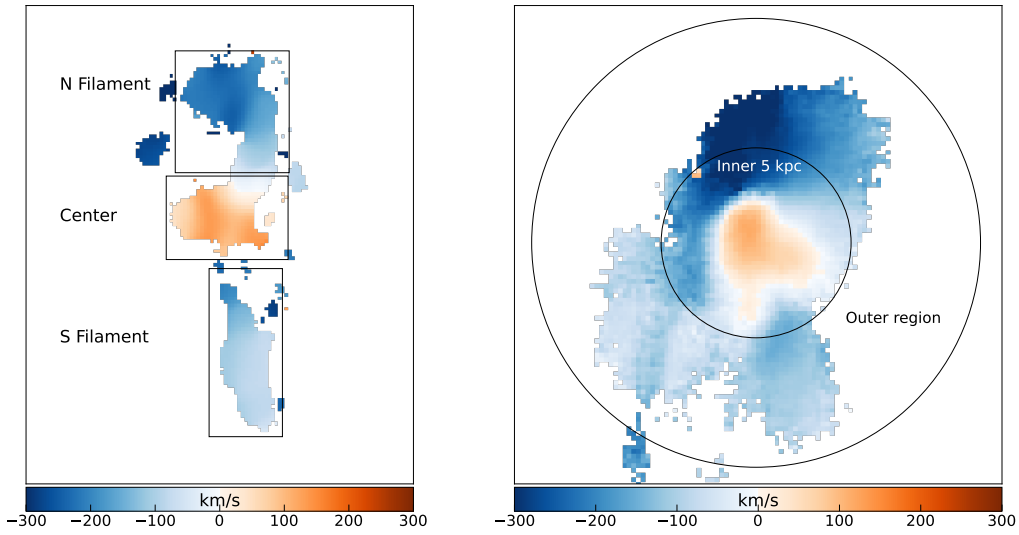

Figure A2: The first moment maps of the molecular gas (left panel) and Hα gas (right panel) used to calculate the velocity structure function as described in section 3.8, where the error in velocity at each pixel is less than 10 km s^{-1}.

Appendix C

Other Contributions

In addition to the research presented in the thesis, I have also collaborated on several projects. Some of those projects lead to publications. The sections below provide a brief overview of these projects and my contributions in them.

C.1 Additional ALMA data analysis of Early Type Galaxies

It has been argued that the cold gas observed in BCGs primarily forms from condensation of hot gas in clusters (Gaspari et al., 2017; Voit et al., 2017; Pulido et al., 2018). However, the origin of molecular gas content in early type galaxies (ETGs) is a poorly understood issue. ETGs are generally believed to be devoid of molecular gas, however, recent surveys showed that 30–40% of ETGs have a considerable amount of molecular gas. Several indicators suggest an external origin of the molecular gas in ETGs. In this paper, we took a similar approach as the one used to study BCGs and explored the probable origin of molecular gas in ETGs from their hot X-ray atmospheres.

I analyzed archival ALMA data of five Early Type Galaxies (ETGs) from a sample of 40 relatively nearby ETGs. We detected $\sim 6 \times 10^7$ $M_\odot$ of molecular gas in NGC1332 and NGC4696, $\sim 5 \times 10^8$ $M_\odot$ of molecular gas in NGC6881 and molecular gas upper limits of $8{\times}10^5$ $M_\odot$ and 10^7 $M_\odot$ in IC1459 and NGC1407, respectively. I wrote section 5.1 in Babyk et al. (2019) that describes the ALMA data analysis and its results including table 3 and figure 5.

The molecular gas mass measurements in these galaxies were combined with molecular gas mass measurements available for other ETGs in the sample from single dish telescopes and compared them to the properties of their hot atmospheres traced using *Chandra* X-ray observations. We found a power-law relationship between the mass and density of the hot gas and the cold molecular gas mass across a wide range of galaxies from central galaxies in clusters to normal giant ellipticals and early spirals. The ETGs with cooling times of $\sim$ Gyr at 10 kpc have detectable amount of molecular gas, a trend that is also observed in BCGs. A correlation between the ratio of cooling time to free-fall time and molecular gas mass was not observed. These results suggested that similar to the most massive cool-core BCGs, most of the molecular gas in ETGs condensed from their hot atmospheres.

C.2 Spoiler clusters

Cool-core BCGs are characterized by short central gas cooling times of $\lesssim 10^9$ yr and low gas entropy of $\lesssim 30$ keV cm^2. Although radio-mechanical feedback heats the atmospheres of these clusters maintaining the hydrostatic and thermal equilibrium on large scale, it also promotes some residual cooling, where the ratio of local cooling time ($t_{\rm cool}$) to free-fall time ($t_{\rm ff}$) of the gas falls below unity (Nulsen, 1986; Voit & Donahue, 2015; Prasad et al., 2018). These properties are commonly associated with the presence of cold molecular gas, warm Hα gas and star formation. In this paper, we studies 5 clusters that have low central gas cooling times and entropies, similar to cool-core clusters, but do not have a detectable level of cold and warm gas, and star formation.

We analyzed *Chandra* X-ray observations of these clusters. I helped Connor, the lead author of the paper, with the analysis of X-ray data and the discussion. We found that X-ray atmospheres of these clusters are fairly smooth and do not show any evidence of a disturbance, despite four out of five clusters showing radio emission associated with radio jets (Martz et al., 2020). Only RBS 0533 cluster may host a radio/X-ray bubble. The lack of cold molecular and Hα gas comparable to other cool-core BCGs with similar atmospheric profiles indicates that these systems have failed to lift the low-entropy gas from central regions to altitudes where its local $t_{\rm cool}/t_{\rm ff} \lesssim 1$, which promotes gas cooling. The metallicity maps of these BCGs also do not show any evidence of high metallicity gas along the radio-jet axis compared to other parts of the cluster atmosphere.

These results support the stimulated feedback model of gas cooling where low-entropy gas lifted by cavities out of central regions to high altitudes cools to form cold gas filaments observed in BCGs (McNamara et al., 2016). All cool-core clusters that have detectable level of cold gas and short atmospheric cooling times at the center have surface brightness

depressions in their X-ray emitting atmospheres supporting this hypothesis. However, as we discussed in chapter 4, single generation of X-ray cavities alone cannot lift enough low entropy gas to explain the observed levels of cold gas in cluster environments. Perhaps the gas is accumulated over several generations of cavities produced by different cycles of AGN activity.